Study of viscoelasticity and adhesion of human alveolar epithelial cells by atomic force microscopy

The importance of probe geometry

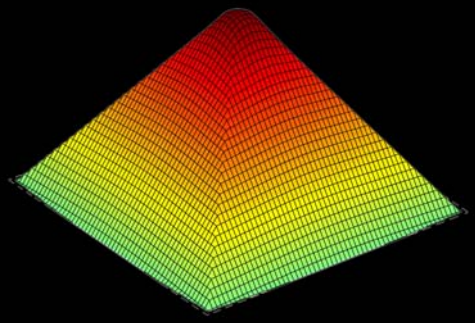

Félix Rico Camps

Study of viscoelasticity and adhesion of human alveolar epithelial cells by atomic force microscopy

The importance of probe geometry

Study of viscoelasticity and adhesion of human alveolar epithelial cells by atomic force microscopy

The importance of probe geometry

A dissertation by

Félix Rico Camps

in partial fulfilment of the requirements for

the degree of Doctor of Philosophy

Barcelona, November 2005

PhD supervisor:

Prof. Daniel Navajas Navarro

Unitat de Biofísica i Bioenginyeria
Dept. de Ciències Fisiològiques I
Facultat de Medicina
Universitat de Barcelona

Preface

The first thought that comes to a physicist involved in biology is whether physics can explain biology. Of course, I cannot answer this question (probably nobody can), because maybe it is not the correct one . A better question might be: *what biological processes can be explained by the laws of physics?* Since Nature appears to be governed by physical laws, it seems obvious that the behavior, structure and function of cells, as part of Nature, are limited by and subjected to the laws of physics. Cellular biophysics does not seek to explain how cells are, but what can we say about cells from the physical point of view. During the last century, cellular biology has been mostly assessed from the biochemical point of view: studying how biochemical stimuli modify the biochemical composition of living cells. However, most of the cells that form our body constantly exert or are subjected to mechanical forces. Muscle cells exert forces during contraction, vascular endothelial cells are subjected to shear forces due to blood streaming, and pulmonary cells resist cyclic deformations due to spontaneous breathing, to mention only a few examples. Therefore, mechanical forces are present in almost all cell types and it seems reasonable that they play an important role in determining cell structure, composition, and function. The recent development of techniques designed to manipulate molecules and cells with nanometric resolution and to measure forces in the picoNewton range opened a new field of study. The continuous increase in works relating mechanical properties of cells with cellular function has shown that mechanics are as important as biochemistry at the cellular level. Thus, the main aim of this thesis is the application of physical tools to better understand the biological world.

The studies presented in this thesis are part of the work I carried out during the last four years in the Biophysics and Bioengineering Unit at the University of Barcelona School of Medicine. The thesis can be divided into four main sections: Introduction, Aims, Experimental studies, and Conclusions. The introduction (Chapter 1) attempts to make a brief review of cellular mechanics. It describes the main cellular components involved, the way in which atomic force microscopy can be used, and some relevant results found in literature. Chapter 1 also draws attention to the limitations of atomic force microscopy when

applied to cell mechanics, and to some important questions that remain open. The aims of the thesis (Chapter 2) correspond to each of the four experimental works described in the thesis. The third section (Chapters 3-6) consists of four experimental works that makes up the core of the thesis. The main theme of the thesis is atomic force microscopy and how it can be applied to the understanding of cellular mechanics. The subtitle of the thesis *The importance of probe geometry* was chosen because three of the four experimental studies are focussed on the manner in which the geometry of the probe may affect the measurements and influence the results obtained. Chapter 3 describes the development and validation of the atomic force microscopy (AFM) system. Chapter 4 presents a study of cell mechanics probed with blunted pyramidal AFM tips. The work in Chapter 5 validates cylindrical AFM tips. In Chapter 6, a study of cell adhesion under inflammatory mediators is presented. Each chapter is written as a paper in order to facilitate reading. The last section presents the main conclusions of the thesis (listed in Chapter 7). Two appendixes are provided at the end of the thesis.

Acknowledgements

During the last four years as a PhD student I have met different people from here, there and everywhere from whom I have learned and unlearned more than I have ever thought. I would like, here, to thank them all.

Vull començar per donar les gràcies a qui més directament ha influït (casi sempre per bé) en el meu treball diari, que són els components passats i presents de la Unitat de Biofísica. Gràcies pel bon i mal humor que ha fet de la Unitat un lloc extraordinari, tan pel bon ambient laboral, com pel millor companyerisme.

Especialment al Daniel, director d'aquesta tesi, per haver confiat (i desconfiat) en mi, per haver-me contagiat del seu rigor científic i extracientífic, i per donar-me la llibertat necessària per dirigir el meu rumb sense deixar de guiar-me per l'oceà de la recerca.

A la resta de *seniors* (i no tant) de la Unitat. En concret, a la Mar, per endinsar-se amb i sense mi, durant llargues hores, pel tortuós camí del desenvolupament matemàtic i per ensenyar-me els seus trucs i piruetes informàtiques; al Ramon, per ser tan bon advocat del Diable i ensenyar-me que provar i equivocar-se és més productiu que especular; al Domènec, per saber més que la pròpia UB la seva normativa, pel seu constant bon humor i per apropar-me de manera excepcional al llunyà món del processat d'imatges; i a Sir Charles el seu bon humor i la seva pau interior.

Agradecer a Miguel Ángel la sabiduría no sólo electrónica que ha ido dedicando día a día, sin la cual no habría sido posible el buen (o mal) funcionamiento de los aparatos desarrollados durante la realización de esta tesis, y de tantas otras.

A Núria Román por hacer que la burocracia fuera una obligación mucho más agradable gracias a su sonrisa y su buen humor.

Donar les gràcies a tots els col·legues que han patit i pateixen al laboratori. En especial al Jordi Alcaraz i a la Lara, l'un per haver-me ensenyat a estimar l'AFM i tots els seus secrets; l'altra per haver-me ensenyat a odiar-ho (tant o més necessari), haver compartit hores i insults davant de l'Uxi-uxi i no escatimar exemples didàctics per intentar fer-me comprendre el món biològic. A la Mireia per fer-me riure com ningú amb la seva visió pràctica i realista de la vida. Al Xavi, per fer-me còmplice de la seva supèrbia i per les

llargues nits de Genepí i Mojitos in the lostern most. Al Jordi Rigau, per demostrar que es pot ser efectiu i productiu sense estressar-se més de lo estrictament necessari. A la Ferranda, per l'alegria que (casi) sempre té i per agafar-me confiança (em sap greu). Al Pere, per odiar el Món casi tant com jo. A la Núria, per fer-me veure que es pot ser trekky sense ser del tot freak. Al Raimon, per portar dignament el tenir dos directors de tesi. A Aitor, por enseñarme que el pluriempleo conduce a la felicidad cuando lo sabes llevar. A la Maria Elena, per recordar-me cada dia que la gent normal té horaris dignes. A Isaac, por su gracia y espíritu didáctico al instruirme en el desconocido mundo de las ratas y el cultivo primario. Al David, per mostrar-me que es pot fer el doctorat sense haver de dormir al laboratori. Ad Irene, per avere cieca fiducia nella mia conoscenza scientifica. A la Gemma, per ensenyar-nos que el treball de l'Aitor consistia en més que enviar e-mails compulsivament. Agrair als domènecs (Deborah, Santi, Albert, Pascu, Pablo i Cristina) el deixar-me estar a prop de la seva cambra fosca i així poder contagiar-me una mica de la seva quietud i concentració. També al Marc (vesícules) i al Carles Solsona, per fer-me estudiar estructures nano de debò.

To all the people I met in the Moy lab during my stay in Miami (Vincent, Ewa, Midhat, Martin, Juliane, KJ). Thank you for giving me the opportunity of working with you, for sharing with me part of your knowledge and your time (during the day or during the night), and for making my stay much more fun and comfortable.

També donar les gràcies a la Universitat de Barcelona per la beca de Recerca i Docència que m'ha permès dedicar tot el meu temps a la tasca científica i docent. Tot i així, m'agradaria esmentar la precarietat laboral en que es troben els investigadors, no només predoctorals, deguda a la poca importància que sembla tenir la ciència en aquest país. Gràcies Precarios/D-recerca.

Para acabar, agradecer a todos los que me han ayudado más indirectamente. A mis padres, por hacerme y dejarme de hacer. A todos los amigos, amics, amici que, ignorando casi totalmente a lo que me dedicaba, me han dado su soporte, o más bien, me han soportado durante todo este tiempo, y más. Et a toi, pour me supporter tout ce que jamais j'aurais supporté.

Gràcies, gracias, grazie, thanks, merci.

Study of viscoelasticity and adhesion of human alveolar epithelial cells by atomic force microscopy

The importance of probe geometry

Contents

Chapter 1

Introduction

1.1 Structural components involved in cell mechanics

Cells are complex organisms formed by an enormous amount of different molecules and organelles. The structure, organization, and nature of these components determine the different cell types, their function, their communication with the surrounding environment, their live cycle, and, as described in this section, their mechanical behavior.

1.1.1 Cytoskeleton

The word cytoskeleton (CSK) has the etymological meaning of *skeleton of the cell*. Like vertebrates skeleton, the CSK indeed plays a central role in the maintenance and organization of the structural morphology of the cell. But cell CSK is more than an inert, static framework that supports the cell body. It also stands for the musculature and circulatory system of the cell, being responsible of cell crawling, cell contraction, intracellular trafficking, or cell division. The CSK forms a network of three main kinds of protein fibers bound by a series of intermolecular linkers and molecular motors, and connected to the extracellular environment and neighboring cells by membrane receptors. The cytoskeleton is thought to be the main responsible of cellular mechanics.

Actin filaments and related proteins

Actin filaments (AF) or *microfilaments* have shown to be the mayor determinants of cytoskeletal mechanics (Alberts et al., 1994; Bray, 2001). Actin filaments are long and flexible helical polymers (F-actin) formed by polymerization of the monomeric globular form of the protein (G-actin). Microfilaments, with a diameter of ~8 nm, have a Young's modulus (E) of ~2 GPa. It is important to note that individual actin filaments are ~10^6 times

stiffer than actin gels and typical animal cells, E~100-1000 Pa. Their relatively short persistence length, ~18 μm, reflects their suitability to support tension stresses (Fudge et al., 2003; Bray, 2001).

Actin is the most abundant protein in the majority of eukaryotic cells (5-10%), accounting for ~20% in some cell types, such as muscle cells. In a typical animal cell, actin filaments are localized at the peripheral region of the cell (0.2-0.5 μm beneath the plasma membrane) forming a three-dimensional network cross-linked mainly by α-actinin and filamin called the actin cortex. Actin is also found throughout the cytosol in both its soluble and polymerized form. Most of the movements of the cells are controlled by actin and its associated molecular motors. The polymerization of actin is indeed a form of movement and is regulated by the hydrolysis of energy. The growth rate at the two ends of AF are different, existing a pointed end (more static, lower growth rate), and a barbed end (more dynamic, faster growth rate) which is supposed to be responsible of filopodia formation (Mogilner and Oster, 2003). In determined cells, actin filaments can form dense, rigid bundles cross-linked with the molecular motor myosin. Under this configuration, they are usually referred to as stress fibers and they can develop forces, leading to cellular contraction or cytoskeletal reorganization, being also able to support compression (Stamenovic and Ingber, 2002). Using optical tweezers the force developed by the stroke on an AF of a single myosin II motor was estimated to be 3-5 pN, with a step size of 5.3 nm, and an energetic efficiency of 12-40% (Bustamante et al., 2004; Finer et al., 1994). Morphological changes in the actin CSK owed to pharmacological or mechanical stimulus commonly parallel variations in the global or local mechanical behavior of cells (Nagayama et al., 2004; Rotsch and Radmacher, 2000; Bhadriraju and Hansen, 2002). Alteration of the polymerization kinetics of actin by Latrunculin A or Cytochalasin D leads to CSK disruption and to a significant decrease in cellular stiffness, reducing also the ability of cells to move and contract. On the other hand, activation of the contractile apparatus, *i.e.* enhancement of actomyosin cross-bridge formation and actin polymerization, has shown to induce an increment in cellular stiffness in a number of cell types (Butler et al., 2002a; Fabry et al., 2001; Charras and Horton, 2002a; Smith et al., 2005; de Morales et al., 2004).

Microtubules and related proteins

Microtubules (MT) are also important determinants of cell mechanics. These have a different structure than actin filaments. MT are formed by polymerization of tubulin $\alpha\beta$ dimers arranged in a hollow cylindrical geometry of ~25 nm outer diameter and ~15 nm inner diameter. Using atomic force microscopy and taking into account their tubelike

structure, the Young's modulus of microtubules has been recently estimated to be ~0.8 GPa (de Pablo et al., 2003). Their structure and stiffness lead to a persistence length of ~5000 μm, much larger than typical cellular dimensions. MT are thus more suitable to withstand compression stresses (Stamenovic et al., 2002; Wang et al., 2002).

Although MT are present in most of animal and vegetal cells, their concentration is much lower than that of AF. The polarized structural nature and the polymerization dynamics of MT strongly determine their organization within the cell. The so-called *plus* end exposes β-tubulin, and tubulin dimers are added more rapidly than to the *minus* end, which exposes α-tubulin. The minus end is usually anchored to an amorphous matrix of filaments located near the nucleus called centrosome from which MT radiate out. MT are dynamically instable, the plus end abruptly changes from phases of linear growth to shrinkage in a random manner. As they form and disassemble MT can find a preferable orientation if their plus ends are capped, usually near cell borders. It has been observed that MT occasionally bend and flex at periphery in culture fibroblasts (Howard and Hyman, 2003). The disruption of MT using drugs such as nocodazole or colchicine induced a slight drop in cell stiffness and an increment in the inward or contraction forces (Buscemi, 2004; Stamenovic et al., 2002; Charras and Horton, 2002a; Thoumine et al., 1996). This findings show the importance of MT in cellular mechanics, and they support the hypothesis of MT as cell responsible structures for supporting compression forces.

In addition, MT have a key role in cellular trafficking. Molecular motors such as kinesin or dynein transport proteins and even whole vesicles and organelles along MT to the different regions of the cell. The step size of a single kinesin motor while it moves along a MT is ~8 nm, generating a force of ~7 pN with an energetic efficiency of 40-50% (Bustamante et al., 2004). Another important function of MT is to move chromosomes and mitotic spindles to opposite sites of the cell during mitosis, leading to strongly differentiated MT organization depending on the cell phase. This movement is generated by both MT polymerization and motor proteins. Cilia and flagella are molecular machines that generate force and movement in certain cell types, and are mainly formed by a thick core of MT.

Intermediate filaments and related proteins

The third kind of proteins that form the CSK are intermediate filaments (IF). They are much more varied in sequence and structure than AF or MT. Indeed, there are more than fifty different types of IF, such as vimentin, keratin, desmin, neurofilaments, or lamins. However, all these kinds have a similar structure formed by coiled-coil dimers. Assembly of IF is based on phosphorylation of the terminal domains of the dimers that interlace

between each other by longitudinal annealing forming a rode-like structure. Unlike AF or MT, IF are not polar structures. The diameter of IF is ~10 nm and their persistence length is ~1 μm. The Young's modulus of IF dimers has been estimated to be of ~2 GPa (Howard, 2001), although a dramatically lower value of 6.4 MPa has been recently reported for hydrated IF, which may explain the short persistence length observed in living cells (Fudge et al., 2003).

The structure, organization, and composition of IF vary from one cell type to another. IF are usually bonded to other parts of the cytoskeleton via linking proteins, such as desmoplakins, filaggrin, or plectins, forming an integrated system. In epithelial cells, for instance, keratin filaments form a network throughout the cytoplasm with higher concentration near the central region, being connected to neighboring cells by specific structures at the cell junctions. Their mechanical properties suggest that IF may contribute to the elasticity of the cells via tensile loading. Their contribution may be negligible at low strains, becoming more important at high loadings (Maniotis et al., 1997). It has been also suggested that IF may prevent from excessive buckling of MT, stabilizing the CSK and having a protective role (Stamenovic and Ingber, 2002). Disruption of the vimentin network of cultured osteoblasts using acrylamide, showed a trend toward reducing cell elasticity, reducing significantly both cell height and cellular reactions (Charras and Horton, 2002a). In addition, IF are also found to tailor the shapes of particular cells, such as neurons, determining axons diameter. Even though, the function of IF, not only mechanical, remains unclear, and further studies may be carried out to establish a satisfactory theory for these complex structures.

Several authors have tried to explain cellular mechanics in terms of measuring the mechanical properties of actin gels (Storm et al., 2005; MacKintosh and Schmidt, 1999; Janmey, 1991; Schnurr et al., 1997; Gittes et al., 1997). However, it seems difficult to find a complete and satisfactory explanation to cell mechanical behavior by means of individual CSK components. The complexity of cellular mechanics comprises its structural organization, cross-linking between filaments, attachment to other cells and to the extracellular matrix, and cooperativity with other cellular organelles. It seems thus important the *in situ* measurement of cellular mechanics under physiological conditions.

1.1.2 Extracellular matrix

The extracellular matrix (ECM) can be seen as an external extension of the CSK. The ECM is a dense mesh formed by several kinds of protein fibers, such as fibronectin, collagen, or laminin secreted by cells themselves. The diameter of the components of this network range from tens to hundreds of nm. Cells attach to the ECM via focal adhesion

contacts, which are clusters of membrane receptors (integrins) and cytoplasmic molecules (see section 1.1.3) (Horwitz, 1997). An important component of ECM is the aminoacid sequence Arg-Gly-Asp (RGD), which is the binding site for several integrin receptors to ECM fibers.

The composition of the ECM depends primarily on the tissue type. Its stiffness is mainly determined by collagen fibers and it is of the same order of magnitude of that of living cells, 100-1000 Pa. The ECM serves as a supporting scaffold for cells when forming living tissues. It has been shown that the density of ECM proteins strongly determines movement, shape and stiffness of cultured cells as well as it causes strengthening of cell-ECM adhesion sites (Bhadriraju and Hansen, 2002; Choquet et al., 1997). Indeed, the ECM supports part of the mechanical forces within the CSK. The balance of forces between cells and the ECM regulates cellular shape, stiffness, and structural stability. Thus, the ECM appears crucial to the developing and function of living tissues, and therefore to the way cells sense and response to mechanical stimulus.

1.1.3 Cell adhesion receptors

As mentioned in the last section, cells behavior, function, movement, and mechanical properties is determined by the specific attachments to their surroundings. Cells form tissues by adhering to neighboring cells and to the ECM. There is a wide amount of adhesion receptors and related structures. Integrins, cadherins, immunoglobulin cell adhesion molecules, and selectins lie among the most important adhesion sites. The adhesion molecules most related to the support and application of mechanical forces, critical for motility, or contraction, and related to the maintenance of the tissue integrity will be briefly reviewed in this section (Bershadsky et al., 2003).

Integrins and focal adhesions

Integrins are heterodimers having an α and a β subunit. Both subunits have a large extracellular domain, a membrane region, and a short cytoplasmic domain. In vertebrate cells, the integrin receptor family includes at least 18 varieties of α subunits and 8 β subunits. An important characteristic of integrins is their ability to move within the membrane and carry conformational changes as a response to extracellular and intracellular factors, leading to states with different avidity and affinity (Juliano, 2002; van Kooyk and Figdor, 2000). Although some kinds of integrins attach to other cell receptors, such as LFA-1 to ICAM-1, integrins main function is related with adhesion to the ECM. The strength of single integrin-ECM interactions has been studied by several authors on both isolated

molecules and living cells using AFM. The rupture forces for these single complexes has found to be Mg^{2+}-dependent, loading rate dependent and on the order of tens of pN (Lehenkari and Horton, 1999; Li et al., 2003; Kokkoli et al., 2004; Trache et al., 2005).

The cytoplasmic region of integrins is indirectly connected to the actin cytoskeleton via linking molecules such as talin, vinculin, or filamin (Horwitz, 1997; Critchley, 2000). This linkage to the CSK regulates integrin diffusion and clustering. Indeed, integrin mediated cell adhesion to the ECM is commonly mediated by clusters of integrins and other cytoplasmic molecules forming complex, specialized structures termed focal contacts or focal adhesions (FA) (Horwitz, 1997; Critchley, 2000). The formed complexes related with adhesion receptors serve as scaffolds for signaling cascades, and as major sites of force application. The area of these FA is of $\sim 1\ \mu m^2$. However, size and strength of FA are modulated by the cell depending on the mechanical properties and biochemical composition of the ECM (Choquet et al., 1997; Galbraith et al., 2002). Stress fibers are usually associated to FA and the forces generated by cells can be measured using different techniques, such as traction microscopy using flexible gels, patterned elastomers, or arrays of bendable posts on which cells are cultured (Balaban et al., 2001; Dembo et al., 1996; Tan et al., 2003). Using such techniques the force per unit area generated by different cells has been estimated to be in the range between 1 to 10 $nN/\mu m^2$.

Cadherins and related complexes

Cadherins form an important family of cell-cell adhesion receptors. As integrins, cadherins are specialized molecules characteristic of the cell type, existing E-cadherins and VE-cadherins, on epithelial and vascular endothelial cells. Cadherins are also transmembrane receptors, having and extracellular region which attaches to other cells, and a cytoplasmic region bound to the CSK via catenin, vinculin and other specialized proteins. An interesting feature of cadherins is their ability to form homophyllic (self-self) connections. The interaction force of single cadherins have been recently probed with AFM and found to be loading rate dependent, Ca^{2+}-dependent, and in the range 35–55 pN.

Cadherins also form structured complexes bound to the CSK. When linked to AF the complexes are called adherens junctions (AJ), and desmosomes when connected to IF. AJ and desmosomes are different from FA in structure and localization, and also less studied. In epithelial cells, AJ are localized between the apical and the basal domains of the cell, forming a continuous adhesion belt (or zonula adherens) connected to surrounding cells and associated with a cytoplasmic plaque of actin (Knust and Bossinger, 2002). AJ are found to be important in the balance of forces in living tissues due to their link to the CSK. AJ are commonly associated with other structures, called tight junctions (TJ), formed by

a different kind of adhesion molecules (occludins, ZO-1...) (Mitic and Anderson, 1998). These complexes also form a belt above AJ which is thought to be the responsible of the permeability of epithelial and endothelial layers.

1.1.4 Cytoplasm

The cytoplasm of vertebrate cells is composed by water with a 20-40% (w/v) of proteins. This high concentration of molecules lead to a crowded cell interior, in contraposition with the classical view of the cell as a balloon full of water with freely moving molecules. Recent developed microscopy techniques enabled us to visualize the cytoplasm with high resolution and with few changes from its native structure and composition (Medalia et al., 2002). Cryoelectron tomography images of *Dictyostelium discoideum* cells revealed a dense cell interior which has lead to a new term to described the cell cytoplasm *molecular crowding* (Ellis and Minton, 2003). This dense organization implies that between 5% and 40% of total cell volume is occupied by macromolecules, which may compete between each other to occupy the available volume. Although the implications of macromolecular crowding have not been already studied in detail, it seems likely an important contribution to the overall cellular viscoelasticity. Measurements of the cytoplasmic viscosity were carried out in the 1950s by Crick and Hugues using micrometer sized particles embedded within the cell cytoplasm (Crick and Hughes, 1950). More recent measurements on direct cytoplasmic extracts from *Xenopus laevis* eggs using conventional rheometers reported an elastic modulus of 2-10 Pa and a loss modulus of 0.5-5 Pa (Valentine et al., 2005), an order of magnitude lower than that of typical cells. At the microscopic level, cytoplasmic extracts behaved as viscous fluids with a viscosity of ~20 mPa·s.

1.1.5 Nucleus

The nucleus of vertebrate cells is formed by a lipid membrane and encloses the genetic material densely packed in the form of chromosomes. AF, MT, and IF surrounds the nucleus at higher concentration than in other cellular regions. The mechanical properties of cell nucleus have been studied by different techniques founding a stiffness higher than that of living cells (Caille et al., 2002; Dahl et al., 2005). Due to the importance of the nucleus in the organization of the CSK it seems difficult to isolate its contribution to cellular mechanics. Indeed, it has been shown that cells nucleus is directly linked to the CSK and indirectly to the cell membrane via integrins (Maniotis et al., 1997). Thus, forces applied to the cell contribute to the deformation of the CSK and to the indirect deformation of the cell nucleus, contributing to the mechanical response of living cells.

1.1.6 Cell membrane

The cell membrane is formed by a lipid bilayer with integrated protein molecules of different type and function. The area of the lipid layer forms the 50% of the total membrane surface. The lipid bilayer serves as a semipermeable barrier between cells and their microenvironment. Water and small molecules (O_2, CO_2) are able to pass through the cell membrane. Another important task of the cell membrane is the regulation of the osmotic equilibrium. The embedded molecules serve as receptors, enzymes, or transport proteins. Both lipid and protein molecules can diffuse within the membrane, which can be seen as a two-dimensional fluid. Using membrane attached beads, this kind of diffusion have been studied. It has been shown that lipid-attached beads diffused randomly, while protein-attached beads diffuse in the same way initially with sudden stationary states, explained by the anchoring of the proteins to the CSK (Bursac et al., 2005). The tension supported by a lipid bilayer has been calculated to be ~1 nN/μm using the micropipette aspiration technique. Similar measurements on living cells revealed a softer tension for the cellular cortex of ~1 pN/μm (Hochmuth, 2000). The surface tension contributes to the whole mechanical properties of living cells and may control cellular functions, such as endocytosis and exocytosis. Due to the close binding of the cell membrane with the actin cortex and other attached molecules, it is difficult to isolate the purely elastic behavior of the cell membrane. It has been shown that cell membranes, probed using AFM and micropipette aspiration, form long tethers of several μm that oppose a force to pulling independent of extension (Hochmuth, 2000; Benoit et al., 2000; Benoit and Gaub, 2002). Poking measurements on living cells reflected forces from hundreds of pN to tens of nN needed to lyse cell membranes using AFM tips (Hategan et al., 2003; Obataya et al., 2005a). Another contribution to cell mechanical properties is the glycocalix composed mainly by chains of polysaccharides. These brush-like structures developed steric forces that have been studied using AFM (Fritz et al., 1994). The contribution of the cell membrane to cellular mechanics seems complex and might need further study.

1.2 Atomic force microscopy applied to cell biology

Our knowledge of the mechanics of the cell has increased in the recent two decades due to the emergence of the nanotechniques. These tools enables us to manipulate biomolecules and cells with nanometer resolution and simultaneously measure forces on the picoNewton to nanoNewton range. Moreover, most of the emerged tools allows us to carry out measurements under liquid environment. Among the most important tools we find magnetic and optical tweezers (Wang et al., 1993; Maksym et al., 2000; Neuman and Block,

2004), microplates (Thoumine et al., 1999), traction microscopy (Dembo et al., 1996; Butler et al., 2002b; Roy et al., 2002), micropipet aspiration (Evans and Yeung, 1989), microarrays of bendable posts made of silicon or PDMS (polydimethilsiloxane) (Tan et al., 2003), and atomic force microscopy (AFM) (Binnig et al., 1986). The last one is one of the most versatile since it enables us to obtain both topographical images and mechanical measurements under physiological conditions at the nanometer and picoNewton scales.

AFM appeared in 1986 and it was originally designed to obtain topographical images of surfaces (Binnig et al., 1986). AFM was rapidly applied to measure the mechanical properties of different samples (Burnham and Colton, 1989). The possibility of working under liquid conditions made AFM straightforwardly applied to the study of structural properties of cells (Haberle et al., 1991; Henderson et al., 1992; Butt et al., 1990). The application of AFM to probe the mechanics of biological samples arrived in 1992. Tao and co-workers applied the atomic force microscope to probe the microelasticity of soft biological samples (Tao et al., 1992), and Hoh and co-workers used AFM, for the first time, to measure the mechanical properties of living cells (Hoh and Schoenenberger, 1994). After these works, a great amount of studies appeared, and continue to appear, to study the morphology and the mechanical properties of living cells under different conditions, as well as various novel methods and techniques to improve measurements on biological samples, and specially on living cells (Dimitriadis et al., 2002; Dvorak, 2003; Domke et al., 2000; Charras and Horton, 2002b; Florin et al., 1995; Horton et al., 2000; Hoh and Schoenenberger, 1994; Lehenkari et al., 2000; Mathur et al., 2001; Rotsch and Radmacher, 2000; Obataya et al., 2005b; Mahaffy et al., 2000; Wojcikiewicz et al., 2003; Zhang et al., 2004a; Lee and Marchant, 2000; A-Hassan et al., 1998; Wu et al., 1998; Han et al., 2005; Benoit and Gaub, 2002; Cappella and Dietler, 1999; You et al., 2000). Even though, a series of limitations arise in practical use, specially when using commercial systems. In this section, we briefly review the most common AFM methods and techniques to obtain both topographical images and mechanical measurements on living cells, emphasizing on the limitations that arise in the day to day use.

1.2.1 Principle of operation

AFM makes use of a flexible cantilever with a sharp tip at its end to probe the sample surface (Fig. 1.1). In the case of AFM systems specially designed to investigate biological samples, the cantilever is positioned in the three dimensions by means of piezoelectric elements. The deflection of the cantilever is measured using the optical lever method (Hansma et al., 1994b). A laser beam is reflected off the back side of the cantilever and detected using a segmented photodiode. The deflection is transformed into force invoking

the Hooke's law and knowing the spring constant of the cantilever. Other configurations use piezoelements to move the sample maintaining the probe fixed. A key feature when handling living cells is the simultaneous visualization of the samples by transmitted light microscopy (Putman et al., 1992). An illustrative scheme of a typical AFM system is shown in Fig. 1.1.

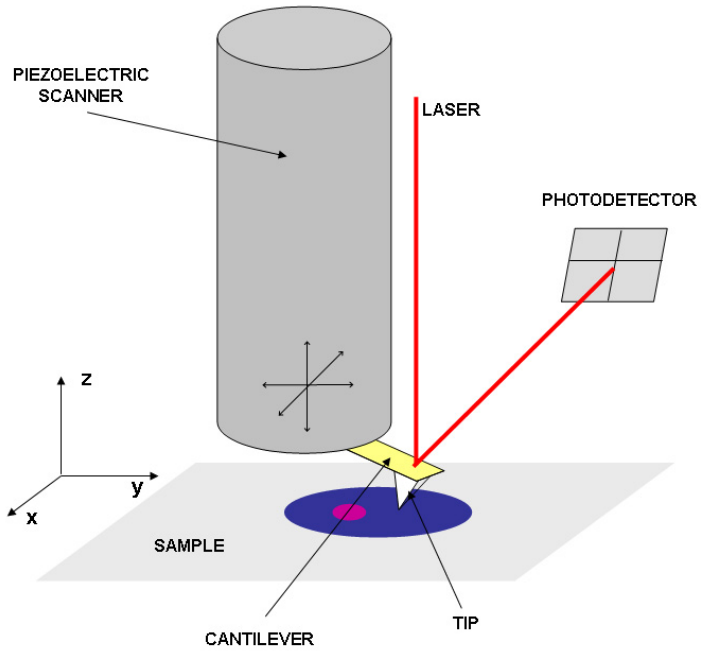

Figure 1.1: Sketch of an typical atomic force microscopy device designed for biological applications.

1.2.2 Imaging living cells

As mentioned above, AFM and its precursor scanning tunnelling microscopy, was firstly applied to obtain topographical information of hard surfaces in air (Binnig et al., 1986). However, its capability of imaging non conducting surfaces in liquid conditions induced its immediate application to biological specimens. AFM is indeed mostly used as an imaging technique, specially in the field of material sciences.

AFM images are obtained by scanning the sample surface with the cantilever tip (Fig. 1.2) at a fixed force. The maintenance of the force level is achieved by using feedback electronics (usually digital proportional integral circuits) continuously correcting the vertical position of the cantilever (relative to the sample) as the input signal varies due to topographic obstacles. The sample topography is reconstructed from the vertical movements used to maintain the fixed force set point. The different imaging modes available

depend on the input signal used in the feedback circuit to control the vertical position. The two main modes used in biology are *contact* and *intermittent contact* (IC or *tapping*) modes, which will be briefly discussed in the following. Other techniques and improvements have been introduced such as magnetic modulation, frequency modulation, or ultrasonic force microscopy (Florin et al., 1994; Albrecht et al., 1991; Yamanaka et al., 1994).

IC-mode consists in making oscillate the cantilever at its resonant frequency (few kHz) (Zhong et al., 1993). Under liquid conditions, the driving oscillation is usually applied by the same piezoelement that controls the vertical position. When imaging living cells with soft cantilevers (~10 pN/nm) the driving oscillation leads to a cantilever deflection amplitude of few tens of nanometers. The driving amplitude of oscillation is adjusted depending on the characteristics of the sample. The scanning is carried out by using the amplitude signal for the feedback. IC-mode is applied when low shear and lateral forces are required. In this mode the tip taps the sample only intermittently leading to lower perturbation and reduced shear forces as the tip scans the sample. In the case of living cells, IC-mode takes advantage of the mechanical properties of living cells. At the resonant frequencies of the cantilevers, cells behave almost as a viscous fluid. Therefore, the force exerted by the cell is proportional to the velocity at which it is probed leading to apparently higher forces when imaging in IC-mode (Burnham et al., 1997; Hansma et al., 1994a; Putman et al., 1994). Even its suitability for acquiring images of living cells without damaging them, IC-mode images have low lateral resolution and it is difficult to resolve cellular structural components, such as the CSK. However, IC-mode may be useful when morphological parameters (perimeter, area, volume) are intended[1].

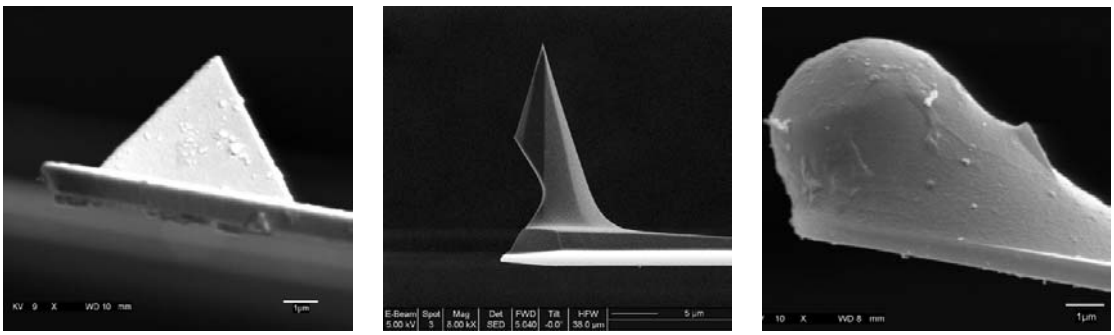

Figure 1.2: Commercially available AFM cantilever probes. 4-sided pyramidal (left), 8-sided pyramidal (center), and a pyramidal tip with a polystyrene sphere attached.

Contact mode is commonly used when high lateral resolution is desired. Imaging mode, tip sharpness, sample stiffness and applied force determine the maximum lateral

[1]To see a graphical simulation of IC-mode provided by Digital Instruments click here

resolution that can be reached. In contact mode, soft cantilevers (k ~0.01 N/m) carrying sharp pyramidal tips (with an apex radius <50 nm), low tip velocities (<100 μm/s) and applied forces of few hundreds of pN are desired to obtain lateral resolutions of tens of nm on living cells. However, to obtain good contrast of the underlying CSK, higher forces might be applied (Hoh and Schoenenberger, 1994). The immobilization of the samples is also important when non adherent cells are imaged. Immobilization can be achieved by using imaging buffers to vary the electrostatic charge of both sample and surface (*e.g.*, Hanks' Balanced Salt Solution), or by chemical modification of the substrate (*e.g.*, 3-aminopropyl-triethoxysilane) (Wagner, 1998). When working with adherent cells, the use of substrate coatings such as fibronectin or collagen and the increase of the culture time may help to enhance cell adhesion to the substrate. AFM images bring us quantitative information such as height, perimeter or volume of living cells together with structural details of the surface and the inside of the cells, *e.g.*, cytoskeleton. The possibility of changing the liquid environment while imaging makes AFM an excellent tool to track structural and dimensional responses of living cells under drug treatment. Figure 1.3 shows a living alveolar epithelial cell imaged in contact mode under liquid conditions[2].

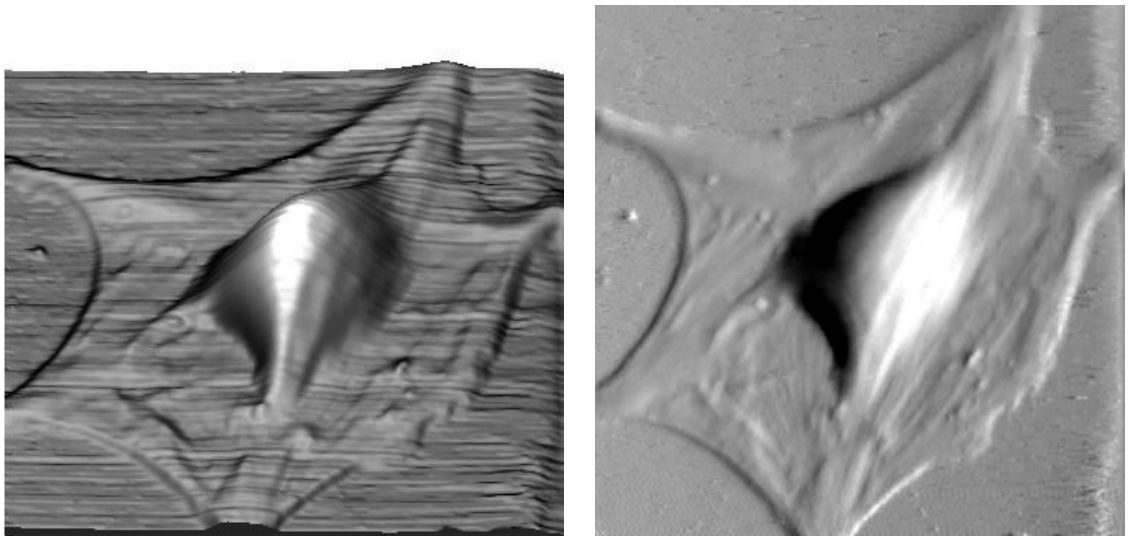

Figure 1.3: 3D height (left) and deflection (right) images of a primary alveolar from rat under liquid conditions. Cell thickness was ~4 μm. Deflection gray scale stands 200 nm, respectively. Scan size was 100 μm. Images were obtained using a Bioscope system operated in contact mode with a pyramidal cantilever tip (k = 10 mN/m) (Veeco, Santa Barbara, USA)

As mentioned above, AFM images are obtained by scanning the sample surface with the cantilever tip continuously correcting the vertical position (height) as the deflection

[2]Primary cells were provided by Isaac Almendros. Images were processed using freeware software WSxM 7.5 (Nanotech, Madrid, Spain).

(in contact mode) or amplitude (in IC-mode) vary as a result of sample topography. If the feedback circuiting was ideal, the error signal might be constant during the scanning. However, the response of actual PID circuits depend on the good tuning of the proportional and integral values and on the properties of the cantilever and the sample. Thus, error signal are not constant but provide images that can reflect properties of the sample. Depending on the imaging mode, error images provide information about minute corrugations of the sample surface (deflection in contact mode) or viscoelastic properties of the sample (amplitude in IC-mode)[3]

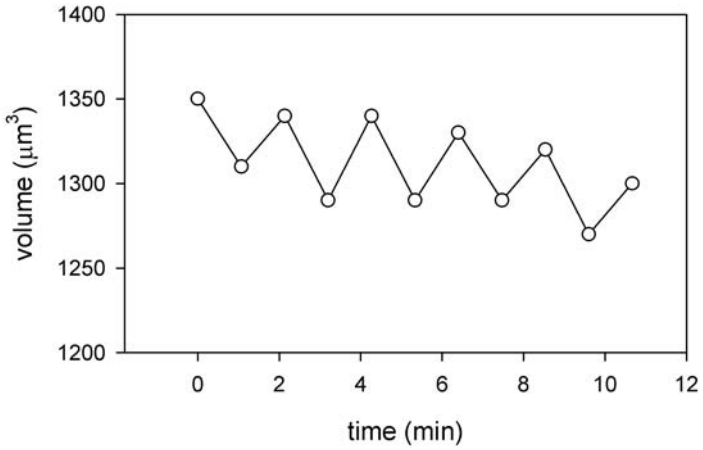

Figure 1.4: Volume of a living A549 cell computed from contact mode AFM images obtained using a Bioscope system (Veeco, Santa Barbara, USA) with V-shaped cantilever (k=10 mN/m). The low resolution (64x64 pixel) and a scan rate of ~100 μm/s allowed us to obtain an image every ~1 min. The hysteresis of the piezoelements introduces a systematic artifact in the volume value obtained from the upward (odd) or the downward (even) images of ~5%. The slight decreasing trend may be due to relaxation of the cells.

One of the main limitations of AFM imaging is its low acquisition rate, specially in the case of large samples (tens of microns), such as living cells. High resolution images of living cells can last several minutes, and are thus restricted to low cellular changes. However, low resolution images still provide quantitative dimensional information with a time resolution of one or two minutes (Schneider et al., 2000; Bhadriraju and Hansen, 2002). Drift artifacts due to thermal deformations of both AFM system and samples are commonly observed in AFM imaging. These effects may be minimized by thermal stabilization of the whole system, even if it is usually difficult on living organisms. Piezoelectric elements also introduce creep and hysteresis effects when imaging large samples.

[3]The interpretation of AFM error images arouse still an intense debate, specially on IC-mode amplitude and phase images.

An illustrative example is shown in Fig. 1.4, where it is shown the cell volume computed from a series of AFM images acquired every ~1 min. Notice that there is a systematic artifact in odd and even images, mainly due the hysteresis of piezoelectric scanners. The utilization of position sensors (such as strain gauges or capacitors) and feedback circuits dramatically minimizes these effects, although it also reduces the time response of the system. For this reason, many of the ultimate commercial equipments introduce servo-controlled positioners. In the special case of living cells, it is important the simultaneous optical visualization of the samples with common optical systems, such as Phase Contrast (PhC), Differential Interference Contrast (DIC), or epi-fluorescence. Commercial AFM systems are commonly difficult to combine with these techniques, reducing their applicability to cell biology.

1.2.3 Mechanical measurements

Apart from imaging purposes, AFM is widely used as a force sensor, detecting forces ranging from tens of picoNewtons to hundreds of nanoNewtons, which is the range involved in cell mechanics. Mechanical measurements use to be obtained by applying triangular oscillations in the vertical direction and measuring the resulting deflection as the tip contacts the sample. The deflection is translated into force using the spring constant of the cantilever which ranges from few mN/m to hundreds of N/m. The obtained curves are commonly known as force-distance ($F-z$) curves, or simply force curves (Fig. 1.5). The analysis of the approaching or loading and the retracting or unloading curves provides information about the elastic and adhesion properties of the sample, respectively, although different information can be extracted from them[4]. The most used AFM methods to study viscoelasticity and adhesion of living cells are explained below.

Viscoelastic measurements

The approaching part of a force-distance plot follows a nonlinear profile (Fig. 1.5). The nonlinearity does not stand for nonlinear behavior of the sample, but is mainly determined by the tip geometry (Fig. 1.2). Commercially available tips used to be pyramidal or conical shaped (Olympus, Tokio, Japan; Vecco, Santa Barbara, USA; MikroMasch, Tallinn, Estonia). Modified cantilevers with spherical beads attached at their ends can also be obtained (Novascan, Ames, USA). All these geometries lead to nonlinear force-indentation ($F-\delta$) relationships, the force increases as the tip indents the sample as a result of the increasing area of contact between the tip and the sample. The $F(\delta)$ relationships obtained

[4]For an extensive and detailed review of AFM force-distance curves see Cappella and Dietler (1999)

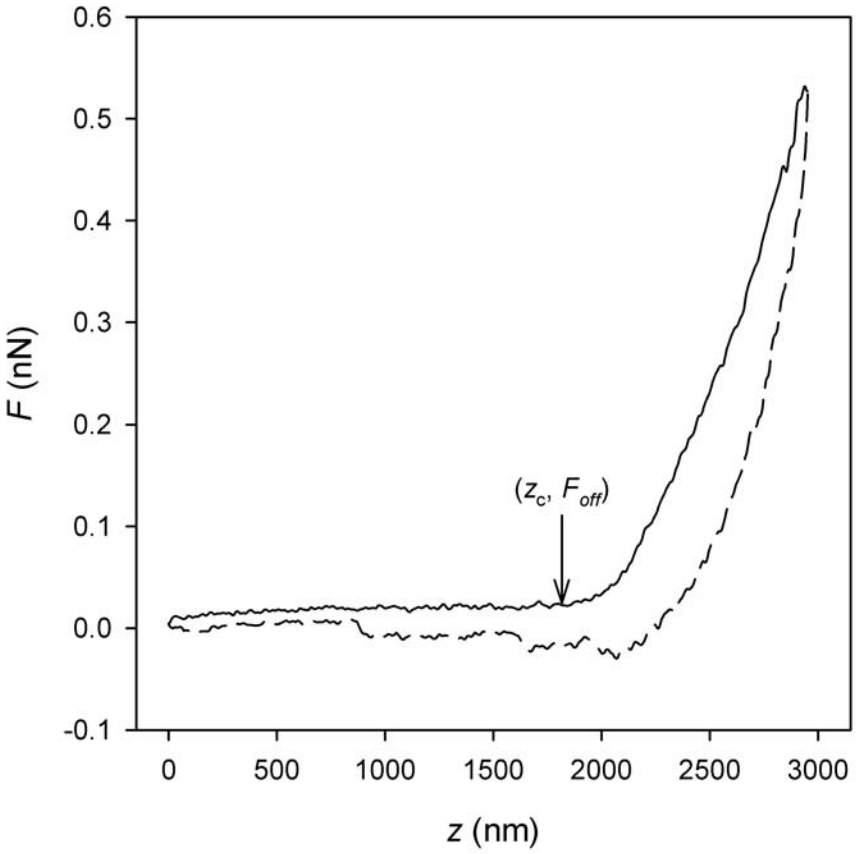

Figure 1.5: Example of a force-distance ($F-z$) curve obtained on a living alveolar epithelial cell using a V-shaped cantilever with pyramidal tip (k=0.01 mN/m). The approaching curve profile is mainly due to the geometry of the tip. The negative values in the retracting curve reflect various adhesion events. The shift in force in the non contact region between approach and retract is due to the viscous drag of the fluid on the cantilever.

with the various tip geometries is described by a contact elastic model of a rigid punch indenting an elastic half space. Heinrich Hertz was the first who described and solved the problem of two elastic bodies in contact (Hertz, 1881), and Sneddon solved the problem for different tip geometries (Sneddon, 1965). Table 1.1 summarizes the most relevant contact elastic models described in the literature. Note that the unique model that lead to a linear force response is that of the cylindrical punch, since its area remains constant during indentation.

The most common approach to obtain the elastic modulus or Young's modulus (E) of living cells is described below[5]. First, the F-z curves are transformed into $F-\delta$ curves by

[5]Different approaches are found in the literature to measure the mechanical properties of samples (Stolz et al., 2004; Pharr et al., 1992; A-Hassan et al., 1998). However, the here described method is the most extended when probing the mechanical properties of living cells.

Tip geometry	Force-indentation relationship, $F(\delta)$
Sphere of radius R	$F = \frac{4E}{3(1-\nu^2)} R^{1/2}\delta^{3/2}$ (Hertz, 1881)
Cone of semi-included angle θ	$F = \frac{2E\tan\theta}{\pi(1-\nu^2)}\delta^2$ (Sneddon, 1965)
Flat ended cylinder of radius a	$F = \frac{2E}{(1-\nu^2)} a\delta$ (Sneddon, 1965)
Four-sided regular pyramid of semi-included angle θ	$F = \frac{0.7453E\tan\theta}{(1-\nu^2)}\delta^2$ (Bilodeau, 1992)

Table 1.1: Contact models for common tip geometries. E and ν are Young's modulus and Poisson ratio of the sample, respectively.

computing the indentation of the tip into the sample, determining the point at which the tip contacts the sample (point of contact). Second, the suitable contact elastic model to the geometry of the tip is fitted to the loading part of the curve. Choosing the approaching part prevents from possible artifacts related to adhesion observed in the retracting region. Due to the nonlinearity of the force response, two issues are crucial for a reliable estimation of E: the determination of the point of contact and the suitability of the contact model to the actual tip geometry (Touhami et al., 2003; Mahaffy et al., 2000; A-Hassan et al., 1998; Costa and Yin, 1999; Briscoe et al., 1994). The point of contact is defined by the force (or deflection) offset (F_{off} or d_{off}) and the vertical point at which the cantilever starts to deflect (z_c) (Fig. 1.5). As can be observed in the figure, in the case of soft samples, the point of contact is difficult to determine visually due to the smooth deflection of the cantilever at low indentations. Thus, an objective estimation of these parameters should be established.

Even if the Young's modulus is a reliable estimate of cell stiffness, as will be described in Section 1.3, cells are not elastic bodies but viscoelastic. Several authors have measured the viscoelasticity of living cells by applying force or deformation steps and measuring the corresponding response (Bausch et al., 2001; Wu et al., 1998; Thoumine and Ott, 1997). The main limitation of these approach is that the obtained mechanical parameters are limited by the width of the time window used during the measurements. A more robust method to probe cell viscoelasticity is the application of low amplitude oscillations at a wide frequency range to estimate the complex shear modulus G^* . The complex shear modulus is divided into a real or in-phase component, which stands for the elasticity or the stored energy, and an imaginary or out-of-phase component, which stands for the viscosity or lost energy. The real part is known as the elastic modulus (G'), while the imaginary part is called the loss modulus (G''). The oscillatory technique has been successfully applied to a wide variety of living cells including lung epithelial cells, airway smooth muscle cells, macrophages, and neutrophils in basal conditions and under mechanical or

pharmacological treatment (Maksym et al., 2000; Fabry et al., 2001; Mahaffy et al., 2000, 2004; Alcaraz et al., 2003; Desprat et al., 2005; Smith et al., 2005; Trepat et al., 2004).

The oscillatory technique used in AFM measurements on living cells consists in applying low amplitude oscillations (50-100 nm) at an operating indentation (δ_0). Under these conditions, the contact elastic model described by $F(\delta)$ can be approximated taking the first two terms of its Taylor expansion

$$F \simeq F(\delta_0) + \frac{\partial F}{\partial \delta}(\delta - \delta_0) + ... \tag{1.1}$$

In the case of a flat ended cylindrical tip of radius a, the above expansion leads to

$$F = F_0 + \frac{2E}{(1-\nu^2)} a(\delta - \delta_0). \tag{1.2}$$

Expressing Eq. 1.2 in terms of the complex shear modulus $G = E/(1-\nu^2)$ and solving for G we obtain

$$G^*(\omega) = \frac{1-\nu}{4a}\frac{F - F_0}{\delta - \delta_0} \tag{1.3}$$

by invoking the Parseval theorem, Eq. 1.3 can be transformed into the frequency domain to obtain an expression for the complex shear modulus

$$G^*(\omega) = \frac{1-\nu}{4a}\frac{F(\omega)}{\delta(\omega)} \tag{1.4}$$

where ω is the angular frequency ($\omega = 2\pi f$), and $F(\omega)$ and $\delta(\omega)$ are the fourier transforms of force and indentation, respectively.

When probing biological samples under liquid conditions the hydrodynamic drag force exerted on the cantilever should be corrected at frequencies above ~0.3 Hz (Alcaraz et al., 2002). The drag force depends on the geometry of the cantilever, by the drag factor $b(0)$, and on the velocity of the cantilever free end $v = \frac{d\delta}{dt}$. It can be expressed by $F_d = b(0)v$. As described in the work by Alcaraz and co-workers, the drag factor increases as the tip approaches the surface. The factor $b(0)$ is usually obtained by applying low amplitude oscillations at different heights above the sample surface and extrapolating to zero separation (Smith et al., 2005; Alcaraz et al., 2003, 2002). The hydrodynamic drag contribution in the frequency domain has the form $F_d(\omega)/\delta(\omega) = i\omega b(0)$ (where $i = \sqrt{-1}$), and may be included into Eq. 1.4 to correct for the drag force, obtaining

$$G^*(\omega) = \frac{1-\nu}{4a}\left[\frac{F(\omega)}{\delta(\omega)} - i\omega b(0)\right]. \tag{1.5}$$

Due to the softness of living cells, mechanical measurements have to be carried out

using soft cantilevers (tens of mN/m) to apply low forces usually below 1 nN. Another important factor to take into account is the thickness of the cells. Living epithelial cells plated on glass coverslips have a thickness of 5-10 μm. Thus, the indentation might also be controlled in order not to sense the underlying hard substrate (Domke and Radmacher, 1998). The maximum indentation reachable when measuring soft samples without sensing the hard substrate can be estimated to be 10-20% of sample thickness.

Adhesion measurements

Cell adhesion is mediated by a collectivity of single binding molecules that adhere to neighboring cells or to the extracellular matrix in a specific manner. Therefore, cell adhesion measurements can be addressed at two levels of interaction: single molecule and multiple molecule. The principle of operation of adhesion measurements by AFM is the same for both levels. The method consists in measuring the interaction force by obtaining force curves using the AFM cantilever. For that purpose, different strategies have been used in cell measurements. The simplest method is the functionalization of the cantilever tip with molecules specifically recognized by the cell. This is the common approach when probing adhesion between living cells and extracellular matrix proteins (Lehenkari and Horton, 1999; Hyonchol et al., 2002). Another technique consists in attaching a cell to the cantilever end and bringing it into contact with a functionalized surface (Wojcikiewicz et al., 2003). The technique has been used to measure the interaction at both single molecule and multiple levels between living T-cells (3A9) and the intercellular adhesion molecule-1. The most realistic and physiologically relevant procedure consists in attaching a cell to the cantilever and make contact with a cultured monolayer. This last method has been applied to study the interaction between leukocytes and endothelial cells (Zhang et al., 2004a).

Single molecule measurements are carried out by obtaining force curves and measuring the rupture force of the adhesion events. Force curves may be obtained at low indentation force to reduce the area of contact and, thus, the binding probability. Due to the stochastic nature of bond rupture, hundreds of measurements need to be averaged to obtain reliable results (Li et al., 1993; Lehenkari and Horton, 1999; Moy et al., 1994b; Benoit et al., 2000; Kokkoli et al., 2004). It has been shown that an adhesion frequency of <30% in the force measurements ensures a probability of >85% of dealing with single molecule events (Tees et al., 2001). Interaction forces involved in single molecule measurements range from tens to hundreds of picoNewtons. The noise level of a force curve due to thermal fluctuations, mechanical perturbations of the system, and turbulence of the liquid is of the order of tens of pN, using a cantilever of few mN/m. Thus, interaction

events involving forces below this level are hardly detectable by AFM and they are usually rejected. As described by Evans and Ritchie and observed by several authors, the rupture force depends on the loading rate, or the rate at which applied force increases (dF/dt) (Evans and Ritchie, 1997). The loading rate is computed by measuring the slope immediately before the rupture takes place in a force-time plot. The loading rates assessed in living cell measurements usually range three or even four orders of magnitude, from tens of pN/s to hundreds of nN/s. This wide range is reached by varying the driving velocity of the cantilever. Due to the elasticity of both cells and adhesion molecules, the effective spring constant formed by the cantilever and the sample in series allows us to obtain the wide range of loading rates, although it makes difficult to control this parameter. It has to be said that, even if semi-automatic procedures have been proposed to detect and measure the rupture events, most of the current work is still done visually (Baumgartner et al., 2000b). This subjective method of data processing may introduce systematic errors in the results. Thus, an objective, automatic algorithm may be developed to obtain more reliable results.

In the case of multiple bonded attachments, the three simplest configurations might be mentioned: N identical bonds loaded in series, zipper-like attachment of N identical bonds, and N identical bonds loaded in parallel. The first configuration is common in protein unfolding measurements, in which each bond experience the same force and ruptures at random order (Rief et al., 1997). In a zipper the same force propagates from bond to bond after rupture of the lead bond takes place. Bond rupture occur in sequence at random times from first to last. Finally, for the parallel bonds arrangement, the force is divided among all the binding sites involved in the attachment. The last is the configuration which better describes multiple adhesion measurements obtained by AFM on living cells and it will be briefly described here.

Multiple adhesion on living cells is usually measured by keeping the sample and the cantilever in contact for few seconds and measuring the force and work required to detach the two surfaces (Wojcikiewicz et al., 2003; Zhang et al., 2002a, 2004a). Due to the large area of contact and to the long contact time, multiple bonds might be formed leading to multiple rupture events. The forces involved in multiple cell adhesion depend on the contact area, the time of contact, the loading rate, and the strength of the specific interaction. These forces are usually of hundreds of pN or few nN. Retraction curves usually present a peak of force followed by a cascade of rupture events until complete detachment. The maximum peak of force in the retracting curve determines the detachment force. The work of adhesion (or de-adhesion) is computed by the area under the unloading curve on a force-distance plot. The slope in a force-time plot just before the cascade of rupture

events occur provides an estimate of the loading force.

In both single molecule and multiple bonds measurements it is necessary to correct for the hydrodynamic drag force that introduces a systematic bias in rupture and detachment forces. As mentioned before, the drag force is proportional to the tip velocity and to the drag coefficient b. Both rupture and detachment forces are corrected by adding the amount $vb(h)$ to the measured peak of force. As the drag coefficient depends on the tip-sample distance (h) a previous calibration may be obtained to determine the correction factor taking h into account. However, the common procedure estimates a constant drag coefficient and uses it to correct for the drag force. At high loading rates (above 10 nN/s) this simpler approach may introduce important errors and might be avoided, especially in single molecule measurements where the drag force is of the same order of magnitude of molecular forces (Janovjak et al., 2005).

The main limitation of commercial AFM systems when measuring multiple adhesion is the low travel of the vertical piezoelements. Some cell measurements need the acquisition of force curves with an amplitude of tens of μm. The typical vertical range for commercial systems is 7 μm, being 14 μm in some apparatus designed for biological applications. When carrying out both single molecule and multiple adhesion assays, it is also critical the actual measurement of the vertical and lateral displacement, which is only possible with position sensors, such as strain gauges. Even the recent introduction of this technology in commercial systems, most of them use precalibrated piezopositioners that introduce important hysteresis effects and have low reproducibility. Adhesion receptors use to be distributed throughout the cell surface, but specially localized in certain regions, such as cell borders or cell-cell junctions. Thus, accurate positioning of the cantilever tip on these regions seems necessary, but difficult to obtain with commercial systems. Again, the difficulty to combine commercial systems with conventional optical microscopy techniques limits their applicability to cell adhesion studies.

1.3 Cell mechanics

Mechanics is a branch of physics that deal with forces. As such, mechanics studies strains due to applied stresses, to obtain elastic and viscous properties of materials. The adhesive properties of materials play an important role in their mechanical behavior. For that reason, most of the textbooks that deal with continuous and contact mechanics have a section to explain adhesion (Johnson, 1985). In the concrete case of cell biology, adhesive properties of living cells determine their viscoelastic response and viceversa. Moreover, a major division of living cells when dealing with mechanics is their availability to adhere

to surfaces talking, thus, about adherent cells and non-adherent or suspended cells. It seems thus difficult to isolate adhesion from viscoelasticity, in cell measurements. Thus, Even their interconnection, few are the studies that imply adhesion and viscoelastic measurements of living cells.

Due to the great body of evidence that forces are applied, transmitted, and balanced by living cells and their connections with other cells and the ECM, it seems likely that mechanics is an important field to study in cell biology. Mechanical properties of living cells are becoming as important as classical biochemical approaches to better understand how cells function (Huang et al., 2004; Janmey and Weitz, 2004). In this section, the major findings on mechanical[6] properties obtained on living cells are addressed, as well as the main models to explain cells mechanical behavior.

1.3.1 Cell microrheology

Rheology or viscoelasticity deals with the elastic and viscous properties of materials. Due to the micrometer size of the common used probes to study cellular mechanics, the use of the term microrheology is widely accepted.

Softness

Several viscoelastic measurements have been carried out on different cell types and using various probing technics and all of them coincide on one particular isuue: cells have extremely low stiffness values. In fact, we might talk about the *softness* of the cells, to emphasize this important characteristic. The range of stiffnesses found in living cells vary more than four orthers of magnitude, from tens of Pa to hundreds of kPa, finding such variation even within a same cell (Maksym et al., 2000; de Morales et al., 2004; Wu et al., 1998; Domke et al., 2000; Rotsch and Radmacher, 2000). This wide range of values may be due to the different types of cells, the structural heterogeneity of cells themselves, and the probing instrumentation. Adherent cells form part of tissues that have different functions and thus different properties. It seems logical that cells coming from mechanically different tissues may behave mechanically different. For instance, skeletal cells has been shown to be stiffer than endothelial cells (Mathur et al., 2001). Since cells are very heterogenic structures, their stiffness depends strongly on the probed region (Goldmann et al., 1998; Rotsch and Radmacher, 2000; Rotsch et al., 1997). Moreover, as we will discuss in the following, the rate at which cells are probed may also influence the obtained mechanical properties. In addition, the used technique to probe the mechanical proper-

[6] I understand mechanics as a discipline that comprises both viscoelasticity and adhesion.

ties may also induce a modification of the local stiffness. For example, the attachment of magnetic beads to the cell surface via integrin receptors applied in magnetic or optical tweezers measurements has been shown to induce local CSK reorganization (Fabry et al., 2001). This reorganization may be reflected in the mechanical measurements. The different assumptions adopted in each approach, such as the value of the Poisson ratio (usually assumed to be 0.5), the hypothesis of frictionless contact in AFM measurements, the supposed thickness of cells, or the description of cells as continuous materials may also be factors that determine the observed variability of cells viscoelastic properties.

Viscoelasticity

Another important property of living cells is the fact that cells behave not only elastically but also in a viscous manner, *i.e.* cells are viscoelastic. The viscoelasticity of living cells can be measured by different procedures. One of the most common is the application of a step of force or deformation and the measurement of the corresponding response. Using this simple approach, it has been observed that cells respond initially as an elastic body and then either force and deformation relax in time. Elastic and viscous moduli, damping factors, and relaxation times of living cells have been estimated using this technique (Thoumine and Ott, 1997; Bausch et al., 2001; Wu et al., 1998). A more robust approach to determine the viscoelasticity of materials is the application of controlled low amplitude oscillations. This method resulted in stress-strain loops with hysteresis reflecting the viscoelastic behavior of living cells. Both elastic and viscous response showed also to depend on the rate at which the deformation was applied, cells behaved stiffer when probed at higher rates. In particular, both G' and G" followed a weak power low at low frequencies, with G" approaching to a purely Newtonian fluid at frequencies above 100 Hz (Alcaraz et al., 2003; Smith et al., 2005; Fabry et al., 2001; Trepat et al., 2005; Goldmann and Ezzell, 1996).

The stress-strain relation of living cells has been shown to be fairly linear for low deformations or applied forces. When higher strains were applied, cells usually behaved nonlinearly, reflecting a higher apparent stiffness (Alcaraz et al., 2003; Mahaffy et al., 2000; Laurent et al., 2002; Wang et al., 1993; Rotsch and Radmacher, 2000). This effect may be due to the underlying hard substrate where adherent cells grow and to an inherent cellular characteristic, termed as *strain hardening*. This last concern is indeed controversial. Some authors have taken the observed effect of apparent higher stiffness of living cells probed at high indentations with AFM as an evidence of strain hardening (Stamenovic and Ingber, 2002). However, recent AFM measurements taking into account cells thickness have shown a linear behavior, even when cells were at indentation depths >50%

of their thickness (Mahaffy et al., 2004).

It is now widely accepted that living cells behave stiffer as their internal tensile stress (prestress) increases. This cell stiffening induced by prestress has been observed in a variety of cell types under different treatments which modified the internal prestress by both biochemical or mechanical stimulus (Wang and Stamenovic, 2002; Stamenovic and Ingber, 2002; Trepat et al., 2004; Pourati et al., 1998). Wang and co-workers state that living cells are structures that regulate their shape stability through the prestress. By regulating CSK prestress by treating cells with contractile and relaxing agonists, the authors found a linear relationship with stiffness (Wang and Stamenovic, 2002; Stamenovic and Ingber, 2002). In addition, they observed that partial detachment of endothelial cells from their substrate induced retraction, which did not occur when disrupting the actin CSK (Pourati et al., 1998). Moreover, viscoelastic measurements carried out on living cells cultured on deformable substrates showed increased stiffness when being stretched (a mechanical stymulus that may increase cells prestress) (Pourati et al., 1998; Trepat et al., 2004). These results confirm the hypothesis of a preexisting CSK tension (mainly concentrated in the actin CSK), which may play an important role in cells mechanical stability and stiffness.

Models of cell microrheology

From the constantly increasing models that pretend to explain the above described mechanical behavior of living cells, here are explained three of the most applied and contrasted experimentally.

Several studies have described the viscoelastic properties of living cells in terms of classical viscoelastic models composed of springs and dashpots. Some of these well known classical models comprise the Maxwell model, formed by a spring and a dashpot in series; the Voigt model, made of a spring and a dashpot in parallel; or the Kelvin model, a Maxwell body in parallel with an additional spring. These models have been applied using different probing techniques such as AFM or magnetic tweezers which applied a step of force or deformation to the cells (Wu et al., 1998; Bausch et al., 2001). The approach enables us to measure elastic and viscous properties described in terms of spring constants and viscous factors. As mentioned before, one of the limitations of this approach is that the results obtained are limited by the time window used during measurements (Desprat et al., 2005). In addition, the frequency dependence of the viscoelastic parameters observed on different cell types using various techniques (Fabry et al., 2001; Alcaraz et al., 2003) cannot be explained by these simple models.

A more complex theoretical model based on the structural organization and composition of cells is the *tensegrity* hypothesis. The tensegrity model takes its name from

architecture principles and states that cells are structures whose stability is maintained by tensile elements (cables) that cannot support compression, and compressive elements (struts) which balance the tension in the cables. The tension on these cables is balanced by internal compression-supporting elements and/or by external attachments. In living cells, actin filaments and intermediate filaments are viewed as the tensile elements, and microtubules, stress fibers and cell-cell and cell-ECM attachments are the responsible elements to balance tensional fores. Thus, cells and ECM work together to equilibrate the system. Some studies have used the cellular tensegrity model to describe a number of cellular features, such as prestress-induced stiffening or strain hardening (Wendling et al., 1999; Stamenovic et al., 2002; Coughlin and Stamenovic, 2003; Stamenovic, 2005; Wang et al., 2001). One of the main limitation of the tensegrity hypothesis is the fact that tensegrity is a static model and it may difficultly explain cellular active processes such as actin polymerization or activation of the contractile apparatus. However, it brings a *realistic* idea of the structure and function of each CSK element in living cells, and predicts interesting experimentally observed behaviors.

The third model addressed here interprets cellular dynamical behavior in terms of the *soft glassy rheology*, which was developed to explain foams, emulsions, or slurries (Sollich et al., 1997; Sollich, 1998). As mentioned before, cells probed using oscillatory measurements at a wide range of frequencies reveal an elastic and a frictional moduli that increase with frequency following a weak power-law (Maksym et al., 2000; Fabry et al., 2001, 2003; de Morales et al., 2004; Smith et al., 2005; Trepat et al., 2005). This behavior implies a continuous spectrum of relaxation times, which means that there is no resonant or characteristic viscoelastic time constant for cells. These results are supposed to be a reflect of a higher order structural organization rather than particular molecular properties (Sollich, 1998). Moreover, structural organization is thought to be in a metastable, out from the equilibrium, and disordered state. The complex shear modulus for such a material has been described by the structural damping model

$$G^*(\omega) = G_0 \left(\frac{\omega}{\Omega_0}\right)^{x-1} (1 + i\eta)\Gamma(2 - x)\cos\left(\frac{\pi(x-1)}{2}\right) \tag{1.6}$$

where G_0 and Ω_0 are scaling factors for stiffness and frequency, respectively, ω is radian frequency, (x–1) is the power law exponent, $\eta = \tan[\pi(x-1)/2]$ is the hysteresivity, $\Gamma()$ is the gamma function and $i = \sqrt{-1}$. The implications of the above equation are that, apart from scale factors that depend on the cell type, the state of the cells is described by the sole parameter x. Depending on the value of x, cells have solid-like (x=1) or liquid-like (x=2) behavior, which is mainly regulated by the activity or intracellular agitation

of the cytoskeletal molecules (Fabry et al., 2001, 2003). This parameter has been interpreted as an *effective noise temperature*, which might be modulated by the cells to vary their viscoelastic state. By the moment, the soft glassy model of cellular mechanics is a phenomenological model and, as such, it does not explain the ultimate responsible of the observed behavior.

1.3.2 Cell adhesion

In 1978, Bell exposed the first quantitative theory about cellular adhesion by means of specific non-covalent bonds and suggested that the dissociation of adhesive receptor-ligand bonds, which mediates cell adhesion, could be influenced by external applied force (Bell, 1978). The importance in Bell's theory was to hypothesize the significant role of mechanical force in biochemistry. It was not until AFM and other nanotools appeared that Bell's theory was directly tested by measuring rupture forces of individual isolated molecular complexes and, afterwards, directly of adhesion molecules on living cells (Moy et al., 1994a; Florin et al., 1994; Lehenkari and Horton, 1999). Evans and Ritchie extension of Bell's model (Evans and Ritchie, 1997) is described in this section since it is the most accepted and experimentally verified theory for single molecular bonds, which are though to regulate cellular adhesion.

Dynamic force spectroscopy

An isolated weak non-covalent individual bond exists far from equilibrium and only has non-zero strength on time scales shorter than the time needed for spontaneous dissociation $t_0 = 1/k_0$, where k_0 is the dissociation rate. If a force is applied faster than t_{off}, a bond resists detachment with a force determined by the intermolecular potential $E(x)$. Energy barriers depend on applied force to the bond (Fig. 1.6). The higher the applied force, the lower the barrier, and the shorter the lifetime, leading to an increase in the dissociation rate constant

$$k(f) = k_0 \exp\left(\frac{f\gamma}{k_B T}\right) \tag{1.7}$$

where f is the pulling force, γ is the width of the barrier projected along the direction of the pulling force, T is absolute temperature, and k_B is Boltzmann's constant. When pulling the bond with an increasing force ramp, the activation barrier height diminishes in time, and the probability density function for the dissociation of the bond at a force f is given by

$$P(f) = k_0 \exp\left(\frac{f\gamma}{k_B T}\right) \exp\left\{\frac{k_0 k_B T}{\gamma r_f}\left[1 - \exp\left(\frac{f\gamma}{k_B T}\right)\right]\right\} \tag{1.8}$$

where $r_f = df/dt$ is the loading rate, *i.e.* the rate at which force is applied (force/time). The maximum probability is given by maximizing Eq. 1.8, *i.e* $\partial P(f)/\partial f = 0$, which results in the most probable force

$$f^* = \frac{k_B T}{\gamma} \ln\left(\frac{\gamma}{k_0 k_B T}\right) \frac{k_B T}{\gamma} \ln\left(r_f\right) \tag{1.9}$$

To characterize the energy barriers the most probable force is calculated from the the mode of the rupture force histograms for a wide range of loading rates. This method is usually referred to as dynamic force spectroscopy (DFS) (Evans and Ritchie, 1997) and has been applied to explore the energy landscapes of different isolated interacting molecular complexes, such as biotin/(strept)avidin (Merkel et al., 1999), unfolding of FNIII domains in the extracellular matrix protein tenascin (Oberhauser et al., 1998), homotypic cadherins (Baumgartner et al., 2000a), and complexes within living cells, such as leukocyte function-associated antigen-1/intercellular adhesion molecule-1 (Zhang et al., 2002b), or integrin alpha(4)beta(1)/vascular cell adhesion molecule-1 (Zhang et al., 2004b). Usually, force versus $\ln(r_f)$ diagrams reflect one or more linear regimes, which stand for one or more activation barriers of the bond potential and range from few tens to one or two hundred pN. The outer and the inner barriers are described by the regimes at low and high loading rates, respectively. An important feature of single cellular adhesion molecules is their capability to increase the binding affinity or adhesion strength with which they bind. The in vivo modulation of the affinity of cells receptors occur by intracellular signaling and involves molecular conformational changes of them (van Kooyk and Figdor, 2000). It has been shown in living T-cells that integrins can be activated in vitro by means of Mg^{2+}, increasing the affinity or strength of formed bonds, but not by common cellular activators such as PMA (Wojcikiewicz et al., 2003). The modulation of the adhesion strength at the cellular level is also modulated by clustering and cooperativity of receptors. This feature is briefly described in the next subsection.

Multiple adhesion

According to Bell's theory, cellular adhesion is mediated by a number of specific bonds that bind cells between each other and to their extracellular matrix (Bell, 1978). Apart from the observed increase in individual binding affinity of molecular complexes, cells serve of another mechanism which enhances, even more, their binding capacity. This mechanism has been called *avidity*. Even if avidity is a term commonly used when re-

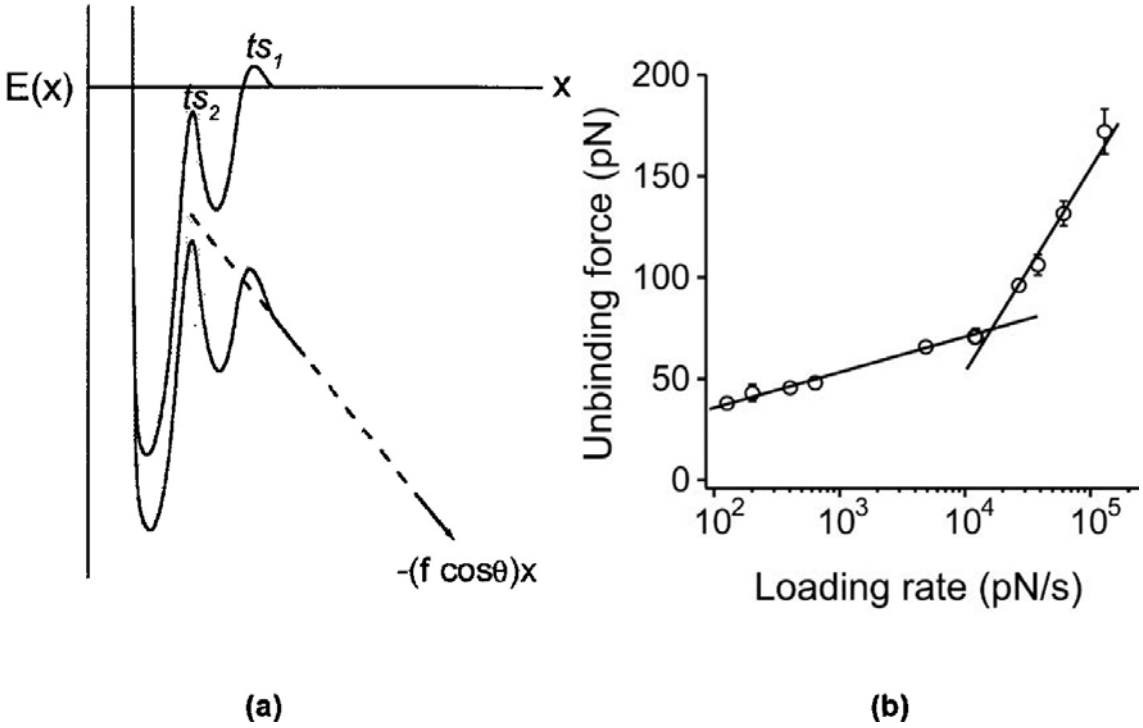

Figure 1.6: a) Conceptual energy landscape for a hypothetical bond with two activation barriers, transition stats (*ts*). A pulling force f oriented at an angle θ to the molecular coordinate x adds a mechanical potential $-(f\cos\theta)x$, that tilts the landscape lowering the barriers. b) Experimental force versus loading rate data (circles) for the cellular adhesion complex $\alpha_4\beta_1$/vascular cell adhesion molecule-1 complex in 2 mM Mg^{2+}. Diagram reflects two regimes which describe two transition states. Solid lines are linear fits to Eq. 1.9 for each regime. The resulting fitted values give an estimation of the Bell parameters for the potential. (Images adapted from (Evans, 2001) and (Zhang et al., 2004b), respectively.)

ferring to cellular adhesion, its meaning is still poorly defined. Avidity involves a dynamic reorganization of cell-adhesion receptors into clusters that can be attached to the cytoskeleton. Well known structures which are thought to enhance cell adhesion are focal adhesions. As mentioned in section 1.1.3, focal adhesion complexes are clusters of integrins and other related proteins linked to the actin CSK. Clustering of integrins and related molecules, such as vinculin, may induce a local mechanical stiffening of the functional adhesion units or adhesiosomes (*e.g.* adherens junctions, focal adhesions). This increase in adhesiosome stiffness may induce an increase in the loading rates involved in cellular movements, leading to an increase in the rupture force necessary to detach the adhesion units, and a consequent augment of the binding strength. Another example of modulation of the adhesion capacity by cells is the case of leukocytes. As reviewed by van Kooyk and Figdor, leukocytes under activated conditions (PMA treatment) modulate their adhesive

avidity by releasing integrin receptors from the CSK (van Kooyk and Figdor, 2000). Doing so, integrins can diffuse freely throughout the cell membrane, redistribute, and finally cluster. This mechanism has been recently found to be enhanced by the induced PMA decrease in cellular stiffness which is translated into a higher deformability, and results in a higher area of contact, increasing the number of binding sites (Wojcikiewicz et al., 2003). Adhesion molecules reorganization depends strongly on the cell type, function, activation process, and viscoelastic properties. Reorganization and redistribution of adhesion sites is thought to be the major determinant of the modulation of cells adhesive capacity, although viscoelastic properties are starting to be taken into account (van Kooyk and Figdor, 2000; Wojcikiewicz et al., 2003).

1.3.3 The alveolar-capillary barrier and mechanics of alveolar epithelial cells

The pulmonary system is responsible of the oxygen supply necessary for the normal function of cells that form the human body. Lungs are mechanically dynamic structures continuously subjected to deformation and cyclic forces due to spontaneous breathing or mechanical ventilation. Mechanical properties of cells have been shown to play a key role in important biological functions. The structure of the lungs where gas exchange takes place is the alveolar-capillary (a-c) barrier. This is formed by a monolayer of capillary endothelial cells laying on a basement membrane formed mainly by ECM fibers which, in turn, serves as a basement for the growth of a monolayer made of epithelial cells (Fig. 1.7). The alveolar-capillary structure form a semipermeable barrier which enables gas exchange between the blood and the alveolar airspace, while preventing from flowing of liquid, macromolecules, and migratory cells (Fig. 1.7 left). An important feature of lung injury is damage of the a-c barrier, which leads to alveolar flooding and infiltration of polymorphonuclear neutrophils and macromolecules to the alveolar airspace (Fig. 1.7 right). Alveolar flooding has been associated with the formation of paracellular gaps in both endothelial and epithelial monolayers. Acute lung injury has been associated with inflammation and mechanical ventilation (Martin, 2002). The maintenance of the a-c barrier under inflammatory conditions has been suggested to lay on a dynamic balance of the forces at which endothelial and epithelial cells are subjected (Dudek and Garcia, 2001; Kawkitinarong et al., 2004; Trepat et al., 2005). Knowledge of the mechanical properties of living pulmonary cells under basal, inflammatory, and stretched conditions is important for the better understanding of the maintenance of the integrity of the a-c barrier.

The working hypothesis is that the structural integrity of the a-c barrier is maintained

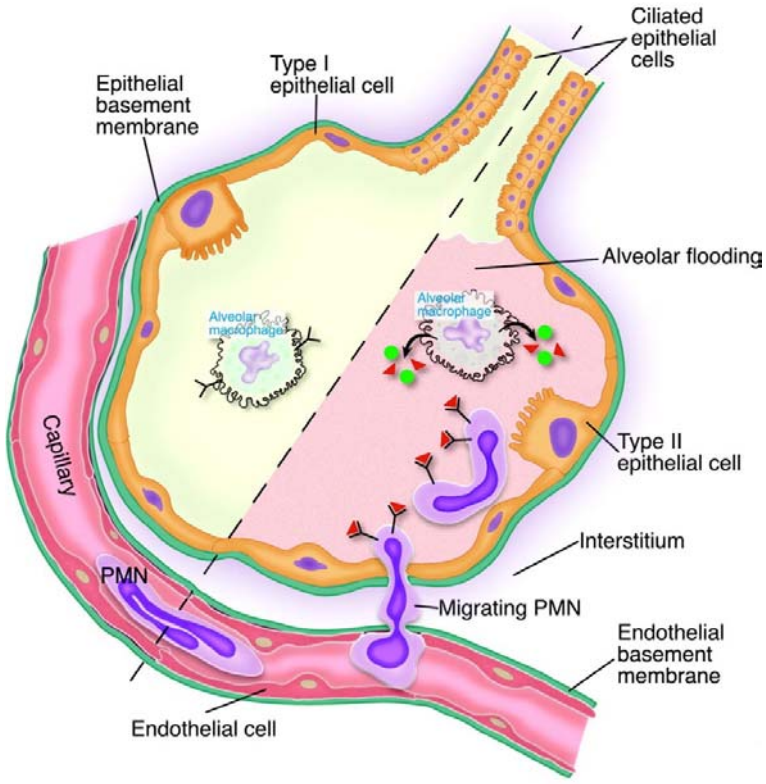

Figure 1.7: Normal (left) and injured (right) states of the alveolar-capillary interface. Normal alveolar function enables gas exchange while preventing from liquid flow and cellular migration. Under injured or inflammatory conditions the alveolar-capillary barrier may disrupt forming paracellular gaps. Vascular liquid, polymorphonuclear neutrophils, and macromolecules may infiltrate into the alveolar airspace causing alveolar flooding. (Adapted from Feistritzer and Riewald 2005)

by the balance between inward or centripetal forces and outward or centrifugal adhesive forces applied at cell-cell and cell-ECM adhesion sites. Inward forces are caused by passive viscoelastic recoil during cell stretching owing to breathing or mechanical ventilation, and by active cellular contraction due to activation of the actomyosin machinery. In normal conditions, this inward forces might be counterbalanced by the outward adhesive forces that hold cells between each other and to the ECM. On the one hand, it has been shown that human pulmonary artery endothelial cells treated with the proinflammatory mediator thrombin increase the phosphorylation of the myosin light chain kinase, which is related with the activation of the contractile cell apparatus (Dudek and Garcia, 2001). In addition, measurement of the electrical resistance across endothelial monolayers reflected a significant augment in response to thrombin, suggesting an increment in the endothelial permeability. This increased permeability has been also associated with formation of paracellular gaps (Kawkitinarong et al., 2004). In contrast, recent studies on human um-

bilical vein endothelial cells have shown that thrombin at low concentrations (~40 pM) may have protective effects of the endothelial barrier (Feistritzer and Riewald, 2005). On the other hand, similar measurements on human alveolar epithelial cells showed a decrease in electrical resistance after addition of thrombin, suggesting now a decrease in epithelial barrier permeability (Kawkitinarong et al., 2004). The authors showed also an increase in the activation of the actomyosin machinery, reflecting cellular contraction. Immunostaining of cell-cell adhesion sites reflected accumulation of ZO-1/occludin complexes, related with tight junctions, which are known to be important in the maintenance of monolayer permeability. Kawkitinarong and co-workers interpreted these results as evidences of enhancement of epithelial barrier integrity, suggesting different and opposite roles of thrombin on epithelial and endothelial cells. Nevertheless, the cited works only show indirect measurements of the forces involved in the structural integrity of the a-c barrier. Recent mechanical measurements carried out on human alveolar epithelial cells using magnetic tweezers have shown that thrombin induced a rapid and sustained increase of cellular stiffness, which is in accordance with different measurements on various cell types that relates contractibility activation with cell stiffening (Trepat et al., 2005). An increased stiffness may induce an augment in the viscoelastic recoil due to breathing or mechanical ventilation. Moreover, it has been shown that alveolar epithelial cells subjected to stretch were stiffer than non-stretched cells (Trepat et al., 2004). In addition, recent measurements on our laboratory suggest that thrombin induces an increase in the contractile force as measured using traction microscopy, which is a direct measurement of the inward forces exerted by cells to the substratum (Gavara, 2005). Taken together, these results suggest that thrombin induces an increase in the inward forces of alveolar epithelial cells. However, as far as we know, there is no direct measurements of the adhesive (outward) forces involved in cell-cell and cell-ECM adhesion sites of the alveolar epithelium under inflammatory conditions. According to the working hypothesis adhesive forces may counterbalance the increase in the inward forces to maintain the a-c barrier integrity. If adhesive forces cannot withstand the increased inward tension, the balance of forces may break, leading to disruption of the alveolar epithelium. One of the most used tools to probe adhesion forces at both molecular and cellular level is atomic force microscopy (Benoit and Gaub, 2002). Thus, further knowledge of the maintenance of the integrity of the a-c barrier may be addressed by measuring the adhesion strength using such technique on living pulmonary cells.

Bibliography

E. A-Hassan, W. Heinz, M. D. Antonik, N. P. D'Costa, S. Nageswaran, C. A. Schoenenberger, and J. H. Hoh. Relative microelastic mapping of living cells by atomic force microscopy. *Biophys.J.*, 74:1564–1578, 1998.

B. Alberts, D. Bray, J. Lewis, M. Raff, K. Roberts, and J. D. Watson. *Molecular Biology of the Cell*. Garland Publishing, New York, 1994.

T. R. Albrecht, P. Grutter, D. Horne, and D. Rugar. Frequency modulation detection using high-q cantilevers for enhanced force microscope sensitivity. *J.Appl.Phys.*, 69 (2):668–673, 1991.

J. Alcaraz, L. Buscemi, M. Puig de Morales, J. Colchero, A. Baro, and D. Navajas. Correction of microrheological measurements of soft samples with atomic force microscopy for the hydrodynamic drag on the cantilever. *Langmuir*, 18(3):716–721, 2002.

J. Alcaraz, L. Buscemi, M. Grabulosa, X. Trepat, B. Fabry, R. Farre, and D. Navajas. Microrheology of human lung epithelial cells measured by atomic force microscopy. *Biophys.J.*, 84:2071–2079, 2003.

N. Q. Balaban, U. S. Schwarz, D. Riveline, P. Goichberg, G. Tzur, I. Sabanay, D. Mahalu, S. Safran, A. Bershadsky, L. Addadi, and B. Geiger. Force and focal adhesion assembly: a close relationship studied using elastic micropatterned substrates. *Nature Cell Biology*, 3(5):466–472, 2001.

W. Baumgartner, P. Hinterdorfer, W. Ness, A. Raab, D. Vestweber, H. Schindler, and D. Drenckhahn. Cadherin interaction probed by atomic force microscopy. *Proc.Natl.Acad.Sci.U.S.A.*, 97(8):4005–4010, 2000a.

W. Baumgartner, P. Hinterdorfer, and H. Schindler. Data analysis of interaction forces measured with the atomic force microscope. *Ultramicroscopy*, 82(1-4):85–95, 2000b.

A. R. Bausch, U. Hellerer, M. Essler, M. Aepfelbacher, and E. Sackmann. Rapid stiffening of integrin receptor-actin linkages in endothelial cells stimulated with thrombin: a magnetic bead microrheology study. *Biophys.J.*, 80(6):2649–2657, 2001.

G. I. Bell. Models for specific adhesion of cells to cells. *Science*, 200(4342):618–627, 1978.

M. Benoit and H. E. Gaub. Measuring cell adhesion forces with the atomic force microscope at the molecular level. *Cells Tissues Organs*, 172(3):174–189, 2002.

M. Benoit, D. Gabriel, G. Gerisch, and H. E. Gaub. Discrete interactions in cell adhesion measured by single-molecule force spectroscopy. *Nature Cell Biology*, 2(6):313–317, 2000.

A. D. Bershadsky, N. Q. Balaban, and B. Geiger. Adhesion-dependent cell mechanosensitivity. *Annu.Rev.Cell Dev.Biol.*, 19:677–695, 2003.

K. Bhadriraju and L. K. Hansen. Extracellular matrix- and cytoskeleton-dependent changes in cell shape and stiffness. *Exp.Cell Res.*, 278(1):92–100, 2002.

G. Bilodeau. Regular pyramid punch problem. *J.Appl.Mech.-Trans.ASME*, 59:519–523, 1992.

G. Binnig, C. F. Quate, and Ch Gerber. Atomic force microscope. *Phys.Rev.Lett.*, 56(9): 930–933, 1986.

D. Bray. *Cell Movements. From Molecules to Motility*. Garland Publishing, New York, 2001.

B. J. Briscoe, K. S. Sebastian, and M. J. Adams. The effect of indenter geometry on the elastic response to indentation. *J.Phys.D: Appl.Phys.*, 27:1156–1162, 1994.

N. A. Burnham and R. J. Colton. Measuring the nanomechanical properties and surface forces of materials using an atomic force microscope. *J.Vac.Sci.Technol.A*, 7(4):2906–2913, 1989.

N. A. Burnham, O. P. Behrend, F. Oulevey, G. Gremaud, P. J. Gallo, D. Gourdon, E. Dupas, A. J. Kulik, H. M. Pollock, and G. A. D. Briggs. How does a tip tap? *Nanotechnology*, 8(2):67–75, 1997.

P. Bursac, G. Lenormand, B. Fabry, M. Oliver, D. A. Weitz, V. Viasnoff, J. P. Butler, and J. J. Fredberg. Cytoskeletal remodelling and slow dynamics in the living cell. *Nature Materials*, 4(7):557–561, 2005.

L. Buscemi. Estudi mitjançant microscòpia de força atòmica de la mecànica de cèl.lules epitelials alveolars en resposta a trombina. 2004.

C. Bustamante, Y. R. Chemla, N. R. Forde, and D. Izhaky. Mechanical processes in biochemistry. *Annu.Rev.Biochem.*, 73:705–748, 2004.

J. P. Butler, R. E. Brown, D. Stamenovic, J. P. Morris, and G. P. Topulos. Effect of surface tension on alveolar surface area. *J.Appl.Physiol*, 93(3):1015–1022, 2002a.

James P. Butler, Iva M. Tolic-Norrelykke, Ben Fabry, and Jeffrey J. Fredberg. Traction fields, moments, and strain energy that cells exert on their surroundings. *Am J Physiol Cell Physiol*, 282(3):C595–C605, 2002b.

H. J. Butt, E. K. Wolff, S. A. Gould, Northern B. Dixon, C. M. Peterson, and Hansma. Imaging cells with the atomic force microscope. *J.Struct.Biol.*, 105(1-3):54–61, 1990.

Nathalie Caille, Olivier Thoumine, Yanik Tardy, and Jean J. Meister. Contribution of the nucleus to the mechanical properties of endothelial cells. *J.Biomech.*, 35(2):177–187, 2002.

B. Cappella and G. Dietler. Force-distance curves by atomic force microscopy. *Surface Science Reports*, 34(1-3):1–+, 1999.

G. T. Charras and M. A. Horton. Single cell mechanotransduction and its modulation analyzed by atomic force microscope indentation. *Biophys.J.*, 82(6):2970–2981, 2002a.

G. T. Charras and M. A. Horton. Determination of cellular strains by combined atomic force microscopy and finite element modeling. *Biophys.J.*, 83(2):858–879, 2002b.

D. Choquet, D. P. Felsenfeld, and M. P. Sheetz. Extracellular matrix rigidity causes strengthening of integrin-cytoskeleton linkages. *Cell*, 88(1):39–48, 1997.

K. D. Costa and F. C. P. Yin. Analysis of indentation: implications for measuring mechanical properties with atomic force microscopy. *J.Biomech.Eng.*, 121:462–471, 1999.

M. F. Coughlin and D. Stamenovic. A prestressed cable network model of the adherent cell cytoskeleton. *Biophys.J.*, 84(2 Pt 1):1328–1336, 2003.

F. H. C. Crick and A. F. W. Hughes. The physical properties of cytoplasm - a study by means of the magnetic particle method .1. experimental. *Exp.Cell Res.*, 1(1):37–80, 1950.

D. R. Critchley. Focal adhesions - the cytoskeletal connection. *Curr.Opin.Cell Biol.*, 12 (1):133–139, 2000.

Kris N. Dahl, Adam J. Engler, J. D. Pajerowski, and Dennis E. Discher. Power-law rheology of isolated nuclei with deformation mapping of nuclear substructures. *Biophys.J.*, 89(4):2855–2864, 2005.

M. Puig de Morales, E. Millet, B. Fabry, D. Navajas, N. Wang, J. P. Butler, and J. J. Fredberg. Cytoskeletal mechanics in adherent human airway smooth muscle cells: probe specificity and scaling of protein-protein dynamics. *Am.J.Physiol.-Cell Physiol.*, 287(3):C643–C654, 2004.

P. J. de Pablo, I. A. T. Schaap, F. C. MacKintosh, and C. F. Schmidt. Deformation and collapse of microtubules on the nanometer scale. *Phys.Rev.Lett.*, 91(9), 2003.

M. Dembo, T. Oliver, A. Ishihara, and K. Jacobson. Imaging the traction stresses exerted by locomoting cells with the elastic substratum method. *Biophys.J.*, 70(4):2008–2022, 1996.

N. Desprat, A. Richert, J. Simeon, and A. Asnacios. Creep function of a single living cell. *Biophys.J.*, 88(3):2224–2233, 2005.

E. K. Dimitriadis, F. Horkay, J. Maresca, B. Kachar, and R. S. Chadwick. Determination of elastic moduli of thin layers of soft material using the atomic force microscope. *Biophys.J.*, 82:2798–2810, 2002.

J. Domke and M. Radmacher. Measuring the elastic properties of thin polymer films with the atomic force microscope. *Langmuir*, 14(12):3320–3325, 1998.

J. Domke, S. Dannohl, W. J. Parak, O. Muller, W. K. Aicher, and M. Radmacher. Substrate dependent differences in morphology and elasticity of living osteoblasts investigated by atomic force microscopy. *Colloids Surf.B Biointerfaces*, 19(4):367–379, 2000.

S. M. Dudek and J. G. Garcia. Cytoskeletal regulation of pulmonary vascular permeability. *J.Appl.Physiol*, 91(4):1487–1500, 2001.

J. A. Dvorak. The application of atomic force microscopy to the study of living vertebrate cells in culture. *Methods*, 29(1):86–96, 2003.

R. J. Ellis and A. P. Minton. Cell biology - join the crowd. *Nature*, 425(6953):27–28, 2003.

E. Evans. Probing the relation between force - lifetime - and chemistry in single molecular bonds. *Annu.Rev.Biophys.Biomol.Struct.*, 30:105–128, 2001.

E. Evans and K. Ritchie. Dynamic strength of molecular adhesion bonds. *Biophys.J.*, 72 (4):1541–1555, 1997.

E. Evans and A. Yeung. Apparent viscosity and cortical tension of blood granulocytes determined by micropipet aspiration. *Biophys.J.*, 56(1):151–160, 1989.

B. Fabry, G. N. Maksym, J. Butler, M. Glogauer, D. Navajas, and J. J. Fredberg. Scaling the microrheology of living cells. *Phys.Rev.Lett.*, 87:148102–148105, 2001.

B. Fabry, G. N. Maksym, J. P. Butler, M. Glogauer, D. Navajas, N. A. Taback, E. J. Millet, and J. J. Fredberg. Time scale and other invariants of integrative mechanical behavior in living cells. *Phys.Rev.E*, 68(4), 2003.

Clemens Feistritzer and Matthias Riewald. Endothelial barrier protection by activated protein c through par1-dependent sphingosine 1-phosphate receptor-1 crossactivation. *Blood*, 105(8):3178–3184, 2005.

Jeffrey T. Finer, Robert M. Simmons, and James A. Spudich. Single myosin molecule mechanics: piconewton forces and nanometre steps. *Nature*, 368(6467):113–119, 1994.

E. L. Florin, V. T. Moy, and H. E. Gaub. Adhesion forces between individual ligand-receptor pairs. *Science*, 264(5157):415–417, 1994.

E. L. Florin, M. Rief, H. Lehmann, M. Ludwig, C. Dornmair, V. T. Moy, and H. E. Gaub. Sensing specific molecular-interactions with the atomic-force microscope. *Biosens.Bioelectron.*, 10(9-10):895–901, 1995.

M. Fritz, M. Radmacher, and H. E. Gaub. Granula motion and membrane spreading during activation of human platelets imaged by atomic force microscopy. *Biophys.J.*, 66(5):1328–1334, 1994.

D. S. Fudge, K. H. Gardner, V. T. Forsyth, C. Riekel, and J. M. Gosline. The mechanical properties of hydrated intermediate filaments: Insights from hagfish slime threads. *Biophys.J.*, 85(3):2015–2027, 2003.

C. G. Galbraith, K. M. Yamada, and M. P. Sheetz. The relationship between force and focal complex development. *Journal of Cell Biology*, 159(4):695–705, 2002.

N. Gavara. Personal communication. 2005.

F. Gittes, B. Schnurr, P. D. Olmsted, F. C. MacKintosh, and C. F. Schmidt. Microscopic viscoelasticity: Shear moduli of soft materials determined from thermal fluctuations. *Phys.Rev.Lett.*, 79(17):3286–3289, 1997.

W. H. Goldmann and R. M. Ezzell. Viscoelasticity in wild-type and vinculin-deficient (5.51) mouse f9 embryonic carcinoma cells examined by atomic force microscopy and rheology. *Exp.Cell Res.*, 226(1):234–237, 1996.

W. H. Goldmann, R. Galneder, M. Ludwig, W. Xu, E. D. Adamson, N. Wang, and R. M. Ezzell. Differences in elasticity of vinculin-deficient f9 cells measured by magnetometry and atomic force microscopy. *Exp.Cell Res.*, 239(2):235–242, 1998.

W. Haberle, J. K. H. Horber, and G. Binnig. Force microscopy on living cells. *J.Vac.Sci.Technol.B*, 9(2):1210–1213, 1991.

S. W. Han, C. Nakamura, I. Obataya, N. Nakamura, and J. Miyake. A molecular delivery system by using afm and nanoneedle. *Biosens.Bioelectron.*, 20(10):2120–2125, 2005.

P. K. Hansma, J. P. Cleveland, M. Radmacher, D. A. Walters, P. E. Hillner, M. Bezanilla, M. Fritz, D. Vie, H. G. Hansma, C. B. Prater, J. Massie, L. Fukunaga, J. Gurley, and V. Elings. Tapping mode atomic force microscopy in liquids. *Appl.Phys.Lett.*, 64(13): 1738–1740, 1994a.

P. K. Hansma, B. Drake, D. Grigg, C. B. Prater, F. Yashar, G. Gurley, S. V. Eling, S. Feinstein, and R. Lal. A new, optical-lever based atomic-force microscope. *J.Appl.Phys.*, 76(2):796–799, 1994b.

A. Hategan, R. Law, S. Kahn, and D. E. Discher. Adhesively-tensed cell membranes: Lysis kinetics and atomic force microscopy probing. *Biophys.J.*, 85(4):2746–2759, 2003.

E. Henderson, P. G. Haydon, and D. S. Sakaguchi. Actin filament dynamics in living glial cells imaged by atomic force microscopy. *Science*, 257(5078):1944–1946, 1992.

H. Hertz. On the contact of elastic bodies. In *Hertz's Miscellaneous Papers*, Miscellaneous Papers, chapter 5, pages 146–162. Macmillan, London, 1881.

R. M. Hochmuth. Micropipette aspiration of living cells. *J.Biomech.*, 33(1):15–22, 2000.

J. H. Hoh and C. A. Schoenenberger. Surface morphology and mechanical properties of mdck monolayers by atomic force microscopy. *J.Cell Sci.*, 107(Pt 5):1105–1114, 1994.

M. A. Horton, G. T. Charras, G. Ballestrem, and P. P. Lehenkari. Integration of atomic force and confocal microscopy. *Single Molecules*, 1(2):135–137, 2000.

A. F. Horwitz. Integrins and health. *Sci.Am.*, 276(5):68–75, 1997.

J Howard. *Mechanics of Motor Proteins and the Cytoskeleton*. Sinauer Associates, Sunderland, MA, 2001.

Joe Howard and Anthony A. Hyman. Dynamics and mechanics of the microtubule plus end. *Nature*, 422(6933):753–758, 2003.

Hayden Huang, Roger D. Kamm, and Richard T. Lee. Cell mechanics and mechanotransduction: pathways, probes, and physiology. *Am.J.Physiol.-Cell Physiol.*, 287(1): C1–11, 2004.

K. Hyonchol, H. Arakawa, T. Osada, and A. Ikai. Quantification of fibronectin and cell surface interactions by afm. *Colloid Surf.B-Biointerfaces*, 25(1):33–43, 2002.

P. A. Janmey. Mechanical properties of cytoskeletal polymers. *Curr.Opin.Cell Biol.*, 3 (1):4–11, 1991.

P. A. Janmey and D. A. Weitz. Dealing with mechanics: mechanisms of force transduction in cells. *Trends Biochem.Sci.*, 29(7):364–370, 2004.

H. J. Janovjak, J. Struckmeier, and D. J. Muller. Hydrodynamic effects in fast afm single-molecule force measurements. *Eur Biophys J Biophy*, 34(1):91–96, 2005.

K. L. Johnson. *Contact Mechanics*. Cambridge University Press, Cambridge, 1985.

R. L. Juliano. Signal transduction by cell adhesion receptors and the cytoskeleton: Functions of integrins, cadherins, selectins, and immunoglobulin-superfamily members. *Annu.Rev.Pharmacol.Toxicol.*, 42(1):283–323, 2002.

K. Kawkitinarong, L. Linz-McGillem, K. G. Birukov, and J. G. Garcia. Differential regulation of human lung epithelial and endothelial barrier function by thrombin. *Am.J.Respir.Cell Mol.Biol.*, 31(5):517–527, 2004.

E. Knust and O. Bossinger. Composition and formation of intercellular junctions in epithelial cells. *Science*, 298(5600):1955–1959, 2002.

E. Kokkoli, S. E. Ochsenhirt, and M. Tirrell. Collective and single-molecule interactions of alpha(5)beta(1) integrins. *Langmuir*, 20(6):2397–2404, 2004.

V. M. Laurent, S. Henon, E. Planus, R. Fodil, M. Balland, D. Isabey, and F. Gallet. Assessment of mechanical properties of adherent living cells by bead micromanipulation: comparison of magnetic twisting cytometry vs optical tweezers. *J.Biomech.Eng*, 124 (4):408–421, 2002.

I. Lee and R. E. Marchant. Force measurements on platelet surfaces with high spatial resolution under physiological conditions. *Colloid Surf.B-Biointerfaces*, 19(4):357–365, 2000.

P. P. Lehenkari and M. A. Horton. Single integrin molecule adhesion forces in intact cells measured by atomic force microscopy. *Biochem.Biophys.Res.Commun.*, 259(3): 645–650, 1999.

P. P. Lehenkari, G. T. Charras, A. Nykanen, and M. A. Horton. Adapting atomic force microscopy for cell biology. *Ultramicroscopy*, 82(1-4):289–295, 2000.

F. Y. Li, S. D. Redick, H. P. Erickson, and V. T. Moy. Force measurements of the alpha(5)beta(1) integrin-fibronectin interaction. *Biophys.J.*, 84(2):1252–1262, 2003.

Y. Q. Li, N. J. Tao, J. Pan, A. A. Garcia, and S. M. Lindsay. Direct measurement of interaction forces between colloidal particles using the scanning force microscope. *Langmuir*, 9:637–641, 1993.

F. C. MacKintosh and C. F. Schmidt. Microrheology. *CUrrent Opinion in Colloid and Interface Science*, 4(4):300–307, 1999.

R. E. Mahaffy, C. K. Shih, F. C. MacKintosh, and J. Kas. Scanning probe-based frequency-dependent microrheology of polymer gels and biological cells. *Phys.Rev.Lett.*, 85:880–883, 2000.

R. E. Mahaffy, S. Park, E. Gerde, J. Kas, and C. K. Shih. Quantitative analysis of the viscoelastic properties of thin regions of fibroblasts using atomic force microscopy. *Biophys.J.*, 86(3):1777–1793, 2004.

G. N. Maksym, B. Fabry, J. P. Butler, D. Navajas, D. J. Tschumperlin, J. D. Laporte, and J. J. Fredberg. Mechanical properties of cultured human airway smooth muscle cells from 0.05 to 0.4 hz. *J.Appl.Physiol*, 89(4):1619–1632, 2000.

A. J. Maniotis, C. S. Chen, and D. E. Ingber. Demonstration of mechanical connections between integrins cytoskeletal filaments, and nucleoplasm that stabilize nuclear structure. *Proc.Natl.Acad.Sci.U.S.A.*, 94(3):849–854, 1997.

Thomas R. Martin. Neutrophils and lung injury: getting it right. *J.Clin.Invest.*, 110(11): 1603–1605, 2002.

Anshu B. Mathur, Amy M. Collinsworth, William M. Reichert, William E. Kraus, and George A. Truskey. Endothelial, cardiac muscle and skeletal muscle exhibit different viscous and elastic properties as determined by atomic force microscopy. *J.Biomech.*, 34(12):1545–1553, 2001.

O. Medalia, I. Weber, A. S. Frangakis, D. Nicastro, G. Gerisch, and W. Baumeister. Macromolecular architecture in eukaryotic cells visualized by cryoelectron tomography. *Science*, 298(5596):1209–1213, 2002.

R. Merkel, P. Nassoy, A. Leung, K. Ritchie, and E. Evans. Energy landscapes of receptor-ligand bonds explored with dynamic force spectroscopy. *Nature*, 397(6714):50–53, 1999.

L. L. Mitic and J. M. Anderson. Molecular architecture of tight junctions. *Annu.Rev.Physiol.*, 60:121–142, 1998.

A. Mogilner and G. Oster. Force generation by actin polymerization ii: The elastic ratchet and tethered filaments. *Biophys.J.*, 84(3):1591–1605, 2003.

V. T. Moy, E. L. Florin, and H. E. Gaub. Intermolecular forces and energies between ligands and receptors. *Science*, 266(5183):257–259, 1994a.

V. T. Moy, E. L. Florin, and H. E. Gaub. Adhesive forces between ligand and receptor measured by afm. *Biophys.J.*, 66(2):A340, 1994b.

M. Nagayama, H. Haga, M. Takahashi, T. Saitoh, and K. Kawabata. Contribution of cellular contractility to spatial and temporal variations in cellular stiffness. *Exp.Cell Res.*, 300(2):396–405, 2004.

K. C. Neuman and S. M. Block. Optical trapping. *Rev.Sci.Instr.*, 75(9):2787–2809, 2004.

F. Obataya, C. Nakamura, S. W. Han, N. Nakamura, and J. Miyake. Mechanical sensing of the penetration of various nanoneedles into a living cell using atomic force microscopy. *Biosens.Bioelectron.*, 20(8):1652–1655, 2005a.

I. Obataya, C. Nakamura, S. Han, N. Nakamura, and J. Miyake. Nanoscale operation of a living cell using an atomic force microscope with a nanoneedle. *Nano Letters*, 5(1): 27–30, 2005b.

A. F. Oberhauser, P. E. Marszalek, H. P. Erickson, and J. M. Fernandez. The molecular elasticity of the extracellular matrix protein tenascin. *Nature*, 393(6681):181–185, 1998.

G. M. Pharr, W. C. Oliver, and F. R. Brotzen. On the generality of the relationship among contact stiffness, contact area, and elastic modulus during indentation. *J.Mater.Res.*, 7 (3):613–617, 1992.

J. Pourati, A. Maniotis, D. Spiegel, J. L. Schaffer, J. P. Butler, J. J. Fredberg, D. E. Ingber, D. Stamenovic, and N. Wang. Is cytoskeletal tension a major determinant of cell deformability in adherent endothelial cells? *Am.J.Physiol*, 274(5 Pt 1):C1283–C1289, 1998.

C. A. J. Putman, K. O. Vanderwerf, B. G. Degrooth, N. F. Vanhulst, F. B. Segerink, and J. Greve. Atomic force microscope with integrated optical microscope for biological applications. *Rev.Sci.Instr.*, 63(3):1914–1917, 1992.

C. A. J. Putman, K. O. Vanderwerf, B. G. Degrooth, N. F. Vanhulst, and J. Greve. Viscoelasticity of living cells allows high-resolution imaging by tapping mode atomic-force microscopy. *Biophys.J.*, 67(4):1749–1753, 1994.

M. Rief, M. Gautel, F. Oesterhelt, J. M. Fernandez, and H. E. Gaub. Reversible unfolding of individual titin immunoglobulin domains by afm. *Science*, 276(5315):1109–1112, 1997.

C. Rotsch and M. Radmacher. Drug-induced changes of cytoskeletal structure and mechanics in fibroblasts: an atomic force microscopy study. *Biophys.J.*, 78:520–535, 2000.

C. Rotsch, F. Braet, E. Wisse, and M. Radmacher. Afm imaging and elasticity measurements on living rat liver macrophages. *Cell Biol.Int.*, 21(11):685–696, 1997.

P. Roy, Z. Rajfur, P. Pomorski, and K. Jacobson. Microscope-based techniques to study cell adhesion and migration. *Nature Cell Biology*, 4(4):E91–E96, 2002.

S. W. Schneider, P. Pagel, C. Rotsch, T. Danker, H. Oberleithner, M. Radmacher, and A. Schwab. Volume dynamics in migrating epithelial cells measured with atomic force microscopy. *Pflugers Archiv-European Journal of Physiology*, 439(3):297–303, 2000.

B. Schnurr, F. Gittes, P. D. Olmsted, F. C. MacKintosh, and C. F. Schmidt. Microrheology in actin gels: Experiment and theory. *Biophys.J.*, 72(2):TU285, 1997.

B. A. Smith, B. Tolloczko, J. G. Martin, and P. Grutter. Probing the viscoelastic behavior of cultured airway smooth muscle cells with atomic force microscopy: stiffening induced by contractile agonist. *Biophys.J.*, 88(4):2994–3007, 2005.

I. N. Sneddon. The relaxation between load and penetration in the axisymmetric boussinesq problem for a punch of arbitrary profile. *Int.J.Engng.Sci.*, 3:47–57, 1965.

P. Sollich. Rheological constitutive equation for a model of soft glassy materials. *Phys.Rev.E*, 58(1):738–759, 1998.

P. Sollich, F. Lequeux, P. H,braud, and M. Cauberghs. Rheology of soft glassy materials. *Phys.Rev.Lett.*, 78:2020–2023, 1997.

D. Stamenovic. Microtubules may harden or soften cells, depending of the extent of cell distension. *J.Biomech.*, 38(8):1728–1732, 2005.

D. Stamenovic and D. E. Ingber. Models of cytoskeletal mechanics of adherent cells. *Biomech Model.Mechanobiol.*, 1(1):95–108, 2002.

D. Stamenovic, S. M. Mijailovich, I. M. Tolic-Norrelykke, J. Chen, and N. Wang. Cell prestress. ii. contribution of microtubules. *Am.J.Physiol Cell Physiol*, 282(3):C617–C624, 2002.

M. Stolz, R. Raiteri, A. U. Daniels, M. R. VanLandingham, W. Baschong, and U. Aebi. Dynamic elastic modulus of porcine articular cartilage determined at two different levels of tissue organization by indentation-type atomic force microscopy. *Biophys.J.*, 86 (5):3269–3283, 2004.

C. Storm, J. J. Pastore, F. C. MacKintosh, T. C. Lubensky, and P. A. Janmey. Nonlinear elasticity in biological gels. *Nature*, 435(7039):191–194, 2005.

J. L. Tan, J. Tien, D. M. Pirone, D. S. Gray, K. Bhadriraju, and C. S. Chen. Cells lying on a bed of microneedles: An approach to isolate mechanical force. *Proc.Natl.Acad.Sci.U.S.A.*, 100(4):1484–1489, 2003.

N. J. Tao, S. M. Lindsay, and S. Lees. Measuring the microelastic properties of biological-material. *Biophys.J.*, 63(4):1165–1169, 1992.

D. F. J. Tees, R. E. Waugh, and D. A. Hammer. A microcantilever device to assess the effect of force on the lifetime of selectin-carbohydrate bonds. *Biophys.J.*, 80(2):668–682, 2001.

O. Thoumine and A. Ott. Time scale dependent viscoelastic and contractile regimes in fibroblasts probed by microplate manipulation. *J.Cell Sci.*, 110:2109–2116, 1997.

O. Thoumine, A. Ott, and D. Louvard. Critical centrifugal forces induce adhesion rupture or structural reorganization in cultured cells. *Cell Motil.Cytoskeleton*, 33(4):276–287, 1996.

O. Thoumine, A. Ott, O. Cardoso, and J. J. Meister. Microplates: a new tool for manipulation and mechanical perturbation of individual cells. *J.Biochem.Biophys.Methods*, 39 (1-2):47–62, 1999.

A. Touhami, B. Nysten, and Y. F. Dufrene. Nanoscale mapping of the elasticity of microbial cells by atomic force microscopy. *Langmuir*, 19(11):4539–4543, 2003.

A. Trache, J. P. Trzeciakowski, L. A. Gardiner, Z. Sun, M. Muthuchamy, M. Guo, S. Y. Yuan, and G. A. Meininger. Histamine effects on endothelial cell fibronectin interaction studied by atomic force microscopy. *Biophys.J.*, 2005.

X. Trepat, M. Grabulosa, F. Puig, G. N. Maksym, D. Navajas, and R. Farre. Viscoelasticity of human alveolar epithelial cells subjected to stretch. *Am.J.Physiol.-Lung Cell.Mol.Physiol.*, 2004.

X. Trepat, M. Grabulosa, L. Buscemi, F. Rico, R. Farre, and D. Navajas. Thrombin and histamine induce stiffening of alveolar epithelial cells. *J.Appl.Physiol*, 98(4):1567–1574, 2005.

M. T. Valentine, Z. E. Perlman, T. J. Mitchison, and D. A. Weitz. Mechanical properties of xenopus egg cytoplasmic extracts. *Biophys.J.*, 88(1):680–689, 2005.

Y. van Kooyk and C. G. Figdor. Avidity regulation of integrins: the driving force in leukocyte adhesion. *Curr.Opin.Cell Biol.*, 12(5):542–547, 2000.

Peter Wagner. Immobilization strategies for biological scanning probe microscopy. *FEBS Lett.*, 430(1-2):112–115, 1998.

N. Wang and D. Stamenovic. Mechanics of vimentin intermediate filaments. *J.Muscle Res.Cell Motil.*, 23(5-6):535–540, 2002.

N. Wang, J. P. Butler, and D. E. Ingber. Mechanotransduction across the cell surface and through the cytoskeleton. *Science*, 260(5111):1124–1127, 1993.

N. Wang, K. Naruse, D. Stamenovic, J. J. Fredberg, S. M. Mijailovich, I. M. Tolic-Norrelykke, T. Polte, R. Mannix, and D. E. Ingber. Mechanical behavior in living cells consistent with the tensegrity model. *Proc.Natl.Acad.Sci.U.S.A*, 98(14):7765–7770, 2001.

N. Wang, I. M. Tolic-Norrelykke, J. Chen, S. M. Mijailovich, J. P. Butler, J. J. Fredberg, and D. Stamenovic. Cell prestress. i. stiffness and prestress are closely associated in adherent contractile cells. *Am.J.Physiol Cell Physiol*, 282(3):C606–C616, 2002.

S. Wendling, C. Oddou, and D. Isabey. Stiffening response of a cellular tensegrity model. *J.Theor.Biol.*, 196(3):309–325, 1999.

E. P. Wojcikiewicz, X. Zhang, A. Chen, and V. T. Moy. Contributions of molecular binding events and cellular compliance to the modulation of leukocyte adhesion. *J.Cell Sci.*, 116(Pt 12):2531–2539, 2003.

H. W. Wu, T. Kuhn, and V. T. Moy. Mechanical properties of l929 cells measured by atomic force microscopy: Effects of anticytoskeletal drugs and membrane crosslinking. *Scanning*, 20(5):389–397, 1998.

Kazushi Yamanaka, Hisato Ogiso, and Oleg Kolosov. Ultrasonic force microscopy for nanometer resolution subsurface imaging. *Appl.Phys.Lett.*, 64(2):178–180, 1994.

H. X. You, J. M. Lau, S. Zhang, and L. Yu. Atomic force microscopy imaging of living cells: a preliminary study of the disruptive effect of the cantilever tip on cell morphology. *Ultramicroscopy*, 82(1-4):297–305, 2000.

X. Zhang, E. Wojcikiewicz, and V. T. Moy. Force spectroscopy of the leukocyte function-associated antigen-1/intercellular adhesion molecule-1 interaction. *Biophys.J.*, 83(4): 2270–2279, 2002a.

X. H. Zhang, E. Wojcikiewicz, and V. T. Moy. Force spectroscopy of the leukocyte function-associated antigen-1/intercellular adhesion molecule-1 interaction. *Biophys.J.*, 83(4):2270–2279, 2002b.

X. H. Zhang, A. Chen, D. De Leon, H. Li, E. Noiri, V. T. Moy, and M. S. Goligorsky. Atomic force microscopy measurement of leukocyte-endothelial interaction. *American Journal of Physiology-Heart and Circulatory Physiology*, 286(1):H359–H367, 2004a.

X. H. Zhang, S. E. Craig, H. Kirby, M. J. Humphries, and V. T. Moy. Molecular basis for the dynamic strength of the integrin alpha(4)beta(1)/vcam-1 interaction. *Biophys.J.*, 87 (5):3470–3478, 2004b.

Q. Zhong, D. Inniss, K. Kjoller, and V. B. Elings. Fractured polymer/silica fiber surface studied by tapping mode atomic force microscopy. *Surf.Sci.*, 290(1-2):L688–L692, 1993.

Chapter 2

Aims of the thesis

General aim

To improve and apply AFM methodology to measure the viscoelastic and adhesion properties of living cells, highlighting the importance of probe geometry.

Specific aims

1. To design and set-up a stand-alone 3D system based on AFM specially designed to probe viscoelasticity and adhesion on living cells under controlled environmental conditions.

2. To develop a contact model of a blunted pyramidal tip, and to assess the suitability of pyramidal tips for probing mechanical properties of soft gels and living cells.

3. To validate cylindrical cantilever tips modified by FIB for probing mechanical properties of biopolymers by AFM.

4. To study the effects of thrombin on RGD mediated adhesion and on stiffness of alveolar epithelial cells using cylindrical AFM cantilever tips.

Chapter 3

AFM based system for probing mechanics of living cells

3.1 Abstract

In this work it is presented a 3D stand-alone system based on atomic force microscopy specially designed to study the mechanical properties of living cells. The system uses servocontrolled piezoelements to precisely positioning the cantilever probe. The cantilever deflection is measured using the optical lever method with a near IR light source and a four segment photodiode. The system is mounted on the stage of an inverted optical microscope and can work together with the acquisition of fluorescent or phase contrast images of the samples.

3.2 Introduction

The field of cellular mechanics has grown in the recent decades due to the development of new micro- and nanomanipulation techniques. Many tools, such as magnetic twisting cytometry (Fabry et al., 2001), microplates (Thoumine et al., 1996), or optical tweezers (Henon et al., 1999) have been used to study the viscoelastic properties of living cells or the interactions with their microenvironment, such as adhesion or friction. Among these techniques, one of the most useful tools is AFM. It allows to obtain both morphological information and viscoelastic and interaction properties of living cells under physiological conditions (Rotsch and Radmacher, 2000; Benoit and Gaub, 2002). AFM uses a flexible cantilever with a tip at its end to indent, pull or tear the samples using piezoelectric positioning elements. Forces applied to the samples are computed by measuring the deflection of the cantilever and knowing its spring constant. Although AFM was early used to mea-

sure mechanical properties of samples (Weisenhorn et al., 1989; Burnham and Colton, 1989; Weisenhorn et al., 1993; Hoh and Schoenenberger, 1994), commercially available AFM systems (AFMs) are mainly thought to obtain topographical images of the sample. Even if there is a number of available apparatus specially designed for biological purposes, they still lack of very important features required in cellular biology. First of all, commercial AFMs use to carry precalibrated piezoelectric elements without position sensors, such as strain gauges or capacitors, to directly measure the displacement. This implies that the positioning of the probe (or sample) may be influenced by important hysteresis and creep effects, inherent to piezoelements, that may introduce artifacts in the measurements. The use of position sensors allows the servocontrolled displacement of the probe (or sample), the application of well known waveform movements, and the direct measurement of the displacement, although it reduces the dynamical response. In the particular case of cell biology, another problem arises with commercial systems due to the typical dimensions of the cells, tens of microns, and the limited vertical range of the positioners, $\sim 6\ \mu$m . The limited range of the vertical displacement becomes even more important when probing adhesion properties of living cells, where high amplitude force curves are necessary (Benoit and Gaub, 2002). When studying living systems, it is also very important to control their environmental conditions: culture medium, temperature or PH during measurements. For instance, when monitoring changes in the mechanical properties of living cells during drug addition (Buscemi, 2004). A perfusion system and a temperature controller may be thus necessary if drug treatments or environmental changes are intended. Many of the commercial AFMs do not allow the easy addition of such accessories due to the reduced area available to place and manipulate the sample. Most of commercial AFM systems designed for biological purposes move the cantilever instead of the sample. In such configuration it is necessary to refocus or realign the laser spot continuously as the cantilever moves. This refocus may introduce systematic deviations from the ideal response of the optical beam deflection method (Hansma et al., 1994). A common artifact present in AFM measurements are interference fringes due to the laser light reflected off the cantilever and the light reflected off the sample (Cappella and Dietler, 1999). This interference is detected by the photodiode as an oscillatory wave. The use of a laser source with low coherence and the minimization of the light that reaches the sample may reduce this problem. Another important issue is the possibility of calibrating the spring constant of the cantilever. This is essential when accurate force measurements are intended. The most used technique for calibration is the thermal fluctuations method (Hutter and Bechhoefer, 1993). This method uses the first resonant peak of the thermal fluctuations spectrum of the cantilever which is usually centered at few kHz. Few are the

AFM systems that allow measuring the thermal fluctuations of the cantilever deflection at high enough sampling rates, and lesser are those which have an implemented tool to do so. To accurate probe the desired cells, or even specific regions within the cells, it is important to optically visualize the sample together with the probe with a certain accuracy. It is thus essential the possibility of optically visualize the samples during AFM measurements. Commercial AFMs designed for biological purposes use to be mounted on the stage of an inverted optical microscope. However, the optical path of the microscope used to be interrupted and transmission imaging is only achieved by lateral illumination. Therefore, common optical techniques, such as phase contrast or DIC (or Nomarski), are difficult or impossible to integrate with the AFM. It seems, thus, that several improvements can be introduced to AFM to better study living cells.

The aim of the work was to design and set-up a stand-alone 3D system based on AFM specially designed to probe viscoelasticity and adhesion on living cells under controlled environmental conditions. The system includes position sensors in the high range piezoelectric elements. The 3D positioning is controlled with analog feedback electronics to overcome the hysteresis and nonlinearity of the piezoelements and by custom made programs. It is mounted on an inverted optical microscope with integrated Phase Contrast, DIC, and Fluorescence optical microscopy components. Its free optical path and the infrared laser permits to be used together with all optical components.

3.3 Instrumentation

The configuration scheme of the built force apparatus is shown in Fig. 3.1. The probe and deflection detection system hold together from the XY and Z piezos. These are mounted on an aluminium platform which rests on three micrometer screws (Mitutoyo, Japan) enabling manual vertical positioning with micrometric resolution. The whole system stands on the stage of an inverted optical microscope. The motion system is composed by XY and Z piezoelectric elements with strain gauge position sensors in all three dimensions (Piezosystem Jena GmbH, Germany). The open loop range is 100x100 μm^2 and 38 μm in the XY and Z axis, respectively. The Z motion is servocontrolled with a commercial PID feedback circuit, ENV 40 CSG with a nominal bandwidth of 1 kHz, and its corresponding power supply module ENT 40/20 230V (Piezosystem Jena GmbH, Germany). The X and Y motions are independently servocontrolled by home made PID analog feedback circuits with the corresponding high voltage amplifiers (Fig. 3.2). XY and Z movement is controlled by home made programs based in LabView 7.0 using a 16-bit analog output card (PCI-6733, National Instruments, USA). The deflection and torsion of the cantilever

is measured with the optical lever method. A variable low power (0-15 mW) pigtailed laser 785 nm (Schäfter + Kirchhoff, Germany) beam is focused on the backside of the cantilever, reflected off and detected by a segmented photodiode (S4349, Hamamatsu, Japan). The laser is coupled using fiber optic cable to the collimation and focusing optics. The photodiode holder is magnetically coupled to a 2D-micropositioner to allow us coarse and fine manual centering of the laser spot. A band pass filter can be easily coupled in front of the photodiode in order to reduce not desired light wavelengths. The active area of the photodiode is 3x3 mm^2 divided in 4 segments. An analog circuit (Fig. 3.2) measures the sum (A+B+C+D), top/bottom (A+B-C-D) and left/right (A+C-B-D) difference signals corresponding to the total luminosity falling on the photodiode. This signals are transformed into deflection and torsion of the cantilever by calibrating the photodiode signal before each measurement. The photodiode and position sensor signals are optionally antialiasing filtered (Low Pass Filter, Butterworth, 8 poles, cut-off frequencies 33, 225, or 22000 Hz) and sampled with a 16-bit data acquisition card (PCI-6036E, National Instruments, USA).[1]

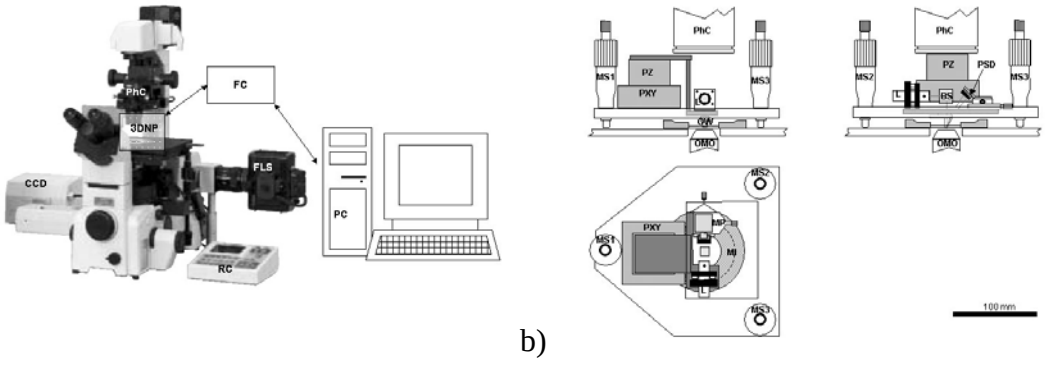

a) b)

Figure 3.1: a) **3DNP**: 3D NanoProbe system, **CCD**: refrigerated CCD camera, **PhC**: Phase contrast rings, **RC**: fluorescent filters, shutter and focusing remote control, **FLS**: fluorescence light source, **CE**: control electronics (Fig. 3.2), **PC**: personal computer. b) System sketch: **PZ**: Z-piezo; **PXY**: XY-piezo; **L**: laser with mount; **PSD**: photodetector with mount; **PhC**: phase contrast rings; **MS**: micrometric screws; **BS**: beamsplitter; **OW**: optical window; **MI**: microincubator; **OMO**: optical microscope objective; **MS**: microscrews

The whole system is mounted on an XY micropositioned stage which slides on the stage of a inverted optical microscope TE2000 (Nikon, Japan) with motorized and remotely controlled light shutter, fluorescence filters and focusing systems. Two CCD cameras are connected to the optical microscope. One for bright field, phase contrast, or DIC

[1] Photodiode detection electronics and XY positioning feedback circuits with low-pass filters were developed in our laboratory my Miguel Ángel Rodríguez.

imaging Marlin (Allied Vision Technologies GmbH, Germany). And a deep cooled CCD camera ORCA-AG (Hamamatsu, Japan) for FRET and epi-fluorescence imaging. Both cameras are connected to the personal computer via the firewall port. Data acquisition cards are mounted on PCI ports of the personal computer and controlled by home-made programs.[2]

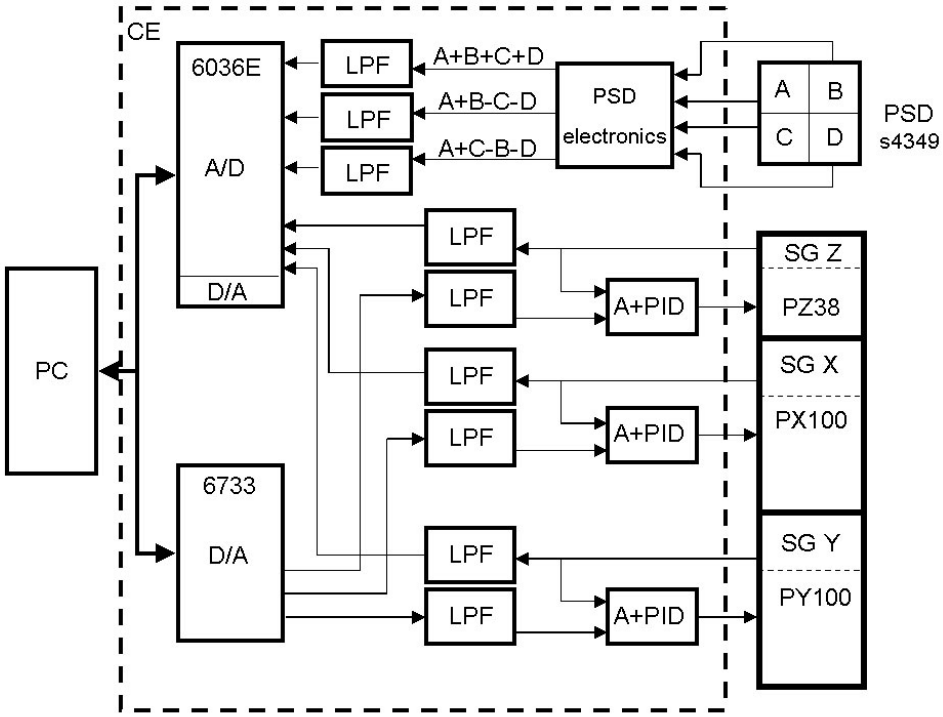

Figure 3.2: Control electronics (**CE** in Fig. 3.1a): 4-segment photodiode (**PSD**), **PZ**: Z piezo with strain gauge sensor (**SG Z**); **PX**: X piezo with strain gauge sensor (**SG X**); **PY**: Y piezo with strain gauge sensor (**SG Y**); **A+PID**: amplifiers and PID circuits; **LPF**: low pass filters; **A/D**: analog/digital input card; and **D/A**: digital/analog output card.

3.4 Validation

3.4.1 Positioning System

One of the most important improvements of the presented force apparatus is the servo-controlled positioning system. The use of strain gauge sensors in the three axis of motion achieves a positioning with accurate resolution and high repeatability. The XY piezoelements enables a resolution of 1 nm in closed loop mode and subnanometer resolution in

[2]Various past and current members of our lab contributed to the development of the acquisition and control software, although a special mention may be done to Daniël ten Bloemendal.

open loop. The Z piezoelectric nominal resolution is even better being 0.7 nm in closed loop and 0.05 nm in open loop. In addition the use of feedback circuits to control the motion enables to reach a repeatability of 63 nm and 47 nm in the XY and Z axes, respectively. The calibration of the XY SG sensors was achieved as follows: a reference sample (spherical beads glued to a coverslip) was attached to the piezopositioning system; different voltages (from 0 to 100 V and return) were applied to the piezo with the servocontrol activated and the SG voltage was measured, a 40X bright field image of the reference sample was acquired at the different applied voltages, *i.e*, different positions. The images were then processed with an algorithm based on crosscorrelations which calculated the relative translational shift between images (in pixels). The shift was then converted into length dimensions knowing the conversion factor (μm per pixel) for the particular microscope and camera used. The resulting calibration plot is shown Fig. 3.3. Notice the strong linearity of strain gauge sensors.

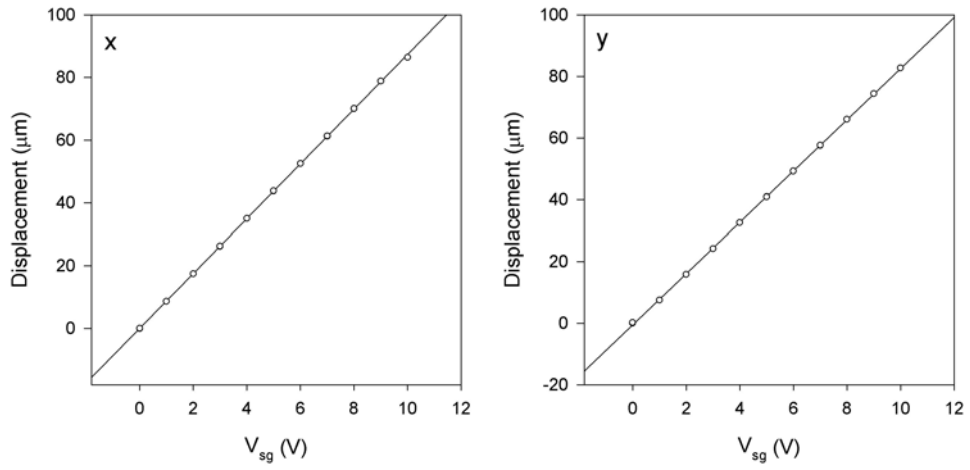

Figure 3.3: XY Strain gauge calibration. Relative translational displacement between images versus measured SG voltage for the X (left) and Y (right) piezoelectric elements.

In closed loop mode, the motion range was slightly reduced to ~85x85 μm^2 and 32 μm in the XY and Z directions, respectively. The actual frequency bandwidth was tested experimentally for both control electronic systems obtaining good performances in the full motion range for frequencies up to 20 Hz. However, at lower amplitudes (few hundred nm) an oscillation frequency of 90 Hz was reached with minimum distortion of the waveform amplitude. The bandwidth in open loop mode was mainly limited by inertial forces. The use of custom made programs enables the application of different and precise waveforms to the positioning system. By the moment, the acquisition of topographical images is not possible with such instrumentation. A tunable PID feedback circuit may be

needed to keep a constant deflection during scanning in real time.

3.4.2 Optical lever method

It is important to notice the improvement made in the optical lever method used to detect the deflection of the cantilever. In our configuration, both the deflection detection system and the probe holds on a same stage. This allows the synchronized motion of probe, laser beam and photodiode avoiding the refocus and realignment of the laser spot and the reflected beam, usually required in commercial AFM systems.

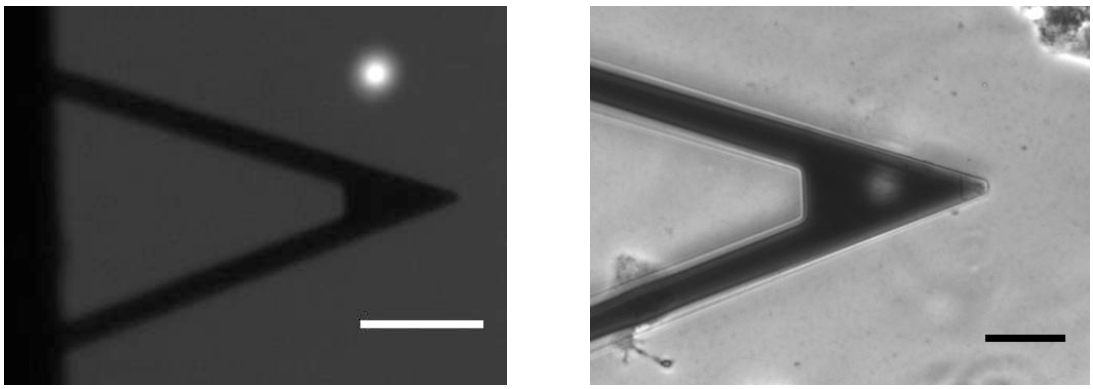

Figure 3.4: Laser spot dimensions. The spot size is small enough (~16 μm diameter, left) to not overcome the cantilever width (right), minimizing the transmitted light that reaches the sample. Scale bars stand for 100 and 50 μm, respectively.

The pigtailed laser, the collimator, and the focusing lens result in a gaussian-shaped spot of 16 μm diameter at the cantilever plane, not exceeding the dimensions of common cantilevers (Fig. 3.4) and enabling almost the total reflection of the laser light. The reduced size and the low power of the laser source bring three main advantages: 1) few IR light arrives at the sample, minimizing the heating and the photobleaching of possible fluorescent labels; 2) little laser light reaches the optical path of the microscope interfering with the image acquisition; and 3) the tiny spot reduces the laser light reflected off the sample minimizing the typical interference fringes in the *F-z* curves. Interference is also reduced by the low coherence of the laser source.

The linearity of the photodiode was also validated. We used an optical bench to align the laser beam and the photodiode, separated by a distance similar to that at which they will remain in the final AFM configuration. The PSD was placed on a 2D micropositioner that enabled us to displace the photodiode in the vertical and horizontal directions with a resolution of 0.5 μm . The vertical (deflection, A+B-(C+D)) and horizontal (torsion, A+C-(B+D)) voltage signals were measured for vertical and horizontal 0.5 μm steps of

the PSD. The resulting voltage versus displacement plots are shown in Fig. 3.5. As can be observed, the photodiode signal was proportional to the displacement of the laser spot, reflecting the linearity of the position detection system. Deviations from the ideal response may be attributed to misalignment of the micropositioning system and not from non linearities of the photodiode.

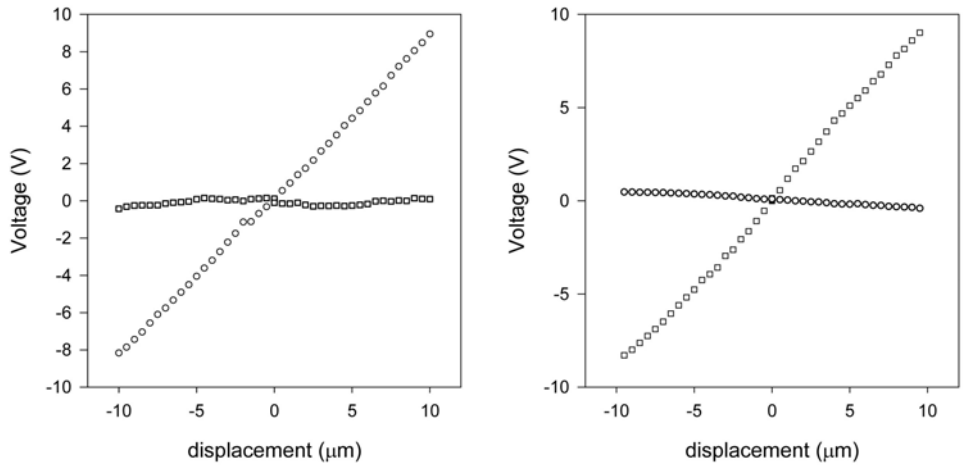

Figure 3.5: Linearity test of the photodiode. Vertical (deflection, A+B-(C+D), *circles*) and horizontal (torsion, A+C-(B+D), *squares*) signals versus vertical (left) and horizontal (right) displacement of the PSD.

3.4.3 Optical Microscopy

As mentioned before, the force apparatus is mounted on the stage of an inverted optical microscope. The reduced height of our system and the free optical path enables us the use of phase contrast rings (Fig. 3.6) and DIC polarizer, prism and condenser. The near IR light in the optical lever detection system makes possible the use of epi-fluorescence filters without interferences with the laser beam. The optical microscope carry objectives with magnifications up to 60x. The revolving nosepiece focusing, the fluorescent filters and the shutters are motorized and can be controlled with the computer. The cooled CCD camera has the possibility of manually switch on and off the refrigeration system. These remote controls minimize the mechanical coupling with the force apparatus. Therefore, all the optical microscope resources can be used together with the apparatus with minimal mechanical interfering with the force detection system.

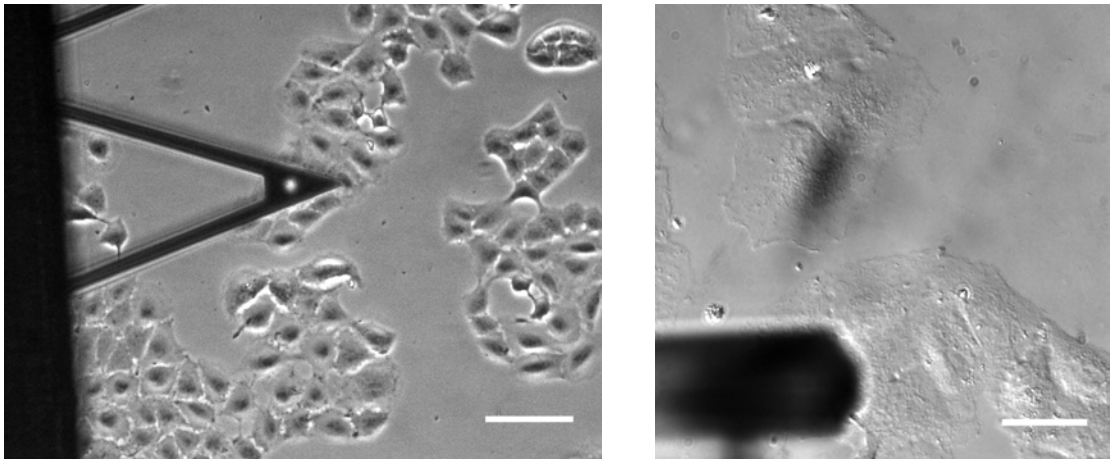

Figure 3.6: Phase contrast image (left) of a V-shaped cantilever above above alveolar epithelial (A549) cells obtained with a 10x objective (bar = 100 μm). Nomarski image of A549 cells acquired with a 40x objective (right). The shadow of a rectangular cantilever can be observed (bar = 30 μm).

3.4.4 Controlled environment

The force device was designed with a wide and clear front aperture to access the sample. A temperature controlled microincubator (MI) is easily appended as shown in Fig. 3.1b. The temperature of the samples can be servocontrolled from ~0ºC to ~55ºC, allowing physiological conditions (37ºC). The culture medium in which samples are immersed can be removed and added using a perfusion pump or simply with a micropipette. The perfusion system is a key feature when drug treatments are intended.

3.4.5 Cantilever spring constant calibration

The data acquisition card enables us to acquire the deflection signal with a high sampling frequency (up to 50 kS/s). This enables us to record the thermal fluctuations of the cantilever with enough frequency bandwidth to detect the first, and even second, oscillation mode of the cantilever and determine its spring constant using the thermal fluctuations method (Hutter and Bechhoefer, 1993) (see also Appendix B). The main control software incorporates a calibration program based in Matlab 7.0 that computes the cantilever spring constant before carrying out the measurements.

3.5 Applications

Mechanical measurements on living cells are usually obtained by means of the so-called force-distance curves: a triangular waveform is applied to the vertical direction, and the deflection is measured as the tip indents the sample. Adhesion studies are carried out using this technique but analyzing the retracting part of the curve. Measuring the torsion of the cantilever, as the tip scans horizontally the sample surface, allows us the study of friction properties. The main application our device is designed for is the measurement of viscoelastic and adhesion properties of living cells. The use of soft cantilevers (spring constant ~10 mN/m) enables us to apply and measure forces at the pN level, which is the order of magnitude of the forces involved in cellular processes. The elasticity of materials is commonly described by means of its Young's modulus (E), and the viscoelasticity by using the complex shear modulus ($G^*(\omega)$, being ω the excitation frequency). E is obtained from high amplitude force-distance curves fitted with a certain contact elastic model (Radmacher et al., 1996; Alcaraz et al., 2003). A representative example of a *d-z* curve obtained on a pulmonary living cell is shown in Fig. 3.7. $G^*(\omega)$ is obtained by applying low amplitude sinusoidal oscillations at a certain indentation and computing the ratio of the Fourier transforms of excitation and response (Mahaffy et al., 2000; Alcaraz et al., 2003). The force apparatus enables us the application of a superposition of waves at different frequencies to the vertical motion. Thus, it is easy to estimate the frequency response of living cells under changing conditions with a single measurement.

Apart from nanoindentation applications, the system allows us to measure adhesion properties on living cells. Adhesion properties are very important to the structural stability and mechanics of living cells. Adhesion reflects the mechanical interaction of cells with their surroundings. Living cells express different membrane proteins (such as selectins or integrins) to regulate their adhesion to neighboring cells or to the extracellular matrix. Adhesion measurements can be carried out by coating AFM cantilevers with binding sites from the extracellular matrix or other cells. The coated cantilever approaches the sample surface, makes contact and the detachment interaction is measured when retracting as a negative deflection in the *F-z* curves. Adhesion can be studied at two main levels: single molecule and multiple measurements. The force apparatus is specially designed to operate in this last mode where large collectivities of adhesion sites are involved. This collectivities can induce high detachment forces (few nN) and a high Z range is required. The use of a 38 μm piezo in the vertical direction is enough to study adhesion without limitations of low travel range, usual in most of the commercially available AFM systems. Figure 3.8 shows a representative example of a retraction curve obtained using a spherical

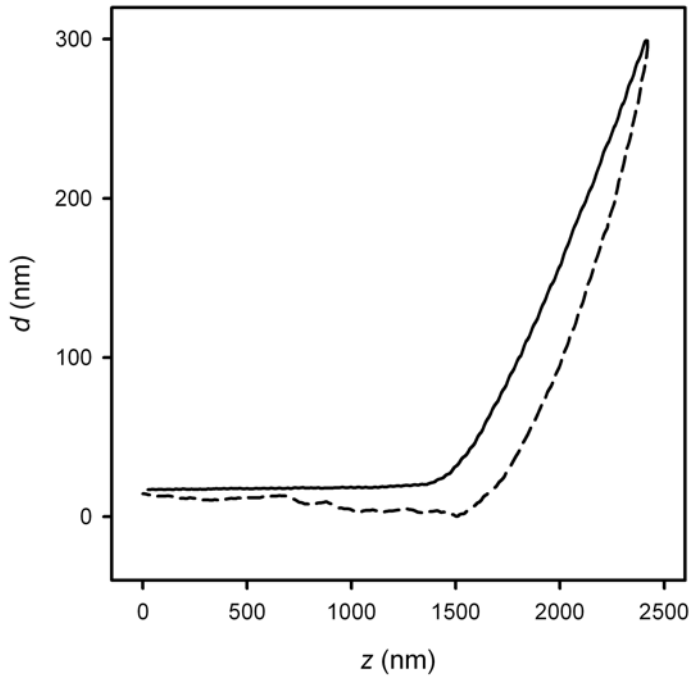

Figure 3.7: Deflection-distance (*d*-*z*) curve obtained with a spherical cantilever tip (R = 2500 nm, k = 0.01 N/m) on an alveolar epithelial cell in culture (peak-to-peak amplitude 2.5 μm/s at 0.3 Hz). Solid and dashed lines stands for approach and retract curves, respectively.

cantilever tip coated with ECM proteins on a living alveolar epithelial cell.

It is widely accepted that the major responsible of the mechanical behavior of living cells is its microfilament cytoskeleton (CSK). New fluorescence staining techniques, such as Green Fluorescent Protein transfection, enables us in vivo labelling of the different components of the CSK. The presented system allows us simultaneous acquisition of mechanical and adhesion measurements and fluorescence images of living cells. Thus, studies on how the CSK is affected under changes in the environmental conditions (drug addition, temperature...) or under mechanical deformation are easy to implement. Living cells have shown to be heterogeneous systems with different properties depending on its internal structure. Thus, their mechanical behavior depends on the probed location within the cell. Phase contrast imaging allows us to visualize the nucleus and other intracellular structures. The high precision of the positioning system, together with the phase contrast microscopy, makes the system very suitable to measure viscoelastic and adhesion properties at precise regions within cells.

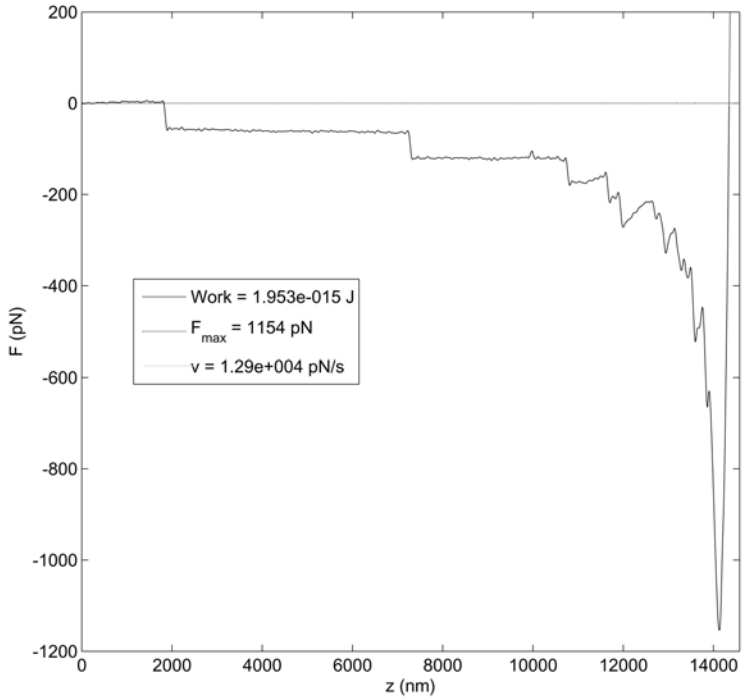

Figure 3.8: Detachment Force-distance *F-z* curve (solid line) obtained with a spherical cantilever tip (R = 2500 nm, k = 0.01 N/m) coated with RGD peptide on an alveolar epithelial cell in culture (retraction speed 1.5 μm/s). Dotted line shows the zero force reference.

3.6 Conclusions and perspectives

We have developed an force device based on AFM especially designed to study mechanical properties of living cells, such as viscoelasticity or adhesion. The system is mounted on the stage of an inverted optical microscope. It is designed to work together with fluorescence, bright field or phase contrast microscopy techniques, enabling the acquisition of optical images with a magnification up to 60x. The system can be used under different environmental conditions thanks to the microincubator and the perfusion system. A future improvement of the system may be the development of a tunable PID feedback circuit to control the force applied to the samples. This will allow us the acquisition of contact mode images of living cells.

Bibliography

J. Alcaraz, L. Buscemi, M. Grabulosa, X. Trepat, B. Fabry, R. Farre, and D. Navajas. Microrheology of human lung epithelial cells measured by atomic force microscopy. *Biophys.J.*, 84:2071–2079, 2003.

M. Benoit and H. E. Gaub. Measuring cell adhesion forces with the atomic force microscope at the molecular level. *Cells Tissues Organs*, 172(3):174–189, 2002.

N. A. Burnham and R. J. Colton. Measuring the nanomechanical properties and surface forces of materials using an atomic force microscope. *J.Vac.Sci.Technol.A*, 7(4):2906–2913, 1989.

L. Buscemi. Estudi mitjançant microscòpia de força atòmica de la mecànica de cèl.lules epitelials alveolars en resposta a trombina. 2004.

B. Cappella and G. Dietler. Force-distance curves by atomic force microscopy. *Surface Science Reports*, 34(1-3):1–+, 1999.

B. Fabry, G. N. Maksym, J. Butler, M. Glogauer, D. Navajas, and J. J. Fredberg. Scaling the microrheology of living cells. *Phys.Rev.Lett.*, 87:148102–148105, 2001.

P. K. Hansma, B. Drake, D. Grigg, C. B. Prater, F. Yashar, G. Gurley, S. V. Eling, S. Feinstein, and R. Lal. A new, optical-lever based atomic-force microscope. *J.Appl.Phys.*, 76(2):796–799, 1994.

S. Henon, G. Lenormand, A. Richert, and F. Gallet. A new determination of the shear modulus of the human erythrocyte membrane using optical tweezers. *Biophys.J.*, 76 (2):1145–1151, 1999.

J. H. Hoh and C. A. Schoenenberger. Surface morphology and mechanical properties of mdck monolayers by atomic force microscopy. *J.Cell Sci.*, 107(Pt 5):1105–1114, 1994.

J. L. Hutter and J. Bechhoefer. Calibration of atomic-force microscope tips. *Rev.Sci.Instr.*, 64(7):1868–1873, 1993.

R. E. Mahaffy, C. K. Shih, F. C. MacKintosh, and J. Kas. Scanning probe-based frequency-dependent microrheology of polymer gels and biological cells. *Phys.Rev.Lett.*, 85:880–883, 2000.

M. Radmacher, M. Fritz, C. M. Kacher, J. P. Cleveland, and P. K. Hansma. Measuring the viscoelastic properties of human platelets with the atomic force microscope. *Biophys.J.*, 70(1):556–567, 1996.

C. Rotsch and M. Radmacher. Drug-induced changes of cytoskeletal structure and mechanics in fibroblasts: an atomic force microscopy study. *Biophys.J.*, 78:520–535, 2000.

O. Thoumine, A. Ott, and D. Louvard. Critical centrifugal forces induce adhesion rupture or structural reorganization in cultured cells. *Cell Motil.Cytoskeleton*, 33(4):276–287, 1996.

A. L. Weisenhorn, P. K. Hansma, T. R. Albrecht, and C. F. Quate. Forces in atomic force microscopy in air and water. *Appl.Phys.Lett.*, 54(26):2651–2653, 1989.

A. L. Weisenhorn, M. Khorsandi, S. Kasas, V. Gotzos, and H. J. Butt. Deformation and height anomaly of soft surfaces studied with an afm. *Nanotechnology*, 4:106–113, 1993.

Chapter 4

Probing mechanical properties of living cells by atomic force microscopy with blunted pyramidal cantilever tips

4.1 Abstract

Atomic force microscopy allows the acquisition of high resolution images and the measurement of mechanical properties of living cells under physiological conditions. AFM cantilevers with blunted pyramidal tips are commonly used to obtain images of living cells. Measurement of mechanical properties with these tips requires a contact model which takes into account their blunted geometry. The aim of this work was to develop a contact model of a blunted pyramidal tip, and to assess the suitability of pyramidal tips for probing mechanical properties of soft gels and living cells. We developed a contact model of a blunted pyramidal tip indenting an elastic half-space. We measured Young's modulus (E) and the complex shear modulus ($G^* = G' + iG''$) of agarose gels and A549 alveolar epithelial cells with pyramidal tips and compared them with those obtained with spherical tips. The gels exhibited an elastic behavior with almost coincident loading and unloading force curves and negligible values of G''. E fell sharply with indentation up to ~300 nm, showing a linear regime for deeper indentations. A similar indentation dependence of E with twofold lower values at the linear regime was obtained with the spherical tip fitted with Hertz's model. The dependence of E on indentation in cells paralleled that found in gels. Cells exhibited viscoelastic behavior with $G''/G' \sim 1/4$. Pyramidal tips commonly used for AFM imaging are suitable for probing mechanical properties of soft gels and living cells.

4.2 Introduction

The mechanical properties of the cell play a key role in determining cell shape and changes during essential functions such as contraction, crawling and migration. New microscopy and nanomanipulation techniques have led to a dramatic increase in our knowledge of the morphology and mechanical properties of cells. One of the most powerful tools is atomic force microscopy, which allows us to obtain topographical images and to probe mechanical properties of living cells under physiological conditions (Rotsch and Radmacher, 2000). Moreover, AFM can be used to monitor dynamic changes in the shape and mechanics of the cell during pharmacological treatments.

AFM uses a flexible cantilever with a sharp tip at its end to probe the sample surface. Images are obtained by scanning the surface of the sample with the cantilever tip. The sharpness of the tip, apart from other characteristics such as sample stiffness, determines image resolution (Heuberger et al., 1996). Soft silicone nitride AFM cantilevers with pyramidal tips are commonly used for obtaining high resolution images of living cells (You and Yu, 1999; Tortonese, 1997). Pyramidal tips are blunted or rounded at the apex. Despite their bluntness, they are sharp enough to resolve subcellular structures of living cells, such as the cytoskeleton, which plays the main role in cellular mechanics (Heidemann and Wirtz, 2004; Henderson et al., 1992; Charras and Horton, 2002; Lal et al., 1995; You et al., 2000; Huang et al., 2004).

The cell mechanics are probed with AFM by indenting the surface of the cell with the tip of the cantilever and measuring the force-indentation (F-δ) relationship. Mechanical parameters of the sample are usually estimated by fitting F-δ data with a suitable contact model taking into account the geometry of the probe. The Hertz theory (Hertz, 1881) is the most common approach to analyzing contact mechanics. This approach is based on infinitesimal strains and assumes linear elastic, isotropic, axisymmetric, perfectly smooth and semi-infinite bodies in contact with each other over a small region of their surface (Hertz, 1881). In particular, Hertz's theory leads to analytical solutions for spherical and conical tips indenting an elastic half-space (Johnson, 1985). Assuming a spherical geometry of the tip apex, the spherical Hertz model has been applied to pyramidal tips to determine mechanical properties of biopolymer gels and living cells (Radmacher et al., 1995, 1993; Shroff et al., 1995). This model fails for indentations larger than the apparent radius of curvature of the tip (10 – 50 nm). For deep indentations, pyramidal tips have been modeled as cones (Radmacher et al., 1995; Wu et al., 1998). A blunted cone model has been developed for a wider range of indentations (Briscoe et al., 1994; Mathur et al., 2001). However, the actual geometry of pyramidal tips is not a blunted cone but a

blunted pyramid. A contact model for an ideal pyramid has been numerically developed by Bilodeau (Bilodeau, 1992). This pyramidal model has recently been used to probe mechanical properties of living cells at deep indentations (Alcaraz et al., 2003). To the best of our knowledge, a more detailed pyramidal contact model taking into account the blunt geometry of conventional AFM pyramidal tips has not been developed.

The use of a cantilever with a microsphere attached at its end has recently been proposed to indent the sample with a simple contact geometry and to minimize strain (Dimitriadis et al., 2002; Mahaffy et al., 2000). Cantilevers with microspheres ranging ~1 to ~10 μm in diameter have been used to probe biopolymer gels and living cells (Mahaffy et al., 2000; Dimitriadis et al., 2002; Mahaffy et al., 2004; Shoelson et al., 2004). Sample mechanical properties were estimated by fitting indentation data with the Hertz spherical model. Although a microsphere provides a simple contact geometry for probing mechanics, the use of this tip yields low resolution images that may not reflect the actual topography of some samples (Stolz et al., 2004). Replacing the cantilever between imaging and mechanical measurements is difficult and time consuming. This may be suitable for large, stable and uniform samples but not for living cells since they have a complex shape and exhibit heterogeneous and time-varying mechanical properties. Moreover, the mechanics and shape of the cell change during spontaneous contraction and locomotion and in response to pharmacological stimuli. The use of a single cantilever for imaging and indentation enables us to precisely correlate the shape and mechanics of living cells. Pyramidal tips commonly used for AFM imaging could be suitable for probing cell mechanics. Moreover, measurements at low indentations could be improved by developing a blunted pyramidal model that takes into account the blunted geometry of the tip.

The aim of this work was to develop a contact model of a blunted pyramidal tip and to assess the suitability of AFM pyramidal tips for probing mechanical properties of soft biopolymer gels and living cells. We first developed a contact model of a blunted regular pyramid indenting an elastic half-space. We probed soft samples of agarose gels and living human alveolar epithelial cells with pyramidal and spherical tips using the blunted pyramidal model and the spherical Hertz model, respectively. The Young modulus (E) and the complex shear modulus ($G^*(\omega)$) estimated with the pyramidal and spherical tips were compared.

4.3 Theory

4.3.1 Contact model of a blunted pyramid indenting an elastic half-space

Force-indentation relationship, $F(\delta)$, for a blunted $n-$sided rigid regular pyramid of semi-included angle θ, tip defect h, and spherical cap radius R_c (Fig. 4.1) was derived using Betti's reciprocal theorem (Ugural and Fenster, 1987). Accordingly, the total force F applied by a tip with an arbitrary shape and projected area A was computed from the pressure distribution of a flat indenter ($p^*(r, \varphi)$) of plan-form A

$$F = \iint_A p^*(r,\varphi)\frac{f(r,\varphi)}{\delta^*}\, r\, dr\, d\varphi, \tag{4.1}$$

where δ^* is the indentation depth for the flat indenter and $f(r, \varphi)$ is the interpenetration function for the tip. The analytical form of $p^*(r, \varphi)$ is known only for elliptical contact areas. Thus, only in this case a closed-form solution of Eq. 4.1 can be obtained. Nevertheless, $p^*(r, \varphi)$ and therefore F can be approximated in the Rayleigh-Ritz sense, *i.e.*, by using the best elliptical approximation to the actual contact area (Barber and Billings, 1990).

For a regular $n-$sided pyramid, the cross section at any indentation depth is a regular $n-$sided polygon. Therefore, its best elliptical approximation is a circle of radius a centered on the axis of the pyramid, and the pressure distribution of the corresponding flat indenter is that of a cylindrical punch of radius a

$$p^*(r,\varphi) = \frac{E}{\pi(1-\nu^2)}\frac{\delta^*}{(a^2-r^2)^{1/2}}, \tag{4.2}$$

substituting this expression into Eq. 4.1 we obtain

$$F = \frac{E}{\pi(1-\nu^2)}\iint_A \frac{f(r,\varphi)}{(a^2-r^2)^{1/2}} r\, dr\, d\varphi\,, \tag{4.3}$$

where E is Young's modulus and ν Poisson's ratio.

The blunted pyramid was modelled as a spherical cap which transforms smoothly into an n-sided pyramid (Fig. 4.1) according to the following interpenetration function

$$\begin{aligned} &f(r) = \delta - \tfrac{r^2}{2R_c} \qquad\qquad 0 \le a < b \\ &f(r,\varphi) = \delta - \tfrac{r-b}{\tan\theta}\cos\left(\varphi - \tfrac{2k\pi}{n}\right) - h^* \quad a \ge b \quad \tfrac{(2k-1)\pi}{n} < \varphi < \tfrac{(2k+1)\pi}{n} \quad k = 0, 1, ..., n-1 \end{aligned} \tag{4.4}$$

where b is the radial distance corresponding to the transition from spherical cap to pyrami-

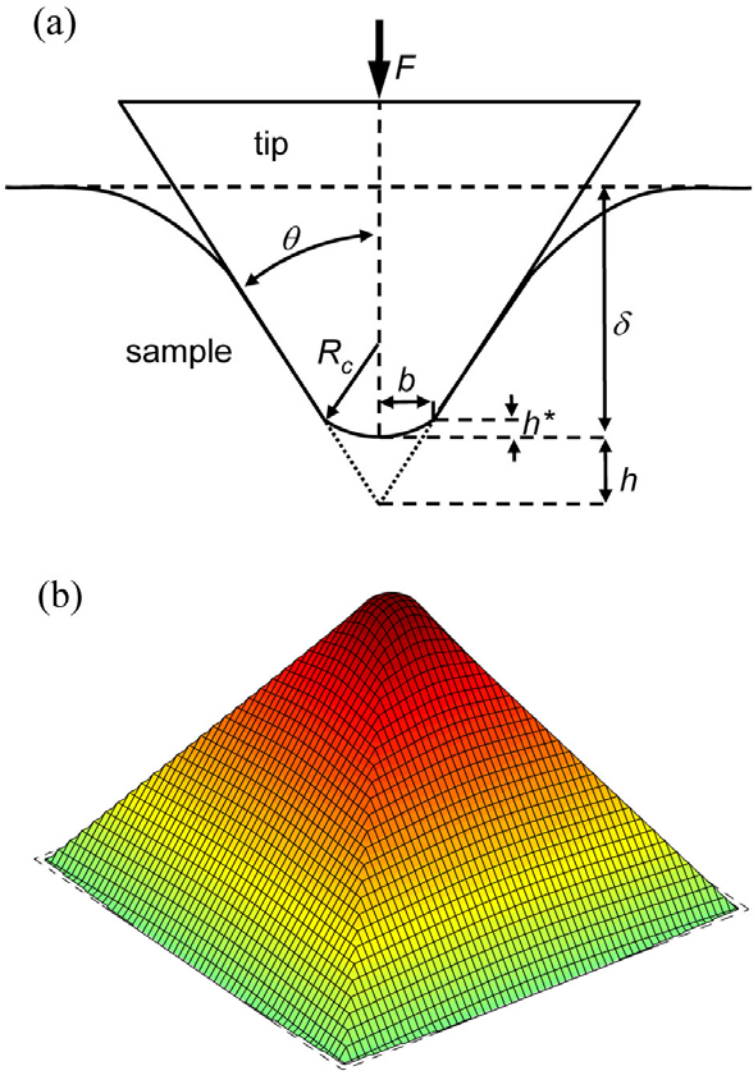

Figure 4.1: Model of the blunted pyramidal AFM tip. (a) Section of a blunted pyramidal tip with semi-included angle θ, tip defect h, and spherical cap radius R_c indenting an elastic half-space. F is force, δ is indentation, b is the radial distance corresponding to the transition from spherical cap to pyramidal faces, and $h^* = b^2/2R_c$. (b) 3D plot of the end (1 μm) of the blunted four-sided pyramidal tip model with the spherical cap merging tangential with the pyramid faces (θ = 35 deg, R_c = 100 nm). Dashed lines are the contour corresponding to flat faces (ideal pyramid).

dal faces and $h^* = b^2/(2R_c)$. For the particular case in which the sphere merges tangential with the pyramid faces $b = R_c\cos\theta$, and the geometrical parameters of the tip are reduced to R_c (or b) and θ.

For $a < b$, $f(r)$ is the interpenetration function of a spherical punch of radius R_c, thus $F(\delta)$ is the spherical Hertz model (Hertz, 1881)

$$F = \frac{4E}{3(1-\nu^2)} R_c^{1/2}\delta^{3/2}. \tag{4.5}$$

For $a > b$

$$\begin{aligned} F &= n\tfrac{E}{\pi(1-\nu^2)}\left[\int_0^b \int_{-\frac{\pi}{n}}^{\frac{\pi}{n}} \left(\delta - \tfrac{r^2}{2R_c}\right)\tfrac{r\,dr\,d\varphi}{(a^2-r^2)^{1/2}} + \int_b^a \int_{-\frac{\pi}{n}}^{\frac{\pi}{n}} \left(\delta - \tfrac{r-b}{\tan\theta}\cos\varphi - h^*\right)\tfrac{r\,dr\,d\varphi}{(a^2-r^2)^{1/2}}\right] \\ &= \tfrac{2E}{1-\nu^2}\left[\delta a - \tfrac{n}{\pi}\sin\left(\tfrac{\pi}{n}\right)\tfrac{a^2}{2\tan\theta}\left(\tfrac{\pi}{2} - \arcsin\tfrac{b}{a}\right) - \tfrac{a^3}{3R_c} + (a^2-b^2)^{1/2}\left(\tfrac{n}{\pi}\sin\left(\tfrac{\pi}{n}\right)\tfrac{b}{2\tan\theta} + \tfrac{a^2-b^2}{3R_c}\right)\right] \end{aligned} \tag{4.6}$$

Owing to the symmetry of the n lateral edges, the contribution of each integration range ($(2k\text{-}1)\pi/n$, $(2k+1)\pi/n$) is equal, and the integration over φ is n times the integration over the first range. The effective contact radius a is obtained by imposing $\partial F/\partial a = 0$

$$\delta - \frac{a}{\tan\theta}\frac{n}{\pi}\sin\left(\frac{\pi}{n}\right)\left(\frac{\pi}{2} - \arcsin\frac{b}{a}\right) + \frac{a}{R_c}\left((a^2-b^2)^{1/2} - a\right) = 0. \tag{4.7}$$

Eqs. 4.6 and 4.7 determine the relationship $F(\delta)$ for a blunted n-sided regular pyramid. The indentation is related to the effective radius of contact a by Eq. 4.7.

For the common regular four-sided pyramid of AFM cantilever tips, the above equations simplify to

$$F = \frac{2E}{1-\nu^2}\left[\delta a - \frac{2^{1/2}}{\pi}\frac{a^2}{\tan\theta}\left(\frac{\pi}{2} - \arcsin\frac{b}{a}\right) - \frac{a^3}{3R_c} + (a^2-b^2)^{1/2}\left(\frac{2^{1/2}}{\pi}\frac{b}{\tan\theta} + \frac{a^2-b^2}{3R_c}\right)\right] \tag{4.8}$$

$$\delta - \frac{a}{\tan\theta}\frac{2^{3/2}}{\pi}\left(\frac{\pi}{2} - \arcsin\frac{b}{a}\right) + \frac{a}{R_c}\left((a^2-b^2)^{1/2} - a\right) = 0. \tag{4.9}$$

In the limit $b\to 0$, Eqs. 4.8 and 4.9 lead to $F(\delta)$ for an ideal regular four-sided pyramid

$$F = \frac{1}{2^{1/2}}\frac{E\tan\theta}{(1-\nu^2)}\delta^2, \tag{4.10}$$

with an effective radius of contact $a = \delta\tan\theta/2^{1/2}$.

4.4 Materials and methods

4.4.1 Atomic force microscopy

Measurements were carried out with an AFM (Bioscope, Digital Instruments, CA, USA), mounted on an inverted optical microscope (IX70, Olympus Optical Co. Europe). V-shaped Au coated silicon nitride cantilevers with nominal spring constant k = 10 mN/m with a regular four-sided pyramidal tip of nominal semi-included angle θ=*35 deg* (Microlevers, Thermomicroscopes, Sunnyvale, CA, USA), and similar cantilevers with a spherical polystyrene bead with nominal diameter of 5 μm glued at its end (NovaScan Technologies, Iowa, USA) were used as AFM probes. One pair of pyramidal and spherical cantilevers was used for probing agarose gels, and another pair for probing cells. Cantilevers were cleaned before each set of measurements using piranha solution (70% H_2SO_4, 30% H_2O_2) for the pyramidal tips, and ethanol for the spherical ones. Scanning Electron Microscopy (Zeiss DSM 940-A, Zeiss, Göttingen, Germany) images of the cantilevers were obtained after measurements to determine the actual tip geometries.

4.4.2 Calibration of cantilever spring constants

The spring constants of the cantilevers were determined by the thermal fluctuations method (Hutter and Bechhoefer, 1993). Briefly, the cantilever was modeled as a simple harmonic oscillator. According to the equipartition theorem, each averaged quadratic term of the Hamiltonian of the system is given by $k_BT/2$, where k_B is the Boltzmann constant and T the absolute temperature. Three seconds of cantilever thermal fluctuations were recorded in air away from any surface at room temperature. Data were filtered with an antialiasing filter (Butterworth, 106 kHz, 8 poles) and sampled at 500 kHz by a computer interface board (PCI-MIO-16E-4, National Instruments, Austin, TX, USA). The power spectrum of fluctuation recordings was computed by FFT. The first resonant peak was fitted with a Lorentzian curve plus an offset to reject contributions other than the first oscillation mode due to white noise. The mean square of fluctuations was computed as the area under the curve (P). Invoking the Parseval theorem, the spring constant was computed as k=ck_BT/P, were c is a correction factor c =0.76 for the first vibration mode of a V-shaped cantilever (Stark et al., 2001).

4.4.3 Agarose gel preparation

Purified agarose (Type I-A: Low EEO, A-0169, Sigma, St. Louis, MO, USA) of 0.3% w/v in Millipore RX water was boiled for ~20 minutes stirring continuously. The agarose

solution was poured into a 35 mm diameter petri dish to obtain a gel thickness ~500 μm. A small region of the petri dish was left bare to allow calibration of the AFM photodiode. After gelation of the solution occurs (~5 min), the sample was covered with 2 ml of Millipore RX water and stored at 4^{o}C.

4.4.4 Cell culture

Cell measurements were carried out in living human alveolar epithelial cells, line A549 (CCL-185, ATCC, Manassas, VA, USA). Culture medium consisted of HEPES (Sigma Chemical, St. Louis, MO) buffered RPMI 1640 with 10% inactivated fetal calf serum (Biological Industries, Kibbutz Beit Haemek, Israel), 1mM L-glutamine, 100 U/ml penicillin, 100 mg/ml streptomycin (GIBCO, Gaithersburg, MD, USA) and 2 mg/ml amphotericin B (Bristol - Myers Squibb Co, New Brunswick, NJ, USA). The cells were incubated at 37^{o}C and 5% CO_2. Two days before the experiments, the cells were trypsinized and plated on 10 mm diameter glass coverslips. The culture medium used during experiments was serum free.

4.4.5 Measurements

A petri dish with agarose gel was placed on the temperature controlled stage (Lake Shore Cryotronics, Westerville, OH, USA) of the AFM at 26^{o}C and stabilized for ~30 min with the cantilever immersed in liquid. The AFM photodiode was calibrated by recording 3 force curves in the bare region of the petri dish using a deflection range ~1 μm ($F \approx$10 nN). Ten deflection-distance ($d-z$) curves (triangular oscillations at 0.3 Hz of 3 μm peak-to-peak amplitude) were recorded (2048 points/cycle) in three different regions of each gel. The cantilever was approached until reaching a maximum indentation ~2 μm and ~1 μm for the pyramidal and spherical tips, respectively. After the last $d-z$ measurement, low-amplitude triangular oscillations (100 nm peak-to-peak, 0.3 Hz) were applied at an operating indentation of ~500 nm, and 5 cycles were recorded at 128 points/cycle. Measurements were carried out on 7 agarose gel samples. Each sample was probed with both pyramidal and spherical tips in random order.

A similar protocol of measurements was taken on seven A549 cells from different cultured coverslips. Each cell was probed randomly with both tips at three points of the central region of the cell surface. Force curves were recorded with a maximum indentation of ~1 μm. Five low amplitude oscillatory cycles were also recorded in one of the three regions of the cell at an operating indentation of ~500 nm. The experimental protocol lasted ~45 min. Contact mode images were acquired after mechanical measurements in

three cells with the pyramidal tip at 1 Hz and force set point <0.5 nN.

4.4.6 Data processing

Each experimental $d - z$ curve obtained with the pyramidal tip was fitted with the blunted pyramid model (Eqs. 4.8 and 4.9) expressed in terms of the displacement of the piezo (z) and the deflection of the cantilever (d), using

$$F = k(d - d_{off}), \tag{4.11}$$

and

$$\delta = z - z_c - (d - d_{off}), \tag{4.12}$$

where k is the spring constant of the cantilever, d_{off} the deflection offset, and z_c the point of contact. Substituting Eqs. 4.11 and 4.12 into Eqs. 4.8 and 4.9 we obtained

$$\begin{aligned} d = d_{off} + \tfrac{2E}{k(1-\nu^2)} \Big[(z - z_c - (d - d_{off}))a - \tfrac{2^{1/2}a^2}{\pi \tan\theta} \left(\tfrac{\pi}{2} - \arcsin \tfrac{b}{a} \right) - \tfrac{a^3}{3R_c} + \\ + (a^2 - b^2)^{1/2} \left(\tfrac{2^{1/2}}{\pi} \tfrac{b}{\tan\theta} + \tfrac{a^2 - b^2}{3R_c} \right) \Big] \end{aligned} \tag{4.13}$$

$$z - z_c - (d - d_{off}) - \frac{a}{\tan\theta} \frac{2^{3/2}}{\pi} \left[\frac{\pi}{2} - \arcsin\left(\frac{b}{a}\right) \right] + \frac{a}{R_c} \left((a^2 - b^2)^{1/2} - a \right) = 0. \tag{4.14}$$

Since there is no analytical solution for Eq. 4.13, the radius of contact a was computed numerically using an interpolation routine.

Pyramidal tip data were also fitted with the ideal pyramidal tip model (Eq. 4.10) expressed in terms of z and d

$$d = d_{off} + \frac{1}{2^{1/2}} \frac{E \tan\theta}{(1 - \nu^2)k} [z - z_c - (d - d_{off})]^2. \tag{4.15}$$

The experimental $d - z$ curves obtained with the spherical tip were fitted with the spherical Hertz model (Eq. 4.5 of z and d

$$d = d_{off} + \frac{4E}{3(1 - \nu^2)k} R^{1/2} [z - z_c - (d - d_{off})]^{3/2}, \tag{4.16}$$

where R is tip radius. A nonlinear least squares fit (Matlab 6.5, The MathWorks Inc., Natick, MA, USA) was used to estimate E, z_c and d_{off} from each loading $d - z$ curve. The fit included a clear noncontact region. For cell measurements, the first micron of the

noncontact region was discarded. The average E for each sample was computed using the last three curves at the three measurement points. The mean and SD of these values were computed. To assess the dependence of E on indentation, contact model equations (Eqs. 4.13, 4.15 and 4.16) were solved for E. E was computed from each force-indentation measurement point, using the values of z_c and d_{off} fitted with the $d - z$ curve. E was computed at equally spaced indentation intervals by interpolation to allow averaging.

For low-amplitude oscillations around an operating indentation (δ_0), Eq. 4.8 can be approximated taking the first two terms of the Taylor expansion (Alcaraz et al., 2003; Mahaffy et al., 2000). Using $G = E/[2(1+\nu)]$ and transforming to the frequency domain, $G^*(\omega)$ for a blunted pyramidal tip is

$$G^*(\omega) = \frac{1-\nu}{4a_0}\frac{F(\omega)}{\delta(\omega)}, \tag{4.17}$$

where $F(\omega)$ and $\delta(\omega)$ are the Fourier transforms of force and indentation, respectively, ωgs the angular frequency ($\omega=2\pi f$) and a_0 is the contact radius at δ_0.

The same procedure was applied to obtain $G^*(\omega)$ for the spherical model (Eq.4.5)

$$G^*(\omega) = \frac{1-\nu}{4(R\delta_0)^{1/2}}\frac{F(\omega)}{\delta(\omega)}. \tag{4.18}$$

$G^*(\omega)$ was separated into its real (in-phase) and imaginary (out-of-phase) parts ($G^*(\omega)=G'(\omega)+iG''(\omega)$), defined as the storage and loss moduli, respectively. The viscoelastic behavior was characterized as the loss tangent (G''/G'). Before computing FFT, recordings were digitally filtered with a high-pass filter (Butterworth, 0.1 Hz, 5 poles), and multiplied by a Hanning window. Given the low oscillatory frequency applied (0.3 Hz) we neglected the hydrodynamic drag artifact (Alcaraz et al., 2002).

4.4.7 Statistics

Data are reported as mean ± SD unless otherwise stated. Differences in E and G^* values obtained using different tips were analyzed by Student's t-test. Statistical significance was assumed at $p < 0.05$.

4.5 Results

4.5.1 Cantilever tips

From the SEM images of the tips used in agarose (Fig. 4.2) we estimated a semi-included angle of θg 35.5 deg for the pyramidal tip and a bead radius of R= 2.4 μm for the spherical

tip. We estimated θg 35.4 deg and R = 2.5 μm for the tips used on A549 cells. The pyramidal tips exhibited a blunted apex (Fig. 4.2). We modeled the actual tip geometry using the blunted pyramid model (tip defect h= 100 nm) with the spherical cap merging tangential with the pyramid faces.

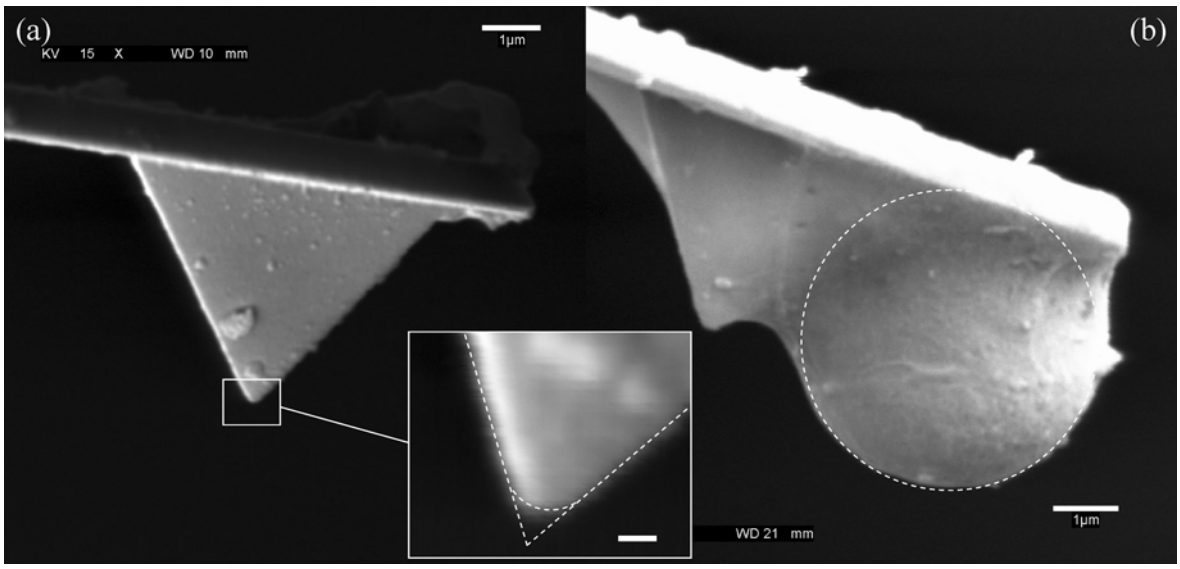

Figure 4.2: Scanning electron micrographs of pyramidal (a) and spherical (b) tips used in agarose gels (bar = 1 μm). The inset shows the blunted pyramidal approximation (bar = 100 nm).

4.5.2 Agarose gels

The pyramidal and spherical tip cantilevers used on agarose gels had spring constants of k = 7.1 ± 0.6 mN/m and k = 7.9 ± 0.6 mN/m, respectively. Representative examples of $d - z$curves taken on agarose are shown in Fig. 4.3. Loading and unloading curves were almost coincident. The fit of the model to the loading curve was excellent for both the pyramidal (r^2 = 0.9994 ± 0.0003, root mean square error (rms) = 4.46 ± 3.06 nm) and spherical (r^2 = 0.9991 ± 0.0002, rms = 2.55 ± 1.48 nm) tips. The residual error plot (Fig. 4.3) showed only minor deviations from the models. Nevertheless, the models slightly underestimated the force in the vicinity of the contact point.

The value of E computed with the pyramidal tip (1.38 ± 1.36 kPa) was larger than that computed with the spherical one (0.72 ± 0.60 kPa) (p>0.05). We found a small coefficient of variation (CoV) of E obtained from consecutive curves acquired at the same point of the gel with the pyramidal (3.9 ± 2.4%) and spherical (2.7 ± 1.8%) tips. Larger variability for the pyramid (10.9 ± 10.5%) and the sphere (13.6 ± 4.9%) were found from measurements taken at different points of the same gel.

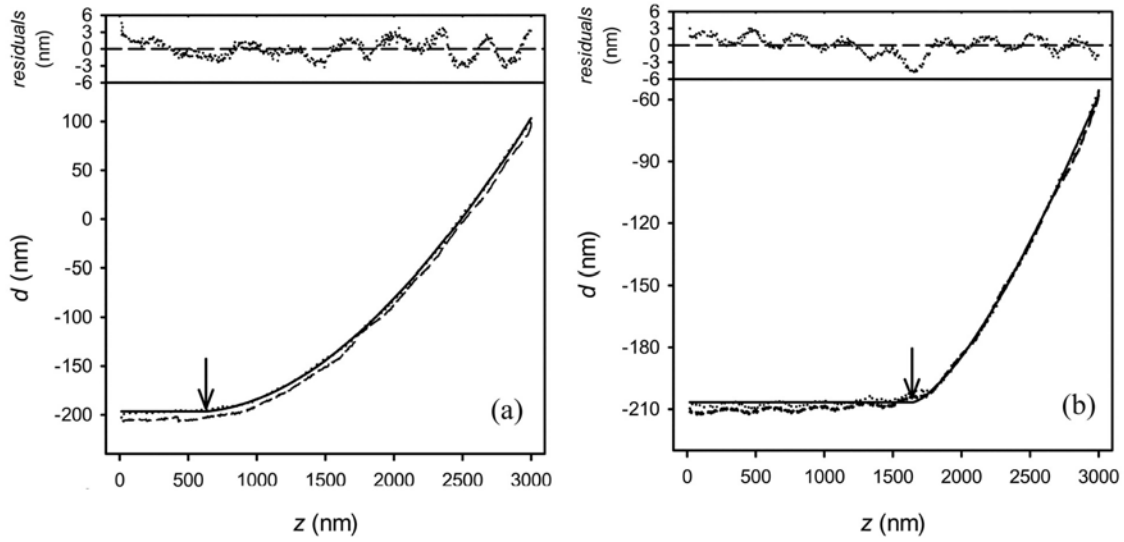

Figure 4.3: Examples of deflection-distance ($d - z$) curves measured on approach (dotted lines) and retraction (dashed lines) on agarose gels with pyramidal (a) and spherical (b) tips. Solid lines are the corresponding blunted pyramidal and spherical fits to approach curves. Fitted values were E = 0.76 kPa, z_c = 634 nm, and d_{off} = -196 nm, and E = 0.35 kPa, z_c = 1651 nm, and d_{off} = -207 nm, respectively. Arrows indicate the contact point. Insets display residual errors.

E computed from the spherical tip exhibited a sharp fall at low indentations reaching a plateau at ~200 nm (Fig. 4.4). A similar indentation dependence was obtained with a plateau above ~300 nm with the pyramidal tip using the blunted model (Eqs. 4.13 and 4.14). When employing the ideal pyramidal model (Eq. 4.15) the plateau was shifted to slightly higher indentations (~400 nm).

$G^*(\omega)$ was measured at comparable operating indentations of 563 ± 92 nm and 475 ± 134 nm for the pyramidal and spherical tips, respectively. The corresponding radii of contact were considerably smaller with the pyramid (0.33 ± 0.05 μm) than with the sphere (1.06±0.15 μm). G' was significantly higher when using the pyramidal tip (0.43 ± 0.20 kPa) than the spherical one (0.17 ± 0.05 kPa) (p <0.05). By contrast, we found negligible values of G" for both tips (0.02 ± 0.05 kPa, pyramid; –0.01 ± 0.02 kPa, sphere).

4.5.3 Alveolar epithelial cells

The cantilevers used on A549 cells had spring constants of k = 6.3 ± 0.4 mN/m and k= 7.9 ± 0.6 mN/m for the pyramidal and spherical tips, respectively. The thickness of the cells in the probed regions was 5-6 μm (Fig. 4.5). The $d - z$ curves of the cells exhibited considerable hysteresis (Fig. 4.5). We frequently observed deflection values below d_{off} in the unloading curves, indicating cell-tip adhesion. The contact models fitted loading

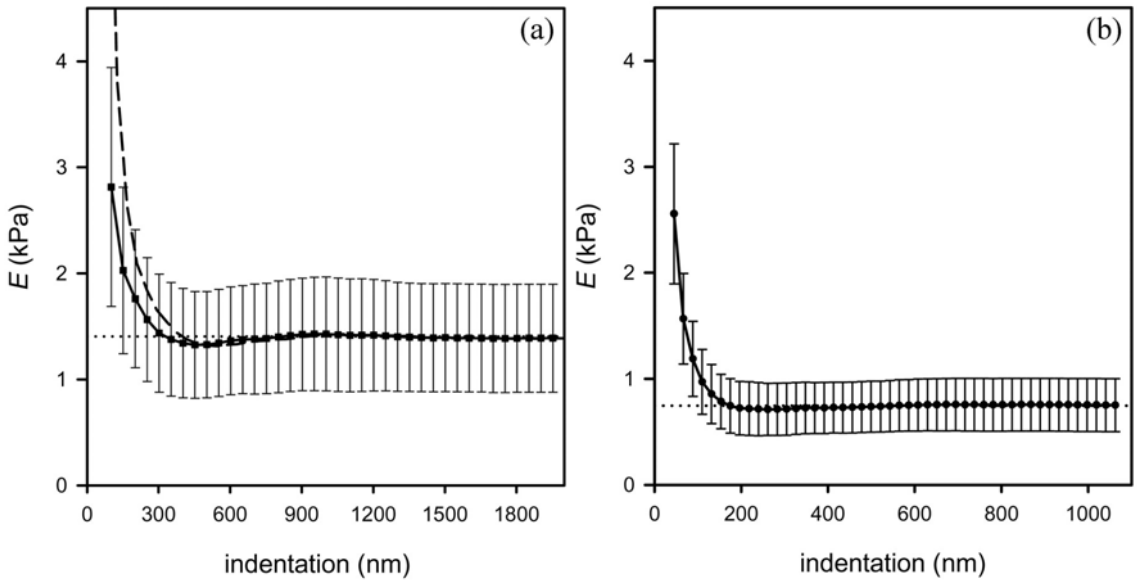

Figure 4.4: Indentation dependence (mean ± SE) of Young's modulus of agarose gels (n = 7) obtained with the pyramidal (a) and spherical (b) tips. Dashed line in (a) displays data fitted with the ideal pyramid model. Dotted lines are mean E values obtained by fitting the whole $d - z$ curves.

$d - z$ curves very well for the pyramidal (Eqs. 4.13 and 4.14, r^2 = 0.994 ± 0.005, rms = 2.91 ± 1.92 nm) and spherical (Eq. 4.16, r^2= 0.998 ± 0.001, rms = 1.63 ± 0.54 nm) tips. We obtained higher values of E with pyramidal (0.91 ± 0.47 kPa) than with the spherical tip data (0.47 ± 0.18 kPa) (p <0.05). Repeated measurements obtained at the same point of the cell led to similar CoV for the pyramid (5.3 ± 3.8%) and the sphere (3.1 ± 2.8%). By contrast, the variability computed from different regions within the same cell rose to 41.9 ± 21.5% (pyramid) and to 25.9 ± 22.7% (sphere). Young's modulus of cells showed an indentation dependence similar to that of gels (Fig. 4.6), reaching the plateau at comparable indentation depths.

$G^*(\omega)$ was measured at operating indentations of 716 ± 255 nm (a= 0.41 ± 0.13 μm) with the pyramid and 541 ± 225 nm (a= 1.13 ± 0.29 μm) with the sphere. With the pyramidal tip we found G' = 0.32 ± 0.16 kPa and G'' = 0.07 ± 0.03 kPa, corresponding to a loss tangent of 0.23 ± 0.12. Lower values of G' = 0.15 ± 0.07 kPa (p <0.05) and G'' = 0.03 ± 0.02 kPa (p <0.05) were obtained with the spherical tip although no significant difference was found in the loss tangent (0.21 ± 0.07).

4.6 Discussion

We have developed a contact model to describe the force-indentation relationship of a blunted pyramid indenting an elastic half-space. The model was extended for applica-

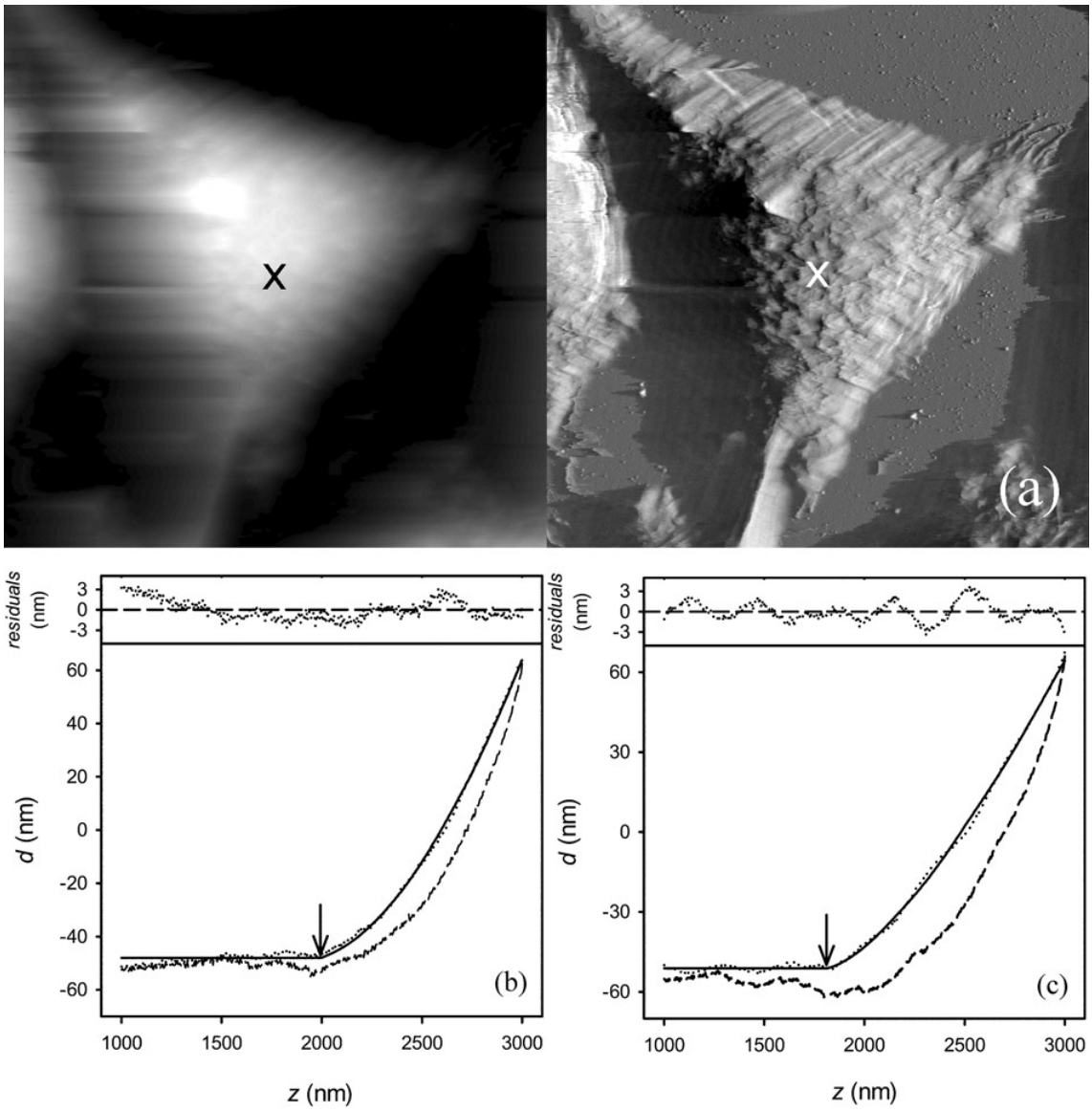

Figure 4.5: (a) Height (left) and deflection (right) images of an A549 cell obtained with the pyramidal tip in contact mode (scan size = 50 μm). Gray level ranges 6 μm (left) and 50 nm (right). (b and c) Examples of deflection-distance ($d - z$) curves measured on approach (dotted lines) and retraction (dashed lines) on the cell with pyramidal (b) and spherical (c) tips. Fitted values were E = 1.31 kPa, z_c = 1997 nm, and d_{off} = -49 nm, and E = 0.36 kPa, z_c = 1812 nm, and d_{off} = -51 nm, respectively. Arrows indicate the contact point. Insets display residual errors. The crosses in the images indicate the point where the pyramidal force curve was obtained.

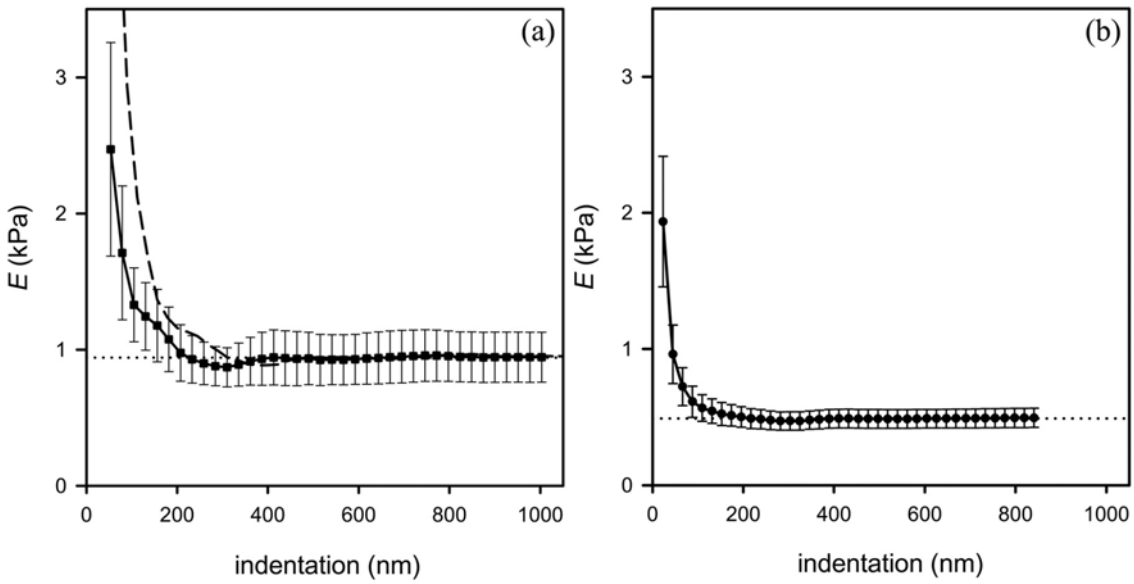

Figure 4.6: Indentation dependence (mean ± SE) of Young's modulus of alveolar epithelial cells (n = 7) obtained with the pyramidal (a) and spherical (b) tips. Dashed line in (a) displays data fitted with the ideal pyramid model. Dotted lines are mean E values obtained by fitting the whole $d - z$ curves.

tion to viscoelastic samples subjected to small amplitude oscillations. Soft agarose gels probed with AFM blunted pyramidal tips showed a fall in E at low indentations reaching a constant value for depths larger than ~300 nm. A similar indentation dependence of E was observed when the gels were probed with the spherical tip. Nevertheless, E and G' measured at deep indentations with the sphere were twofold lower than those found with the pyramid. The gels exhibited an elastic behavior with almost coincident loading and unloading force curves and negligible values of G". The dependence of E on indentation in cells paralleled that found in the gels. Cells exhibited viscoelastic behavior with a G"/G' ratio ~1/4.

The mathematical approach used to develop the blunted pyramidal model was based on Betti's reciprocal theorem and the Rayleigh-Ritz approximation (Ugural and Fenster, 1987). The Betti reciprocal theorem allowed us to relate the total force applied by the pyramidal tip to the pressure distribution of a flat tip with the same contact area (Eq. 4.1). Since this equation cannot be solved analytically, we made use of the Rayleigh-Ritz approach determining the best elliptical approximation to the actual contact area. This approximation is useful when the main interest is to compute $F(\delta)$ and not the pressure distribution, which requires a more complex mathematical development. Barber and Billings used this procedure to obtain $F(\delta)$ of an ideal three-sided pyramidal tip (Barber and Billings, 1990). Their solution differed only by 13% when compared with numerical computations. Given that the intervals of integration decrease with the number of sides,

a lower error for a four-sided pyramid was estimated. In fact, the solution we found for an ideal four-sided pyramid (Eq. 4.10) agrees within 6% with the equation derived by Bilodeau based on the stress distribution of a cone modified by the singularities at the lateral edges of the pyramid (Bilodeau, 1992). By imposing a smooth transition from the spherical cap to the pyramid faces, the faces must be slightly curved near the cap. This curvature leads to a smaller cross-sectional area compared with that of flat faces (Fig. 4.1). At an indentation of ~300 nm (θg 35 deg, R_c = 100 nm) the difference between flat and curved surfaces is ~8% and tends to zero at deeper indentations. Assuming that the force is proportional to the area, we estimate a similar difference in E. The blunted pyramidal model matches the spherical model with a radius equal to that of the spherical cap ($R = R_c$) for indentations where the sample only contacts the spherical cap ($\delta < 2h^*$), and at deeper indentations, the blunted pyramidal model approaches the ideal pyramidal model smoothly (Fig. 4.7). Note that the n-sided blunted pyramidal model (Eq. 4.6 and 4.7) is easily solvable for the variety of pyramidal geometries commercially available. The semi-included angle measured by SEM was in very good agreement with its nominal value (35 deg). This was expected from the stability of the fabrication process (Albrecht et al., 1990) and suggests that the nominal θ could be used to compute the blunted pyramidal model. However, the radius of the spherical cap measured by SEM (R_c = 123 nm) was 2-fold larger than its nominal value (~50 nm). Using the nominal radius would overestimate E by ~65 % for low indentations ($\delta < 2h^*$). The difference would tend to zero for deeper indentations, being <1% for $\delta > 1$ μm. Thus, accurate measurements at low indentations with a blunted pyramidal tip would require precise characterization of tip bluntness. It should be also pointed out that the solution for a n-sided blunted pyramid (Eq. 4.6 and 4.7) tends to that of a blunted cone when $n \rightarrow \infty$ (Briscoe et al., 1994). When, in addition, $b \rightarrow 0$ the solution corresponds to that of an ideal cone (Sneddon, 1965).

AFM systems tilt the cantilever by 10 – 20 degree so that the beams of the cantilever do not touch the sample. Heim and coworkers studied the contribution of the inclination angle (β) to the deflection of the cantilever and suggested a correction factor (Heim et al., 2004). Given the cantilever and tip dimensions we used (320 μm cantilever length, 4-5 μm tip height and 12 deg tilt), Heim's correction factors were < 0.5% for both spherical and pyramidal tips and were thus neglected. Moreover, current contact models assume normal indentation of the tip on the sample surface. Costa and Yin (Costa and Yin, 1999) discussed the effect of tip inclination on $F(\delta)$ for an ideal cone. They suggested that $F(\delta)$ of a tilted conical tip lies between the responses for semi-included angles $\theta+\beta$ and $\theta-\beta$. The force of a regular pyramid in normal indentation is the addition of the force applied to each face. We assume that the total force of a tilted pyramid is composed by the contributions

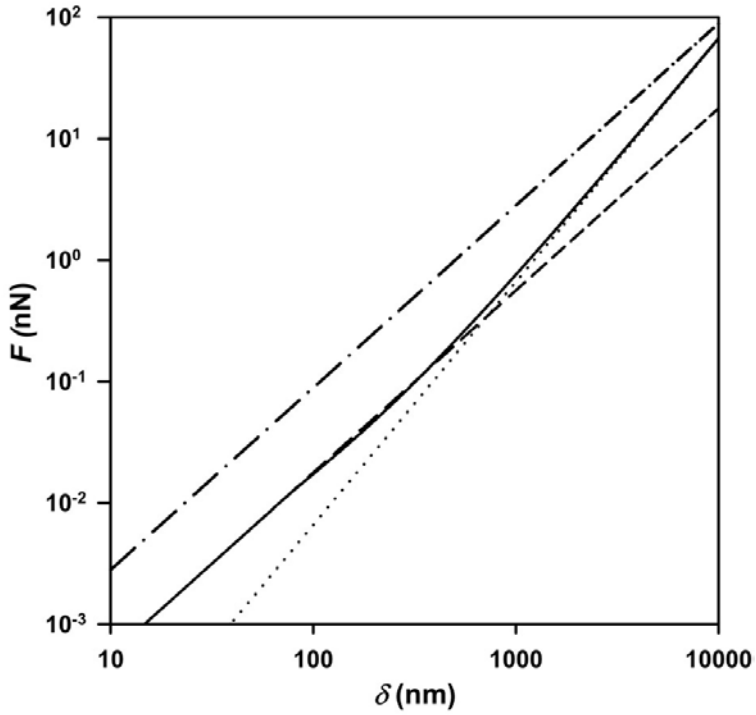

Figure 4.7: Force-indentation (F-δ) relationship for blunted pyramidal, ideal pyramidal and spherical models on an elastic half space with Young's modulus E = 1 kPa. Solid line is the blunted pyramidal model with semi-included angle θ = 35 deg and a spherical cap of radius R_c = 100 nm merging tangential with the faces. Dotted line is the ideal pyramidal model with θ = 35 deg (slope = 2). Dashed line is the spherical model of radius R = 100 nm (slope = 3/2). Dash-dotted line is the spherical model with R = 2500 nm (slope = 3/2). The blunted pyramidal model matches the spherical model of R = 100 nm ($R_c = R$) for indentations smaller than 80 nm ($\delta < 2h^*$) and approaches the ideal pyramidal model for deeper indentations. The difference is <15 % for indentations deeper than 1000 nm.

of each face, weighted by the areas of their cross-sections. In addition, we consider that each face of the tilted pyramid follows $F(\delta)$ of an ideal pyramid (Eq. 4.10) with semi-included angle $\theta \pm \beta$ (faces parallel to the inclination axis) or θgfaces perpendicular to the inclination axis). From this approach, we estimate an apparent increase in E of ~10% when tilting an ideal four-sided pyramid (θ = 35 deg) by 12 degree (for a more detailed development, see Appendix A). Assuming a similar behavior for the blunted pyramidal model, our measurements taken with the tilted pyramidal tip overestimated E by ~10%.

Reliable estimation of mechanical parameters from $d - z$ curves requires accurate determination of the contact point (Mahaffy et al., 2000; A-Hassan et al., 1998; Touhami et al., 2003). In general, the contact point is visually defined at the point where cantilever deflection starts to rise. However, visual determination of the contact point is especially difficult in soft samples which exhibit a smooth increase in cantilever deflection at low

indentations (Figs. 4.3 and 4.5). To define the contact point with an objective procedure, we simultaneously estimated E and the location of the contact point (z_c, d_{off}) by fitting $d - z$ curves which included a noncontact region. The fitting was carried out in the approaching curve to avoid the adhesion events observed in the retraction curves, especially in cells (Fig. 4.5). The quality of the fit with the two tips was excellent in gels and cells. It should be noted, however, that both models slightly underestimated cantilever deflection in the vicinity of the contact point (Figs. 4.3 and 4.5).

We first assessed the suitability of AFM pyramidal tips for probing mechanics in soft agarose gels. We used agarose gels as a reference sample since different techniques have shown that their mechanical properties are elastic, linear, homogeneous and isotropic (Stolz et al., 2004; Normand et al., 2000). Moreover, we made the gel samples ~500 μm thick to avoid the effect of the hard substrate. These features are required to fulfill the assumptions used to derive tip contact models. The high repeatability of E computed from consecutive curves recorded at the same point (CoV < 4%) indicates stability of the sample and absence of permanent deformation. The homogeneity of the gel was reflected in the low variation of E among different points of the sample (CoV < 10%). The near coincidence of the approach and retract $d - z$ curves confirmed the elastic behavior of our gel samples. Measurement of the complex shear modulus allows us to assess the frequency domain expansion of the blunted model (Eq. 4.17). In agreement with the elastic behavior, we found negligible values of G". Moreover, the E/G' ratio obtained for the pyramidal tip (3.21) was similar to that of a pure elastic material (E/G' = 3, ν = 0.5). The consistency between G^* and E lends support to the validity of the complex expansion of the blunted pyramidal model (Eq. 4.17). Taking into account the discrepancies between micro- and macro-rheological measurements (Schmidt et al., 2000), our data of G' compare well with the value of 0.52 kPa derived by Normand and coworkers (Normand et al., 2000) from conventional macroscopic rheology measurements on the same type of agarose at 0.3%. The value of E obtained by fitting the whole $d - z$ curves recorded with the pyramidal tip was twofold higher than that computed with the spherical tip. This difference could reflect uncertainties of the calibration procedure of the cantilevers, which assumes a simple harmonic oscillator model for cantilever mechanics. Nevertheless, E and G^* obtained with the two tips are in reasonable agreement bearing in mind that the difference is comparable to the variability of the gel samples.

To test the range of validity of the blunted pyramidal model we computed the indentation dependence of E in agarose gels (Fig. 4.4). For a linear material, E should be constant over the whole indentation range. Except at low indentations (< 300 nm), E computed with the blunted pyramidal tip showed a plateau up to the deepest indentation

reached (~2 μm). It is noteworthy that fitting the ideal pyramid model also results in the same plateau but slightly shifted to deeper indentations. Therefore, for deep indentations E can be more easily estimated by using Eq. 4.10. It has been suggested that the linear assumption of the Hertz theory fails for the large strains produced by pyramidal tips (Dimitriadis et al., 2002). To minimize strain it has been proposed to probe the sample with a microsphere (Mahaffy et al., 2000; Dimitriadis et al., 2002; Mahaffy et al., 2004). The plateau obtained when probing gels and polymers with a microsphere attached to the cantilever has been taken as evidence of the validity of the spherical contact model (Mahaffy et al., 2000). We found that the pyramidal tip exhibited a constant regime similar to that observed with the spherical tip. The linear regime displayed by the pyramidal tip is in agreement with finite element analysis indicating that high strains applied by sharp tips have only second order effects on the indentation response for linear materials (Costa and Yin, 1999). Moreover, it should be noted that the blunted profile of conventional AFM pyramidal tips reduces the strain in the vicinity of the apex.

Agarose gels exhibited a parallel fall in E at low indentations with both tips. This behavior has been reported in gels and living cells. Large and scattered values of E at low indentations have been attributed to experimental noise, to nonlinear elastic behavior of the samples (Mathur et al., 2001), and to uncertainties in the contact point determination (Mahaffy et al., 2000; Dimitriadis et al., 2002; Mahaffy et al., 2004). However, we averaged data from several measurements (Fig. 4.4) to cancel out the effect of random experimental noise. Moreover, the plateau of E obtained in a wide range of indentations with both tips indicates intrinsic linear mechanical properties of the gel. E estimated at low indentations is very sensitive to uncertainties in the contact point. In fact, the large E we found at low indentations could be explained by an error of 1-2 nm in d_{off}. To avoid ambiguities associated with visual determination we computed the contact point by a robust fitting procedure. The slight but systematic underestimation of cantilever deflection by the two contact models in the vicinity of the contact point (Fig. 4.3) suggests that E at low indentations reflects features of tip-surface interaction. This underestimation of cantilever deflection can be interpreted as a repulsive force. Assuming that agarose and the tip are electrically neutral, a repulsive force could arise from steric interactions of free-end agarose chains forming brush-like arrangements in the gel-liquid interface (Butt et al., 1999). The similar fall of E at low indentations and the deeper linear regime exhibited by the pyramidal and spherical tips on the agarose gels suggest that both cantilevers are suitable for probing the mechanical properties of uniform and thick soft samples.

The performance of the tips in cells was in agreement with that observed in gels. Both tips displayed large values of E at low indentations followed by a sharp fall reaching a

plateau at ~200 nm which extended to the deepest indentation obtained. Similar indentation dependence has been reported in other cells types (Mathur et al., 2001; Mahaffy et al., 2000, 2004). In accordance with the results found in gels, the plateau value of E estimated with the two tips differed by a factor of ~2. The constant E observed over a broad indentation range indicates a fairly linear behavior of cell mechanics. However, the sharp rise of E at low indentions deviated from the linear behavior. This surface singularity may reflect the effect of steric forces associated with the brush-like glycocalix of living cells (Fritz et al., 1994; Lee and Marchant, 2000). The repeatability of consecutive measurements at the same point taken with both tips (~5%) was as good as in the gels. On the other hand, the larger variability among cell regions reflected a more heterogeneous mechanical behavior of the cells. Moreover, the higher heterogeneity observed with the pyramidal tip reflects improved lateral resolution. In contrast to the near elastic behavior of agarose gels, the cells exhibited viscoelastic properties with the oscillatory response dominated by elastic stresses. Similar viscoelastic behavior has also been observed in the same cell type twisting magnetic beads attached to the cell surface (Trepat et al., 2004). Despite the higher values of the storage and loss moduli measured with the pyramidal tip, their ratio (G"/G' = 0.23 ± 0.12) was almost coincident with that obtained with the spherical tip (0.21 ± 0.07). This indicates that both tips differed only in a scale factor. The agreement between the G"/G' ratio obtained with both tips lends further support to the complex expansion of the blunted pyramidal model (Eq. 4.17).

The use of a pyramidal tip allows us to obtain high resolution images of the cell and to measure cell mechanics with the same probe. The resolution of the images enables us to observe cell topography in detail and to identify cytoskeleton fibers and other submembrane structures (Fig. 4.5). A recent work compared the image resolution obtained with pyramidal and spherical tips on porcine articular cartilage (Stolz et al., 2004). Individual collagen fibers observed with pyramidal tips were not resolved with microspheres, reflecting, thus, the poor image resolution of such tips. The linear regime of cell mechanics was clearly reached with the pyramidal tip for indentations of ~300 nm. The effective contact radius of the pyramidal tip at this indentation was ~200 nm, which provides an estimation of the lateral resolution of the mechanical measurements. The use of a single cantilever for imaging and mechanics is an important advantage, which provides precise correlation between viscoelastic mapping and cell structure. We probed the cells at points of 5-6 μm thickness reaching indentations up to ~1 μm. We did not observe hardening effects due to the underlying hard substrate, indicating that the contact model can be reliably applied for indentations up to ~20 % of cell thickness. Consequently, the pyramidal tip can probe cell mechanics with indentations up to 300 nm for cell thickness >1.5 μm. This condition

is maintained over a large region of the cell body of the lung epithelial cells. However, measurements at the thin cell periphery would require correction for the influence of the hard substrate (Dimitriadis et al., 2002; Mahaffy et al., 2004).

In conclusion, we developed a contact model of a blunted pyramidal tip to compute viscoelastic properties of soft samples indented with conventional AFM pyramidal tips. Agarose gels and living cells probed with a blunted pyramidal tip exhibited elastic behavior with large values of Young's modulus for indentations lower than ~300 nm and a linear regime at deeper indentations. This indentation dependence paralleled that obtained with spherical tips, indicating that the larger strains applied by the pyramidal tip at the apex have minor effects on the force-indentation response. However, Young's modulus computed in the linear regime with the two tips differs by a factor of ~2. Cells exhibited viscoelastic behavior with almost coincident values of the loss tangent obtained with both tips. Cells displayed a linear regime for indentations up to ~20% of cell thickness. This allows probing viscoelasticity with the pyramidal tip in a broad central region of the cell body with negligible influence of the hard substrate. Our results suggest that pyramidal tips commonly used for AFM imaging are suitable for probing mechanical properties of soft polymer gels and living cells. The use of a single cantilever enables us to precisely correlate imaging and viscoelastic mapping of living cells.

Bibliography

E. A-Hassan, W. Heinz, M. D. Antonik, N. P. D'Costa, S. Nageswaran, C. A. Schoenenberger, and J. H. Hoh. Relative microelastic mapping of living cells by atomic force microscopy. *Biophys.J.*, 74:1564–1578, 1998.

T. R. Albrecht, S. Akamine, T. E. Carver, and C. F. Quate. Microfabrication of cantilever styli for the atomic force microscope. *J.Vac.Sci.Technol.A*, 8(4):3386–3396, 1990.

J. Alcaraz, L. Buscemi, M. Puig de Morales, J. Colchero, A. Baro, and D. Navajas. Correction of microrheological measurements of soft samples with atomic force microscopy for the hydrodynamic drag on the cantilever. *Langmuir*, 18(3):716–721, 2002.

J. Alcaraz, L. Buscemi, M. Grabulosa, X. Trepat, B. Fabry, R. Farre, and D. Navajas. Microrheology of human lung epithelial cells measured by atomic force microscopy. *Biophys.J.*, 84:2071–2079, 2003.

J. R. Barber and D. A. Billings. An approximate solution for the contact area and elastic compliance of a smooth punch of arbitrary shape. *Int.J.Mech.Sci.*, 32(12):991–997, 1990.

G. Bilodeau. Regular pyramid punch problem. *J.Appl.Mech.-Trans.ASME*, 59:519–523, 1992.

B. J. Briscoe, K. S. Sebastian, and M. J. Adams. The effect of indenter geometry on the elastic response to indentation. *J.Phys.D: Appl.Phys.*, 27:1156–1162, 1994.

H. J. Butt, M. Kappl, H. Mueller, R. Raiteri, W. Meyer, and J. Ruhe. Steric forces measured with the atomic force microscope at various temperatures. *Langmuir*, 15(7): 2559–2565, 1999.

G. T. Charras and M. A. Horton. Single cell mechanotransduction and its modulation analyzed by atomic force microscope indentation. *Biophys.J.*, 82(6):2970–2981, 2002.

K. D. Costa and F. C. P. Yin. Analysis of indentation: implications for measuring mechanical properties with atomic force microscopy. *J.Biomech.Eng.*, 121:462–471, 1999.

E. K. Dimitriadis, F. Horkay, J. Maresca, B. Kachar, and R. S. Chadwick. Determination of elastic moduli of thin layers of soft material using the atomic force microscope. *Biophys.J.*, 82:2798–2810, 2002.

M. Fritz, M. Radmacher, and H. E. Gaub. Granula motion and membrane spreading during activation of human platelets imaged by atomic force microscopy. *Biophys.J.*, 66(5):1328–1334, 1994.

S. R. Heidemann and D. Wirtz. Towards a regional approach to cell mechanics. *Trends Cell Biol.*, 14(4):160–166, 2004.

L. O. Heim, M. Kappl, and H. J. Butt. Tilt of atomic force microscope cantilevers: Effect on spring constant and adhesion measurements. *Langmuir*, 20(7):2760–2764, 2004.

E. Henderson, P. G. Haydon, and D. S. Sakaguchi. Actin filament dynamics in living glial cells imaged by atomic force microscopy. *Science*, 257(5078):1944–1946, 1992.

H. Hertz. On the contact of elastic bodies. In *Hertz's Miscellaneous Papers*, Miscellaneous Papers, chapter 5, pages 146–162. Macmillan, London, 1881.

M. Heuberger, G. Dietler, and L. Schlapbach. Elastic deformations of tip and sample during atomic force microscope measurements. *J.Vac.Sci.Technol.B*, 14(2):1250–1254, 1996.

Hayden Huang, Roger D. Kamm, and Richard T. Lee. Cell mechanics and mechanotransduction: pathways, probes, and physiology. *Am.J.Physiol.-Cell Physiol.*, 287(1): C1–11, 2004.

J. L. Hutter and J. Bechhoefer. Calibration of atomic-force microscope tips. *Rev.Sci.Instr.*, 64(7):1868–1873, 1993.

K. L. Johnson. *Contact Mechanics*. Cambridge University Press, Cambridge, 1985.

R. Lal, B. Drake, D. Blumberg, D. R. Saner, P. K. Hansma, and S. C. Feinstein. Imaging real-time neurite outgrowth and cytoskeletal reorganization with an atomic force microscope. *Am.J.Physiol.-Cell Physiol.*, 269(1 Pt 1):C275–C285, 1995.

I. Lee and R. E. Marchant. Force measurements on platelet surfaces with high spatial resolution under physiological conditions. *Colloid Surf.B-Biointerfaces*, 19(4):357–365, 2000.

R. E. Mahaffy, C. K. Shih, F. C. MacKintosh, and J. Kas. Scanning probe-based frequency-dependent microrheology of polymer gels and biological cells. *Phys.Rev.Lett.*, 85:880–883, 2000.

R. E. Mahaffy, S. Park, E. Gerde, J. Kas, and C. K. Shih. Quantitative analysis of the viscoelastic properties of thin regions of fibroblasts using atomic force microscopy. *Biophys.J.*, 86(3):1777–1793, 2004.

Anshu B. Mathur, Amy M. Collinsworth, William M. Reichert, William E. Kraus, and George A. Truskey. Endothelial, cardiac muscle and skeletal muscle exhibit different viscous and elastic properties as determined by atomic force microscopy. *J.Biomech.*, 34(12):1545–1553, 2001.

V. Normand, D. L. Lootens, E. Amici, K. P. Plucknett, and P. Aymard. New insight into agarose gel mechanical properties. *Biomacromolecules*, 1(4):730–738, 2000.

M. Radmacher, R. W. Tilmann, and H. E. Gaub. Imaging viscoelasticity by force modulation with the atomic force microscope. *Biophys.J.*, 64(3):735–742, 1993.

M. Radmacher, M. Fritz, and P. K. Hansma. Imaging soft samples with the atomic force microscope: gelatin in water and propanol. *Biophys.J.*, 69(1):264–270, 1995.

C. Rotsch and M. Radmacher. Drug-induced changes of cytoskeletal structure and mechanics in fibroblasts: an atomic force microscopy study. *Biophys.J.*, 78:520–535, 2000.

F. G. Schmidt, B. Hinner, and E. Sackmann. Microrheometry underestimates the values of the viscoelastic moduli in measurements on f-actin solutions compared to macrorheometry. *Phys.Rev.E*, 61(5):5646–5653, 2000.

B. Shoelson, E. K. Dimitriadis, H. X. Cai, B. Kachar, and R. S. Chadwick. Evidence and implications of inhomogeneity in tectorial membrane elasticity. *Biophys.J.*, 87(4): 2768–2777, 2004.

S. G. Shroff, D. R. Saner, and R. Lal. Dynamic micromechanical properties of cultured rat atrial myocytes measured by atomic-force microscopy. *Am.J.Physiol.-Cell Physiol.*, 38(1):C286–C292, 1995.

I. N. Sneddon. The relaxation between load and penetration in the axisymmetric boussinesq problem for a punch of arbitrary profile. *Int.J.Engng.Sci.*, 3:47–57, 1965.

Robert W. Stark, Tanja Drobek, and Wolfgang M. Heckl. Thermomechanical noise of a free v-shaped cantilever for atomic-force microscopy. *Ultramicroscopy*, 86(1-2):207–215, 2001.

M. Stolz, R. Raiteri, A. U. Daniels, M. R. VanLandingham, W. Baschong, and U. Aebi. Dynamic elastic modulus of porcine articular cartilage determined at two different levels of tissue organization by indentation-type atomic force microscopy. *Biophys.J.*, 86 (5):3269–3283, 2004.

M. Tortonese. Cantilevers and tips for atomic force microscopy. *IEEE Eng.Med.Biol.Mag.*, 16(2):28–33, 1997.

A. Touhami, B. Nysten, and Y. F. Dufrene. Nanoscale mapping of the elasticity of microbial cells by atomic force microscopy. *Langmuir*, 19(11):4539–4543, 2003.

X. Trepat, M. Grabulosa, F. Puig, G. N. Maksym, D. Navajas, and R. Farre. Viscoelasticity of human alveolar epithelial cells subjected to stretch. *Am.J.Physiol.-Lung Cell.Mol.Physiol.*, 2004.

A. C. Ugural and S. K. Fenster. *Advanced Strength and Applied Elasticity*. Elsevier Science Publishing Co., Inc., New York, 1987.

H. W. Wu, T. Kuhn, and V. T. Moy. Mechanical properties of l929 cells measured by atomic force microscopy: Effects of anticytoskeletal drugs and membrane crosslinking. *Scanning*, 20(5):389–397, 1998.

H. X. You and L. Yu. Atomic force microscopy imaging of living cells: progress, problems and prospects. *Methods in Cell Science*, 21:1–17, 1999.

H. X. You, J. M. Lau, S. Zhang, and L. Yu. Atomic force microscopy imaging of living cells: a preliminary study of the disruptive effect of the cantilever tip on cell morphology. *Ultramicroscopy*, 82(1-4):297–305, 2000.

Chapter 5

Validation of cylindrical cantilever tips for probing mechanical properties of biopolymers by AFM

5.1 Introduction

Atomic force microscopy is widely used as a nanoindenter to probe the mechanical properties of soft biological samples (Alcaraz et al., 2003). The common tips of commercially available AFM cantilevers have pyramidal, conical, or spherical shapes. Such tip geometries lead to an increasing contact area as the tip indents the sample, resulting in a nonlinear force-indentation relationship ($F(\delta)$). A reliable estimation of mechanical parameters depends on the suitability of the applied contact model and on the accurate determination of the point of contact (Mahaffy et al., 2000; A-Hassan et al., 1998; Mathur et al., 2001). This is especially difficult in soft biopolymers and living cells due to the low signal to noise ratio at low indentations. The use of a cantilever tip with flat ended cylindrical geometry minimizes this problems. Focused Ion Beam (FIB) technology with sub-micrometric resolution has been previously used to modify AFM cantilevers and their tips (Hodges et al., 2001; Obataya et al., 2005). The aim of this work was to validate cylindrical cantilever tips modified by FIB for probing mechanical properties of biopolymers by AFM.

5.2 Materials and methods

5.2.1 AFM

Experiments were carried out using a homemade AFM-based system mounted on the stage of an inverted optical microscope (Axiovert S100, Zeiss, Göttingen, Germany). The cantilever was positioned using a single axis piezoactuator (P.841.20, Physik Instrumente, Waldbronn, Germany) servocontrolled with a proportional-integral analog circuit. The deflection (d) of the cantilever was measured using the optical beam deflection method. The laser beam (62FCM, Schäfter + Kirchhoff, Hamburg, Germany) was focused at the backside of the cantilever, reflected off, and reached a four-segment photodiode (S4349, Hamamatsu, Hamamatsu city, Japan). The photodiode and position sensor (z) signals were low-pass filtered (Butterworth analog filter, 8 poles, 256 Hz), and sampled with a 16 bit data acquisition board (PCMIO- 16XE-10, National Instruments, Austin, TX) installed on a personal computer.

5.2.2 Gel samples

Purified agarose (Type I-A: Low EEO, A-0169, Sigma, St. Louis, MO, USA) 0.3% w/v in Millipore RX water was boiled for ~20 min stirring continuously or until agarose dissolved completely. The agarose solution was poured into a 35 mm diameter petri dish to obtain a gel thickness ~500 μm. A small region of the petri dish was left bare to allow calibration of the AFM photodiode. After gelation of the solution occured (~5 min), the sample was covered with 2 ml of Millipore RX water and stored at 4^{o}C. Gels had more stability when left overnight at 4^{o}C and measured the following day.

5.2.3 Cantilever tip modification

Silicon cantilevers (nominal spring constant k = 0.03 N/m, MikroMasch, Estonia) with pyramidal tips (15-20 μm height) were placed on the FIB (FEI Company, Hillsboro, USA) sample holder (Fig. 5.1). Tips were milled using a ring-like pattern (2 μ m inner diameter, 5 μm outer diameter) centered on the tip apex but tilted by an angle of 8^o with respect to the axis of the pyramid. This process was carried out by repetitive passes reducing progressively the outer diameter. The tip end was then removed by milling a straight line pattern perpendicular to the cylinder axis. SEM images were obtained after fabrication to determine the actual radii of the cylinders (a).[1]

[1]Tip modification was carried out by Pere Roca-Cusachs at Plataforma de Nanotecnologia of the Parc Científic de Barcelona.

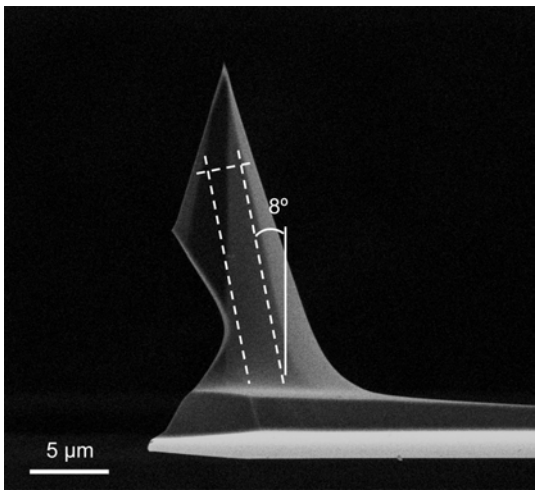

Figure 5.1: AFM silicon cantilever before being modified using FIB technology

5.2.4 Measurements

Measurements were carried out by recording three *d*-*z* curves (3 μm peak to peak, 0.3 Hz) at three different regions of five agarose gels. The indentation reached was ~1 μm.

5.2.5 Data processing

The force was obtained from cantilever deflection (d) by means of the Hooke's law ($F = kd$). Indentation was computed as $\delta = z - z_c - d + d_0$, being z_c the point of contact and d_0 the deflection offset. Samples were assumed to be incompressible (ν=0.5). E, z_c, d_{off} were estimated simultaneously using a non linear least squares algorithm (Matlab 7.0, The MathWorks Inc., Natick, MA, USA) to fit the whole loading part of *d*-*z* curves with the contact model of a flat-ended cylinder indenting an elastic half space (Johnson, 1985)

$$F = kd_0 + \frac{2E}{(1-\nu^2)}a\delta \tag{5.1}$$

expressed in terms of z and d. To analyse the dependency of E on indentation we used the fitted values of z_c and d_0 to compute the indentation. Therefore, E was isolated from Eq. 5.1 and recalculated for each indentation point.

5.3 Results

The resulting microfabricated tip was a flat-ended cylinder (~1.5 μm diameter, ~10 μm high) tilted ~8^o (Fig. 5.2). A representative example of a loading force curve with the corresponding fit of Eq. 5.1 is shown in Fig. 5.3. The $F - \delta$ relationship was fairly linear.

The residual error plot ((Fig. 5.3) showed only minor deviations from the model, systematically near the point of contact. The average quality of the fits was r^2=0.9989±0.0003 (mean±SD). The mean $E \pm SD$ value of agarose gels was 1.79 ± 1.09 kPa. The coefficient of variance (CoV) of E computed from consecutive force curves at a same point of a gel was 1.5 ± 1.1%. The CoV of E for different points inside a same gel was 27 ± 20%.

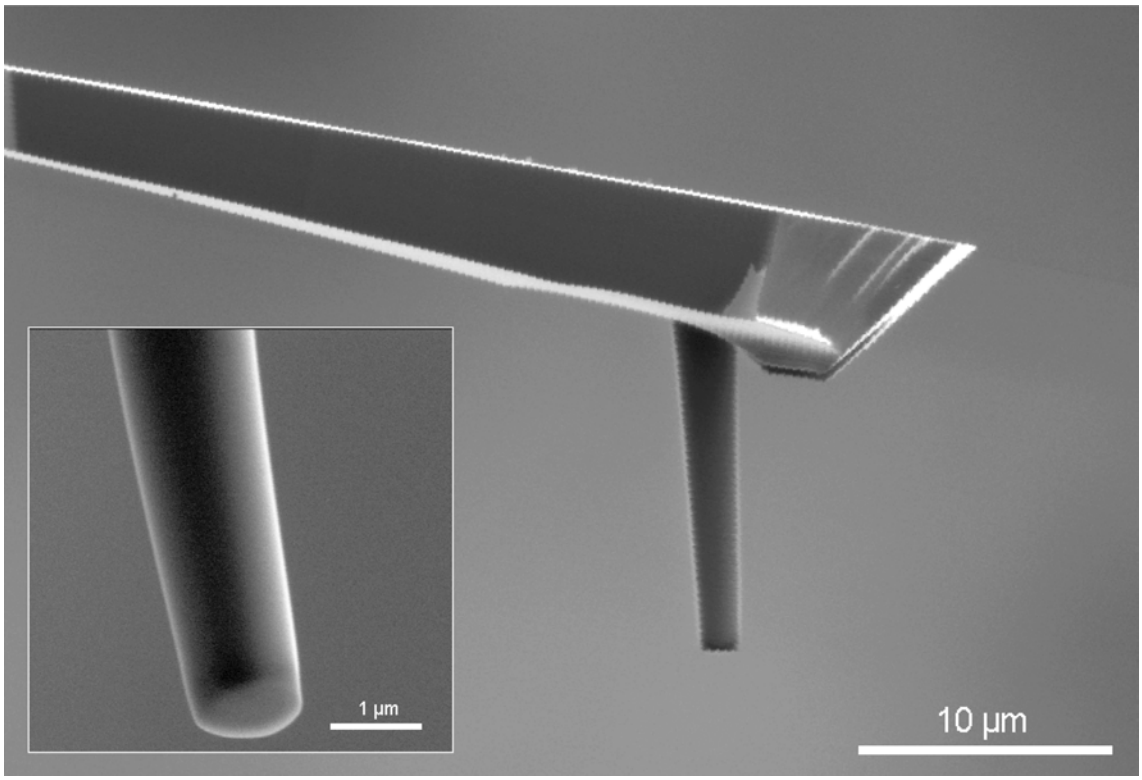

Figure 5.2: SEM image of a cylindrical tip before being used in the measurements. Inset: Detail of the cylindrical flat-end

5.4 Discussion

Flat-ended cylindrical cantilever tips with a diameter of ~1.5 μm and tilted by an angle of ~8º were validated on agarose gels. The $F - \delta$ relationship obtained was fairly linear. The indentation dependence of E followed a sharp fall reaching a plateau for indentations ~200 nm which extended until maximum indentation depths reached.

The modification of the cantilever tips was carried out by FIB. This technology has been successfully used to modify AFM cantilevers (Hodges et al., 2001; Obataya et al., 2005). Indeed, Obataya and co-workers modified AFM cantilever tips to obtain a needle-like shape of 200-300 nm diameter. They used these needles to penetrate inside human epidermal melanocytes and measure the elastic modulus of the nucleus. Among other

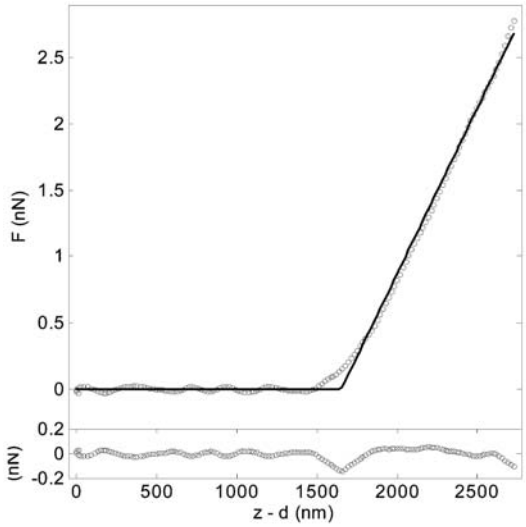

Figure 5.3: Representative example of a force-indentation $F - \delta$ loading curve (dots) with its fit (solid line). The residual errors are plotted below.

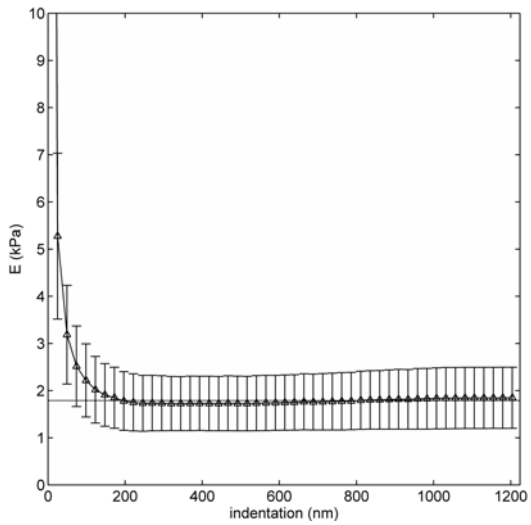

Figure 5.4: Dependency of E on δ (mean±SE). A plateau value is reached at indentations ~200 nm

causes, the accuracy of FIB technology is limited by instability or drift of ion and electron beams currents, by the pixel spacing, and by redepositioning of the sputtered target material. The ratio of the pixel spacing to the beam diameter was chosen in order of obtain a smooth and uniform flux profile. The other causes are reinforced when operating at high intensity of the beam and for long exposure times. Due to the big dimensions of our cylindrical tips we indeed used high intensities (5000 pA) and long dwell times (2 min). To reduce the resulting inaccuracy the milling process was carried out by using repetitive passes with dwell times of 100 ns (Tseng, 2004). The 2 μm inner diameter of the ring-like

milling pattern led to a cylinder diameter slightly smaller, in accordance with the deviation of 15% in similar patterns reported by Tseng. Nevertheless, this did not limit the applicability of the cylinders since a SEM image of each tip was acquired to measure its actual diameter. The purpose of the tilt was to overcome the inclination angle at which the chip is mounted on the AFM cantilever holder.

The contact model was fitted to the whole loading curve including contact and non contact regions. Using the non contact part minimizes the inaccuracy in the visual determination of the point of contact (chapter 4). The experimental force curve differed from the predicted linear behavior near the point of contact (Fig. 5.3). This divergence may be attributed to three main issues. First, the milling procedure lead to a lateral tilt of the flat-end of ±1-2^o. This uncertainty was due to the gaussian profile of the beam which leads to an overmilling of the silicon surface situated closer to the beam source. Supposing a similar uncertainty for the cantilever holder, we would expect ±4^o maximum deviation from normal indentation. Therefore, the tip may first contact the sample by the border of the flat-end circle. This may lead to an increasing contact area, *i.e.* non-linear force response, until the total flat-ended area made contact, from this point onwards, the response may be linear. The region of uncertainty due to a 4^o tilt for a cylinder of radius 1.5 μm might be of ~100 nm, leading to an indentation uncertainty of ~200 nm. Second, agarose gels at such low concentrations may have free-end fibers forming a brush-like interface between the gel and the fluid. Steric forces have been observed in brush-like structures formed by polymers grafted or adsorbed on hard surfaces (Butt et al., 1999). These steric forces may superimpose the purely elastic forces considered by the contact model and may contribute to the observed non linear response. Similar trends has been observed before using spherical and pyramidal cantilevers tips or with needle-shaped cantilever tips on biopolymers and living cells (Chapter 4 and Obataya et al. 2005; Lee and Marchant 2000). And third, the fabrication process of the tips led to a slight rounding of the flat-end edges. This roundness is inherent to FIB technology and can be reduced using low beam currents (Tseng, 2004). We estimated a radius of curvature of ~50 nm for the flat-end edges, which may also contribute to the nonlinear behavior near the contact point for indentations of similar depths.

The mean value of E had an indentation dependence in accordance with that obtained with other cantilever tips on biopolymers and living cells (see Mahaffy et al. 2000; Mathur et al. 2001 and Chapter 4). A sharp fall for low indentations preceded a plateau value (Fig. 5.4). A linear elastic material may have a constant value for the whole indentation range. The plateau was reached at indentations of ~200 nm, lending support to the applicability of the model used to describe the cylindrical tip. The high E values at low indentations

may be the reflect of steric forces and geometrical uncertainties mentioned above. The major advantage of cylindrical tips versus pyramidal or spherical tips was the possibility of maintaining a constant area of contact, obtaining a linear response. Thus, a nonlinear $F - \delta$ relationship may suggest nonlinearities of the probed material. This feature may be useful to study living cells under high strains, which are supposed to experience strain hardening (Stamenovic and Wang, 2000).

In summary, flat-ended cylindrical tips were validated on an linear, elastic sample. Cylindrical tips enable us to measure the mechanical properties of soft biological samples, such as polymer gels and living cells, with AFM maintaining a constant area of contact. A straightforward application of cylindrical tips may be their utilization in adhesion measurements where the number of adhesion bonds are required [2].

Bibliography

E. A-Hassan, W. Heinz, M. D. Antonik, N. P. D'Costa, S. Nageswaran, C. A. Schoenenberger, and J. H. Hoh. Relative microelastic mapping of living cells by atomic force microscopy. *Biophys.J.*, 74:1564–1578, 1998.

J. Alcaraz, L. Buscemi, M. Grabulosa, X. Trepat, B. Fabry, R. Farre, and D. Navajas. Microrheology of human lung epithelial cells measured by atomic force microscopy. *Biophys.J.*, 84:2071–2079, 2003.

H. J. Butt, M. Kappl, H. Mueller, R. Raiteri, W. Meyer, and J. Ruhe. Steric forces measured with the atomic force microscope at various temperatures. *Langmuir*, 15(7): 2559–2565, 1999.

A. R. Hodges, K. M. Bussmann, and J. H. Hoh. Improved atomic force microscope cantilever performance by ion beam modification. *Rev.Sci.Instr.*, 72(10):3880–3883, 2001.

K. L. Johnson. *Contact Mechanics*. Cambridge University Press, Cambridge, 1985.

I. Lee and R. E. Marchant. Force measurements on platelet surfaces with high spatial resolution under physiological conditions. *Colloid Surf.B-Biointerfaces*, 19(4):357–365, 2000.

R. E. Mahaffy, C. K. Shih, F. C. MacKintosh, and J. Kas. Scanning probe-based frequency-dependent microrheology of polymer gels and biological cells. *Phys.Rev.Lett.*, 85:880–883, 2000.

Anshu B. Mathur, Amy M. Collinsworth, William M. Reichert, William E. Kraus, and George A. Truskey. Endothelial, cardiac muscle and skeletal muscle exhibit different viscous and elastic properties as determined by atomic force microscopy. *J.Biomech.*, 34(12):1545–1553, 2001.

[2] This application will be discussed in detail in Chapter 6

I. Obataya, C. Nakamura, S. Han, N. Nakamura, and J. Miyake. Nanoscale operation of a living cell using an atomic force microscope with a nanoneedle. *Nano Letters*, 5(1): 27–30, 2005.

D. Stamenovic and N. Wang. Invited review: Engineering approaches to cytoskeletal mechanics. *J.Appl.Physiol.*, 89(5):2085–2090, 2000.

A. A. Tseng. Recent developments in micromilling using focused ion beam technology. *Journal of Micromechanics and Microengineering*, 14(4):R15–R34, 2004.

Chapter 6

Effect of thrombin on the adhesion properties of living alveolar epithelial cells measured by AFM

6.1 Introduction

The alveolar-capillary barrier is formed by a layer of epithelial cells laying on the basal membrane, which in turn serves as a base for the endothelial layer. The integrity of alveolar-capillary barrier is critical in the understanding of acute lung injury (Geiser, 2003; Ware and Matthay, 2000). Epithelial cells are involved in different functions including modulation of local inflammation, which is tightly regulated by integrins (Sheppard, 2003). A proposed explanation of the disruption of the a-c barrier is the breakage of the equilibrium of forces at which endothelial and epithelial cells are subjected (Dudek and Garcia, 2001; Trepat et al., 2005; Buscemi et al., 2003a,b). This equilibrium involves a balance between inward and outward (tensional and adhesive) forces. Tensional forces comprise those generated by activation of the actomyosin machinery of the cells, and those involved in spontaneous breathing or mechanical ventilation due to viscoelastic recoil. These tensional forces are directed in the inward or centripetal direction of the cell. Adhesion forces include those that tether cells to each other and to their extracellular matrix (Dudek and Garcia, 2001). It has been observed that inflammatory mediators activate the actomyosin machinery of endothelial cells inducing contraction, and the formation of intercellular gaps, leading to disruption of the endothelial barrier (Dudek and Garcia, 2001). Failure of the endothelial barrier permits the passage of vascular fluid, including secreted inflammatory mediators (*e.g.* thrombin), to the interstitial space reaching also the alveolar epithelium. There is controversy about how pro-inflammatory agents may

affect the integrity of the alveolar epithelium. In the one hand, Kawkitinarong and coworkers have recently proposed that thrombin induces enhancement of barrier integrity in the alveolar epithelium, due to remodelling of actomyosin cytoskeleton around cell periphery and enhancement of tight junction complexes (Kawkitinarong et al., 2004). They found an increase in transmonolayer electric resistance in alveolar epithelial monolayers after addition of thrombin, which has been interpreted as a decrease in monolayer permeability. In addition, they also found an increase in myosin light chain phosphorylation, which is usually associated to activation of the contractile machinery of living cells. On the other hand, a recent study shows that thrombin induced an increase in endothelial permeability in intact rabbit lungs, as revealed by capillary filtration measurements (Vadasz et al., 2005). In addition, it has been shown that inflammatory mediators, thrombin and histamine, induce stiffening of alveolar epithelial cells (Trepat et al., 2005; Buscemi et al., 2003a,b). Cellular stiffness has been shown to be related with activation of the contractile apparatus in a number of cell types (Fabry et al., 2001; de Morales et al., 2004; Smith et al., 2005; Trache et al., 2005). Stiffness induced by thrombin has been proposed as a mechanism for the disruption of the alveolar epithelium since cell-cell and cell-ECM adhesion forces may not balance tensional forces due to cell stiffening (Trepat et al., 2005). An increase in the stiffness of alveolar epithelial cells has also been observed after being stretched (Trepat et al., 2005). This increase in stiffness may be enhanced in cells exposed to thrombin, inducing an increase in the viscoelastic recoil exerted during spontaneous breathing or mechanical ventilation. All these results suggest that inward, tensional forces increase in alveolar epithelial cells exposed to proinflammatory mediators, but there is a lack in the knowledge of what is the effect in the outward, adhesive forces. A recent work reflected that histamine induced an increase in endothelial cells stiffness, which resulted in an apparent increase in the adhesion strength of the integrin-fibronectin interaction (Trache et al., 2005). However, little is known, about how proinflammatory mediators may affect the interaction of alveolar epithelial cells with the ECM on which they lay, which plays a key role in barrier dysfunction (Moy et al., 1996).

Atomic Force Microscopy has been successfully used to quantitatively evaluate cell adhesion at both multiple and single-molecule levels (Benoit and Gaub, 2002; Zhang et al., 2004a; Wojcikiewicz et al., 2003; Trache et al., 2005). To measure adhesion forces, AFM cantilevers are usually decorated with proteins specifically recognized by cell surface receptors (Lehenkari and Horton, 1999). By functionalizating the AFM cantilever with ECM proteins it is possible to mimic cell-ECM interaction and to evaluate the molecular interactions under different physiological conditions and drug treatments (Wojcikiewicz et al., 2003; Zhang et al., 2002; Li et al., 2003; Kokkoli et al., 2004; Kim

et al., 2003). In addition, AFM is also used to measure the viscoelastic properties of living cells (Alcaraz et al., 2003).

When probing cell mechanics, an important limitation appears with commercially available AFM cantilever tips. The common geometry use to beis pyramidal or conical. Such a tip geometry leads to a not well defined contact geometry, and a nonlinear force response due to the increasing area of contact as the tip indents the sample. Some authors attached spherical beads to the cantilever to better control the contact area (Mahaffy et al., 2000; Dimitriadis et al., 2002; Hyonchol et al., 2002). Even using spheres, the actual contact area increases with indentation, leading to a non linear response. In soft samples, such as living cells, it is very difficult to accurately determine the point of contact due to the low signal to noise ratio at low indentation depths (Mahaffy et al., 2000; A-Hassan et al., 1998; Touhami et al., 2003). The common visual determination of the point of contact may thus introduce an uncertainty in the indentation value, *i.e.* an uncertainty in the contact area. The use of flat-ended cylindrical tips with known radius may reduce this limitation by imposing a constant area of contact. Focused Ion Beam (FIB) technology has been successfully used to modify AFM cantilevers and tips and it may be appropriate to obtain flat-ended cantilever tips (Hodges et al., 2001; Obataya et al., 2005) .

The aim of the work was to study the effects of thrombin on RGD mediated adhesion and on stiffness of alveolar epithelial cells using cylindrical AFM cantilever tips. We modified silicon cantilever tips using FIB technology to carry out measurement under a constant area of contact. Adhesion properties were quantified by measuring the detachment force, the work of de-adhesion, and the loading rate of the interaction between RGD coated cantilevers and alveolar epithelial cells. The stiffness of alveolar epithelial cells was also measured under basal and inflammatory conditions.

6.2 Materials and Methods

6.2.1 Cantilever modification using FIB technology

Commercial Au coated silicon chips carrying cantilevers (nominal spring constant k = 0.03 N/m (MikroMasch, Estonia)) with pyramidal tips (15-20 μm height) were placed on the FIB (FEI Company, Hillsboro, USA) sample holder. Tips were then milled using a ring-like pattern (2 μm inner diameter, 5 μm outer diameter) centred with the tip apex but tilted by an angle of 8^o with respect to the axis of the pyramid. The end of the resulting cylinder-like tip was then removed milling a straight line pattern perpendicular to the cylinder axis. The resulting tip was a flat ended cylinder (~1.5 μm diameter, ~10 μm

high) tilted ~8°.

6.2.2 Cantilever fuctionalization

Modified Si cantilevers were cleaned using piranha solution (70% H_2SO_4, 30% H_2O_2, 30 min), acetone (5 min), and UV irradiated (15 min). Cantilevers were then soaked in a solution of 5% 3-aminopropyltriethoxysilane (Fluka, Switzerland) in acetone, rinsed with distilled water, and shacked for 30 min in a solution of 0.5% glutaraldehyde (Sigma, USA). Cantilevers were then washed extensively with distilled water and air dried. Afterwards, cantilevers were immersed in 0.1 mg/ml solution of GRGDSP peptide (Calbiochem, Germany) for at least 2 h. Unbound proteins were removed rinsing with PBS. Cantilevers were immersed in a solution of 0.1% BSA in PBS for 30 min, and rinsed again with PBS. Functionalized cantilevers were stored in PBS at 4°C until use.

6.2.3 Measurements

Measurements were carried out using a home-made AFM-based system mounted on the stage of an inverted optical microscope (see Chapter 3). Briefly, the cantilever was positioned by means of piezoelectric translators with strain-gauge position sensors (in closed loop mode, displacement ranges were 32 μm (z) and ~80x80 μm^2 (xy) (Piezosystem Jena, Germany)). An analog proportional-integral circuit was used to servocontrol the movement. The deflection of the cantilever was measured using the optical lever method. A near infrared laser beam (Schäfter + Kirchhoff GmbH, Germany) was reflected off the backside of the cantilever and detected using a 4-quadrant photodiode (Hamamatsu, Japan). The photodiode and the z position sensor signals were low-pass filtered (Butterworth, 256 Hz, 8 poles), sampled with a 16-bit acquisition board PCI-6733, National Instruments, USA), and stored on a personal computer for further processing.

Six force-distance curves were recorded at three retraction speeds (15 μm peak-to-peak at 0.1 Hz, 0.3 Hz, and 1 Hz) after 7 min of treatment with thrombin 5 U/ml final concentration, or vehicle (control) (N = 8). The cantilever was kept in contact at a constant indentation of ~1 μm for 20 s before retraction.

To test the specificity of adhesion a similar protocol (at a single frequency 0.3 Hz) was applied on cells preincubated for 20 min in a solution of 0.5 mg/ml of GRGDSP peptide to block integrins.

Elasticity measurements were carried out by applying force curves (4 μm, 0.3 Hz) reaching a maximum indentation of ~1 μm. Three force curves were recorded before and after adhesion measurements. The value of E for each set of measurements was the

average of the values obtained before and after adhesion measurements.

6.2.4 Staining

F-actin and integrin β_1 were co-stained with rhodamine-phalloidin and with cd29-alexa488 (Molecular Probes, Carlsbad, CA, USA), respectively, on cells treated during 7 min with vehicle or thrombin 5 U/ml, after being fixed with 3.7% paraformaldehyde. Fluorescent images were obtained using an oil-immersed 60X objective with a cooled CCD camera (Orca, Hamamatsu, Japan) coupled to an inverted optical microscope (TE2000 Eclipse, Nikon, Japan).

6.2.5 Data processing

Detachment force and work of adhesion were calculated from retracting curves. Adhesion work was computed by integrating the force over the displacement of the cantilever tip until the latest adhesion event occurred. Detachment force was computed from the peak of force in the unloading curve. Both detachment force and work of de-adhesion were divided by the area of contact computed from the actual measured radius of each cantilever. Loading rate was estimated by fitting a polynomial of first degree to the unloading curve, from the point where the force changed from positive to negative until the minimum peak of force. Drag force exerted on the cantilever due to the surrounding medium was corrected by computing the viscous drag coefficient b at different distances from the surface (Alcaraz et al., 2002).

The indentation was calculated from the displacement of the piezo translator and the deflection of the cantilever as $\delta = z - z_c - d + d_{off}$, where z_c is the point of contact, and d_{off} the deflection offset. For a flat-ended cylindrical tip indenting an elastic half space with Young's modulus E, the $F(\delta)$ relationship is

$$F = \frac{2E}{1-\nu^2} a\delta \tag{6.1}$$

where a is the radius of the cylinder and ν is the Poisson's ratio of the sample, assumed to be 0.5. E, z_c, d_{off} were estimated simultaneously fitting Eq. 6.1, expressed in terms of z and d, to approaching d-z curves using a nonlinear least squares algorithm (Matlab 7.0, The MathWorks Inc., Natick, MA, USA).

6.2.6 Statistics

Data were reported as means ± SE unless otherwise stated. Differences in the mean values of E for control and treated cells were compared by Student's t-test. Detachment force, work of de-adhesion, and loading rate values obtained with different treatments were analyzed using two ways analysis of variance (ANOVA). Statistical significance was assumed at $p < 0.05$.

6.3 Results

Cylindrical tip radii were measured from SEM images acquired after FIB modification (Fig. 5.2). The average value obtained was $a = 668 \pm 46nm$ (mean ± SD).

Cantilever spring constants as computed from the thermal fluctuations method (Hutter and Bechhoefer, 1993; Butt and Jaschke, 1995) differed from their nominal values (k = 0.096 ± 0.021 N/m, mean ± SD). The difference may be due to the high variability of cantilever thickness as a result of its fabrication process, and from the added Cr-Au coating (Sader et al., 1995).

Representative examples of d-z curves obtained with cylindrical tips on an A549 cells under control and inflammatory conditions are shown in Fig. 6.1. Curves presented a fairly linear behavior as expected for a cylindrical indenter. The fit of the cylindrical model to the loading curve was good (r^2 = 0.9958, root mean square error rms = 0.7792 nm), although systematic deviations were observed near the point of contact. This deviations may be explained by three main causes. First, the non homogenous surface of the cells due to their glycocalix. Second, the slightly roundness of cylindrical tips due to their fabrication process. And third, possible systematic inclination of the tip from the normal indentation. The last two causes have been explained in detail in Chapter 5. Steric forces associated with the brush-like glycocalix of living cells have been previously described (Fritz et al., 1994; Lee and Marchant, 2000). Steric forces may superimpose to the purely elastic forces near the point of contact causing a slight increase in the resulting cantilever deflection. This may lead to the observed deviation from the ideal elastic behavior described by the contact model (Eq. 6.1).

Representative examples of the unloading curves obtained in treated and untreated cells are shown in Fig. 6.2. The shaded region represent the computed work of de-adhesion. The minimum force value below the zero force level (dotted line) was used to estimate the detachment force. The force response while pulling the cell before breakage occurred was fairly linear, reflecting again the constant area of contact.

Thrombin induced a significant ~2-fold increase in the Young's modulus as revealed

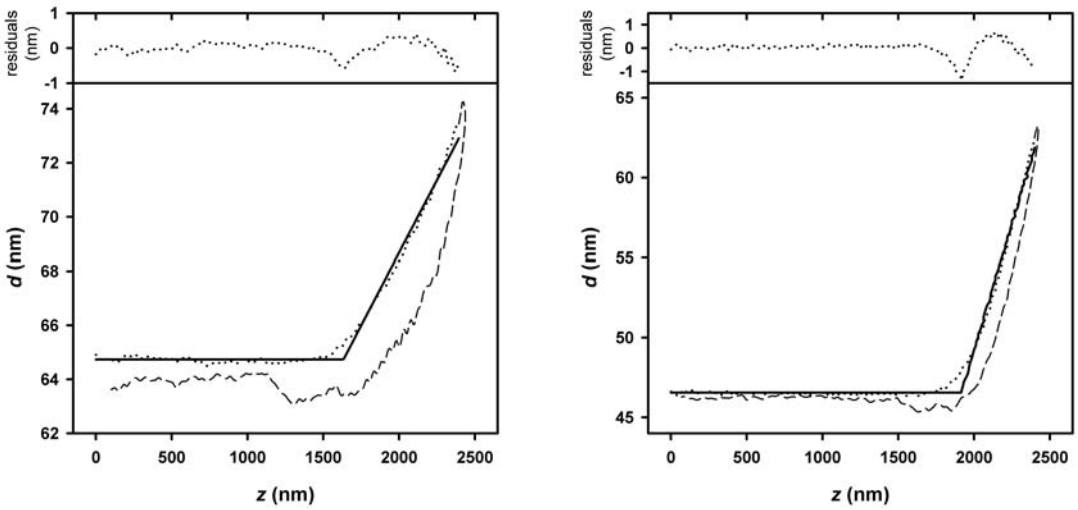

Figure 6.1: Representative examples for *d-z* curves obtained on A549 cells treated with vehicle (left) and thrombin (right) using cylindrical tips. The cylindrical contact model was fitted (solid line) to the loading curve (dotted line). The fitted parameters were E = 0.73 kPa, z_c = 1722 nm, and d_{off} = 64.74 nm (control), and E = 1.69 kPa, z_c = 1970 nm, and d_{off} = 46.56 nm (thrombin). The retracting curve (dashed line) reflected viscous hysteresis and adhesion events. Insets show residual errors.

from *d-z* measurements (Fig. 6.3). Mean detachment force and work of de-adhesion values are shown in Fig. 6.4 as a function of the loading rate. Both work and force depended strongly on cantilever retraction speed ($p<0.001$). We found no statistical significance in the mean values of detachment force and work of de-adhesion at the three applied retraction speeds ($p=0.077$ and $p=0.955$, respectively). However, thrombin induced a significant augment in the loading rate ($p<0.05$).

Pretreatment of A549 cells with soluble RGD containing peptide for 20 min induced a significant decrease in the detachment force and in the work of de-adhesion ($N>4$, Fig. 6.5).

F-actin and β_1 integrin co-staining revealed a rearrangement of the actin filaments after 7 min of treatment with thrombin. After treatment with thrombin, F-actin distributed near the cell borders forming a ring like distribution with thicker filaments. Integrin receptors appeared uniformly located over the cell surface with higher concentration in cell borders (Fig. 6.6). Thrombin appeared not to modify β_1 receptors.

6.4 Discussion

We modified pyramidal Si AFM cantilever tips to obtain flat-ended cylindrical tips. The tips enabled us to carry out AFM force measurements with a controlled, constant area

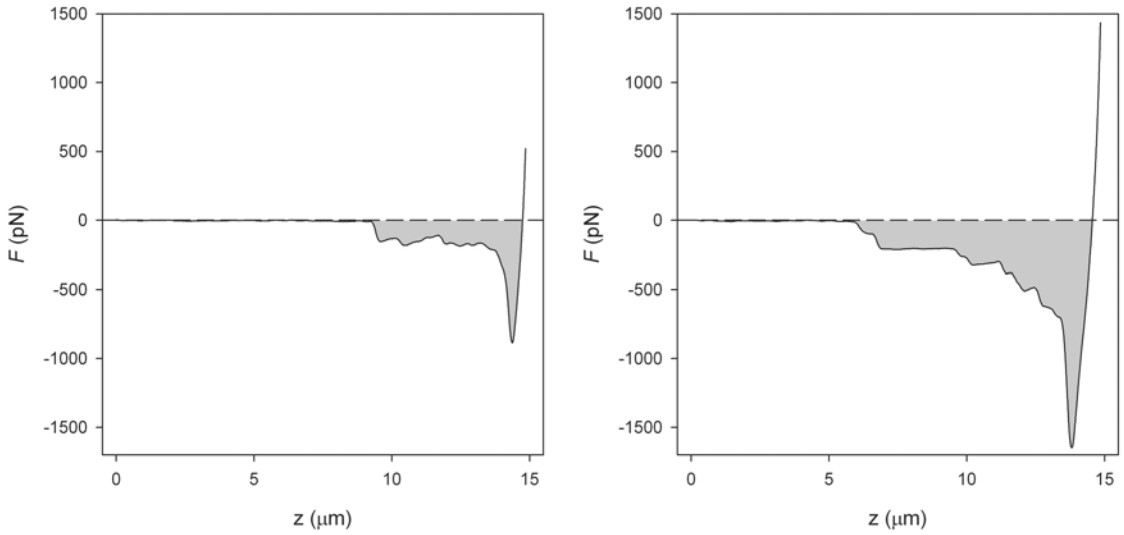

Figure 6.2: Representative examples for *F-z* curves obtained on A549 cells treated with vehicle (left) and thrombin (right) using a cylindrical tip at a retraction speed of 10 μm/s. The work of de-adhesion was computed as the area below the zero force level (shaded area). The detachment force was computed as the minimum force value. The slope of the linear curve before the minimum force value determined the effective stiffness and was used to compute the loading rate by multiplying it by the cantilever velocity.

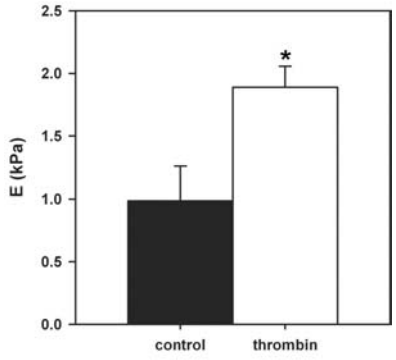

Figure 6.3: Young's modulus (E) computed by fitting the flat-ended cylindrical contact model to the loading part of *F-z* curves. E was significantly higher in cells treated with thrombin.

of contact. Tips were functionalized using GRGDSP peptide. We measured Young's modulus, work of adhesion, detachment force and loading rate on living alveolar epithelial cells treated with thrombin. The results were compared with those obtained on untreated cells. We found significantly higher values of E and loading rate on thrombin treated cells. No significant augment was found in work of de-adhesion and detachment force. Pretreatment of cells with soluble RGD containing peptide significantly reduced both work of adhesion and detachment force.

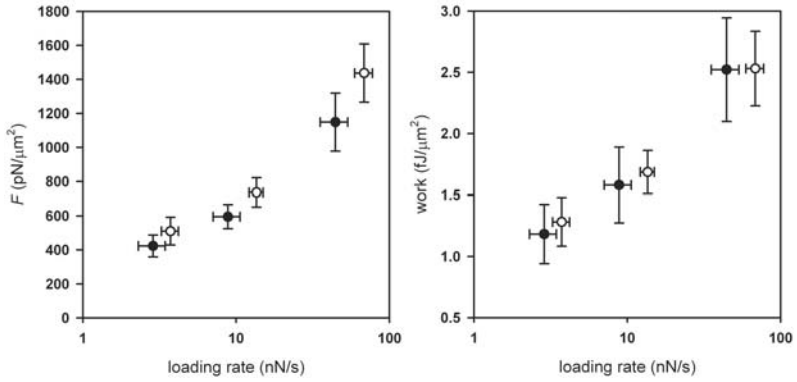

Figure 6.4: Detachment force (left) and work of de-adhesion (right) versus loading rate for control cells (solid circles) and thrombin treated cells (open circles).

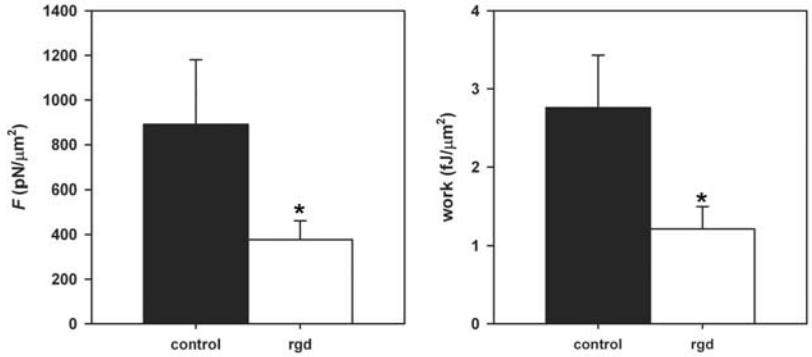

Figure 6.5: RGD soluble peptide inhibited significantly detachment force (left) and work of adhesion (right).

The shape modification of the cantilever tips was carried out to maintain a constant area of contact during measurements. In common adhesion AFM measurements, it is usual to control the maximum indentation force by using a deflection trigger threshold. This force threshold determines the maximum indentation reached in each force curve. This maximum indentation depends on the applied force, on the tip geometry, and on the sample stiffness. Thus, when working at a constant force of contact, if cell stiffness changes, the indentation might also vary. The use of common pyramidal or spherical tips would lead to a different area of contact, thus a different quantity of binding sites. This change of binding sites may lead to a change in the measured adhesion parameters (work and force), and might be interpreted as an change in adhesion strength. With the common used pyramidal cantilevers tips (four-sided, $\theta = 35$ deg), assuming a typical indentation force of ~200 pN, a 2-fold increase in elasticity may lead to a ~4-fold reduction in the area of contact. Assuming an homogeneous distribution of binding sites and no alteration of the adhesion properties of the sample, the detachment force may be reduced by

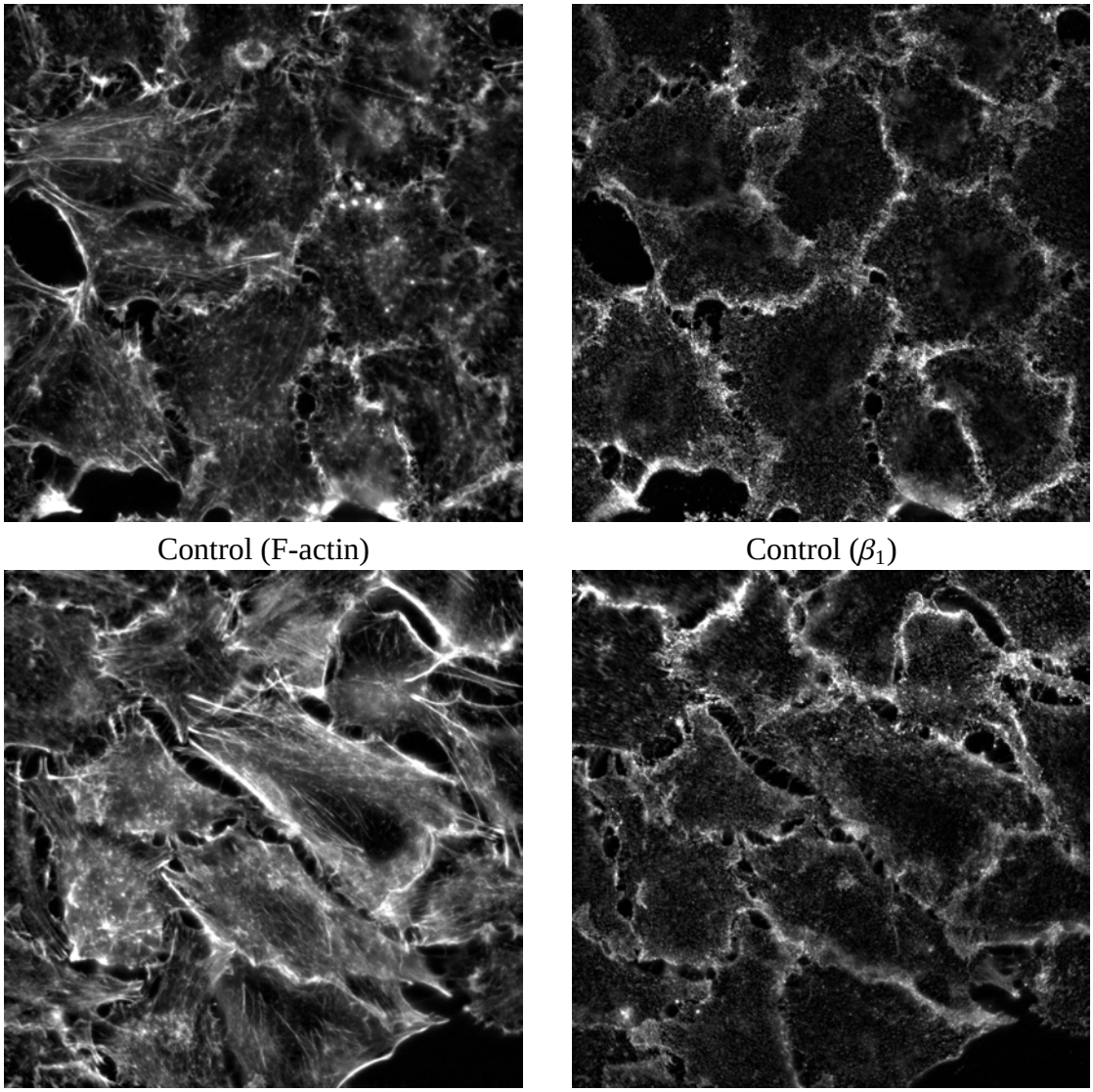

Figure 6.6: F-actin (left) and integrin subunit β_1 (right) staining in A549 cells after seven minutes of treatment with vehicle (top) and thrombin 5 U/ml (bottom).

a similar amount, leading to a possible misinterpretation of the obtained results. This limitation of force control has been previously reflected in the study of Wojcikiewicz and co-workers when measuring adhesion properties with cells attached to the cantilever. The authors found a ~3-fold increase in the detachment force. However, as authors described, this strong augment was mainly due to a 5-fold increase in cells compliance, which lead to an almost 3-fold increase in the area of contact reached during measurements. The detachment force is proportional to the number of formed bonds and, therefore, to the area of contact (Evans, 2001). The work of de-adhesion depends on both the number of bonds and the elasticity of the sample, and indirectly thus to the contact area. A more

general way to represent this magnitudes may be by units of force or work per units of area. The surface energy of adhesion is a common magnitude used to described adhesion properties of materials since it does not depend on the system of measurement (Johnson, 1985). Measuring the work per unit area provides a general magnitude to characterize specific adhesion properties of cells. Therefore, a controlled area of contact seems necessary to obtain comparable results between different studies. Cylindrical tips ensure a constant and known area of contact. Since it is not always possible the use of cylindrical tips, the knowledge of the actual tip geometry and determination of the indentation depth may provide the necessary tools to compute the actual area of contact.

The above discussion obviates an important property of molecular interactions: the force of adhesion is proportional to the logarithm of the loading rate, *i.e.* the rate at which force is applied. AFM force curves are acquired at constant cantilever velocity. Thus, a variation in the stiffness of the sample results in a change in the applied loading rate which, in turn, lead to a variation in the adhesion parameters (Benoit and Gaub, 2002). As pointed out by Wojcikiewicz and co-workers, an increase in the sample compliance is expected to result in an augment in the work of adhesion, which may be overestimated a certain amount due to the decrease in the resulting loading rate.

Another remarkable issue arises when carrying out measurements by controlling the force threshold with conventional cantilever tips. As mention in section 1.3, the frequency dependence of cell viscoelasticity follows a weak power law that can be described by a structural damping model (Fabry et al., 2001). This means that cells appear stiffer when probed at high frequencies than they do at lower ones. Force curves on living cells are usually acquired at different velocities but at a same indentation force. Thus, at high velocities cells may appear harder than they do at lower ones. At a given force, the area of contact diminishes with the increasing stiffness of the sample. Therefore, at high frequencies, the area may be smaller than at lower frequencies, affecting again adhesion measurements. Cylindrical tips prevent also from this possible artifact by maintaining a constant area of contact.

The method used to functionalize the cantilever takes advantage of the activated amino groups of the silanized surface, providing a stable binding between the RGD peptide and the silicon tip. This ensures no detachment of the coating proteins during measurements. The method has been successfully used to bind different proteins to silicon surfaces (Wagner, 1998; Sagvolden et al., 1999; Moy et al., 1999; Zhang et al., 2004b; Willemsen et al., 2000). The latter step of the functionalization process, addition of BSA, blocked the excess aldehyde, reducing unspecific adhesion between tip and sample. The used peptide GRGDSP contained the RGD sequence with is found in the cell-binding domain of both

fibronectin and laminin, important components of the ECM. It has been shown that the fibronectin interaction with $\alpha_5\beta_1$ integrin was due to both the RGD sequence and the synergy site residues (Li et al., 2003). However, RGD containing peptides have been extensively used as a model of cell-ECM interaction for its simplicity and well characterization (Lehenkari and Horton, 1999; Kokkoli et al., 2004; Lee and Marchant, 2000; Kato and Mrksich, 2004; Maheshwari et al., 2000).

Adhesion measurements reflected a slight increase in both detachment force and work of adhesion (Fig. 6.4). However, the increase did not reach statistical significance. The loading rate, in contrast, augmented significantly in cells treated with thrombin. This was a reflect of the increased cellular stiffness. It is noteworthy that the loading rate was not directly proportional to the cantilever velocity, as expected for an elastic material. This effect may be due to the increase in stiffness of the cells as they are probed at higher frequencies, which is in accordance with the structural damping behavior observed in these and other kinds of cells (Fabry et al., 2001, 2003; Trepat et al., 2005; Alcaraz et al., 2003). Due to the controlled area of contact it was possible to obtain a measure of the detachment force per unit area. In the measurements described here, the configuration of the bonds could be approached to N bonds in parallel. In such a system the detachment force can be approximated to be $F_d = N f^*$, being f^* the detachment force of a single bond (Evans, 2001). Taking into account the data found in the literature about RGD-integrin interaction force, and the data we found it would be possible to compute the number of bonds per area, which gives an estimate of the integrin density. Li and co-workers reported the Bell parameters for the interaction between $\alpha_5\beta_1$ at different conditions (high and low affinity) and fibronectin (FN7-10) with various mutations (Li et al., 2003). They used wild-type FN7-10 and FN7-10 with deleted RGD sequence and with mutated synergy site. Using the reported Bell parameters for the interaction between high-affinity integrin and FN7-10 with mutated synergy site, we observed that their data was in good agreement with our results by assuming the breakage of seven bonds. This accordance suggested that our measured interaction may be due to the cooperativity of single bonds in parallel mediated by $\alpha_5\beta_1$ integrin, which has been found in pulmonary epithelial cells (Sheppard, 2003). Our adhesion measurements were carried out by keeping the tip in contact with the cell surface for 20 s. This relatively long time ensured reaching a plateau value for the binding probability (Zhu, 2000; Thoumine et al., 1999). Assuming a closely packed distribution of RGD peptides on the tip surface, there would be of 10^5 peptides/μm^2. Thus, the cell-RGD interaction may be mainly conditioned by the density of RGD receptors. Assuming 100% binding probability we could predict the minimum estimate for the number of RGD-binding sites on alveolar epithelial cells to be ~10 sites/μm^2. This might

be a very conservative estimate due to the mentioned assumptions and taking into account that our force curves were acquired near the center of the cell, where the integrin density might be lower, as revealed the immunostaining images (Fig. 6.6). Different studies reported estimations for the density of integrin receptors with a very wide range of values, from few tenths to several thousands (Hyonchol et al., 2002; Bell, 1978; Zhu, 2000).

To test the specificity of the interaction, adhesion measurements were carried out on A549 cells preincubated with soluble RGD peptide. The significant reduction in both force and work of adhesion suggested that the measured interaction was mainly due to RGD mediated bonds. There are at least twelve integrins that recognize the RGD sequence, from which five of them are present in pulmonary epithelial cells (Sheppard, 2003; Ruoslahti, 1996). To determine the particular receptors involved in the RGD-cell adhesion, inhibition assays using specific antibodies might be carried out.

The found increase in cellular stiffness induced by thrombin was in accordance with previous results obtained on the same cell type but using optical magnetic twisting cytometry (OMTC) (Trepat et al., 2005). The authors found a ~3-fold increase in cellular stiffness after the addition of thrombin. The slightly intensified increase observed using OMTC may be due to the direct binding of the magnetic beads to the actin cytoskeleton. Beads were recovered with an RGD containing peptide and placed on the cell surface during 15 min before measurements, ensuring the formation of focal adhesions. Thus, OMTC probes, mainly, the viscoelasticity due to the actin cytoskeleton. On AFM measurements, even though tips were also functionalized with an RGD containing peptide, focal adhesions were not allowed to form when probing sample stiffness, since the duration was limited to 20 s. Thus, AFM measurements may lead to a more global estimate of cell stiffness since the AFM tip deforms the whole cell ~1 μm depth, and not only the actin cytoskeleton and immediate surroundings. However, the accordance between the two techniques based on different probes and assumptions reflects their complementarity to measure mechanical properties of living cells.

The increased cellular stiffness was accompanied with a structural rearrangement of the actin cytoskeleton as revealed by F-actin immunostaining (Fig. 6.6). This reorganization of actin cytoskeleton has been also found by other authors (Kawkitinarong et al., 2004; Trepat et al., 2005). We observed formation of actin filament bundles near cell periphery. Thicker filaments may be cross-linked by actomyosin cross-bridges, forming stress fibers which are able to generate force. Indeed, Kawkitinarong and co-workers found an increase in the phosphorylation of myosin light chain (Kawkitinarong et al., 2004). In addition, recent results from our laboratory suggest a ~20% increase in actin polymerization in alveolar epithelial cells treated with thrombin (Gavara, 2005). More-

over, disruption of the actin cytoskeleton using cytochalasin D has shown to inhibit significantly the increased stiffness induced by thrombin (Trepat et al., 2005). These results reveal the important role of actin cytoskeleton in cellular mechanics of alveolar epithelial cells. It has been shown in different types of cells that the activation of the contractile machinery is commonly paralleled by an increase in cellular stiffness (Fabry et al., 2001, 2003; Hubmayr et al., 1996). Thus, the observed augment induced by thrombin may also be a reflect of the activation of the actomyosin machinery, which may lead to cell contraction. In fact, visualization of A549 cells using traction microscopy has revealed a marked ~3-fold increase in the force generated by these cells (Gavara, 2005). A reorganization of the actin cytoskeleton may induce to think in a rearrangement of the molecules linked to actin, as integrins are. We stained integrins subdomain β_1 which form part of the fibronectin integrin receptors found in A549 cells, $\alpha_5\beta_1$. Labelled β_1 were homogeneously distributed within the whole cell body, with an apparent higher density near the cell periphery (Fig. 6.6). Thrombin treated cells revealed no apparent redistribution of the stained integrins, in accordance with the no significant results obtained for the measured adhesion parameters.

Our results showed a tendency of increasing the detachment force in cells treated with thrombin, although they were found to be not significant. Recent measurements at the single molecule level of integrin-fibronectin interaction have been reported on endothelial cells treated with hystamine (Trache et al., 2005). Authors found a significant increase in the adhesion strength of fibronectin mediated interactions due to an increase in cellular stiffness, which lead to a parallel augment of the loading rate. The possible explanation of the difference in the statistical significance of the results may be a reflect of the number of measurements carried out. Our data are the average of eight different sets of measurements carried on different cells. Trache and co-workers averaged hundreds of single molecule rupture events carried out on a limited number of cells. Thus, their study focused in the molecular integrin-fibronectin interaction, while we were interested in whole cell adhesion. Our work, however, reveals the direct link between adhesion and viscoelastic properties, which is in accordance with the conclusions of the mentioned paper.

The work of de-adhesion comprises the work necessary to break the formed bonds and the elastic work needed to deform the sample. The work due to elastic deformation can be expressed as

$$W_e = \int F dz_t \tag{6.2}$$

since the response for a cylindrical punch is linear $F = k_c z_t$, where k_c is the effective spring constant of the cell-cantilever system, and z_t the displacement of the tip. The

effective spring constant is computed as $k_c = l_r/v$, with l_r and v being the loading rate and the velocity of the cantilever, respectively. Thus

$$W_e = \int k_c z_t dz_t = \frac{k_c z_t^2}{2} = \frac{F^2}{2k_c} \tag{6.3}$$

Using the obtained values of peak forces and loading rates, the elastic work was computed from Eq. 6.3. Elastic work resulted to be ~12%, ~13%, and ~19% of the total adhesion work for thrombin, computed at the three cantilever velocities, respectively. Control values were very similar being ~12%, ~16%, and ~18% of the total work. These results revealed two remarkable issues. First, the elastic work increased with cantilever velocity. And second, the elastic work did not vary significantly for cells treated with thrombin. At first glance, both results may be counterintuitive. On the one hand, the elastic work for a purely elastic material may be independent of the velocity at which it is probed. However, as reviewed in Section 1.3, cells viscoelasticity has a frequency dependence. This may be the cause of the observed velocity dependence of the elastic work. On the other hand, the stiffer a material is (as cells treated with thrombin) the lower the elastic work may be (Eq. 6.3). However, a stiffer material also leads to a higher loading rate which, in turn, results in a higher detachment force. Due to the dependence on the force of Eq. 6.3, the increased effective spring constant may be counterbalanced by the increased detachment force, leading to non significant changes between control and thrombin treated cells. The above discussion reflects how important the sample viscoelasticity is to the adhesion properties. This issue has been previously observed by Wojcikiewicz and co-workers (Wojcikiewicz et al., 2003). The authors studied murine T-cells (3A9 cell line), *i.e.* non-adherent cells that travel within and migrate through vessels. In the case of non-adherent cells, a decrease in their stiffness leads to an increase in the binding probability due to the increase in the contact area for a given force of contact, and a consequently increase in the number of adhesion sites. However, the physiological system described here is different from that involving suspended cells. Alveolar epithelial cells are adherent cells and the forces and deformations involved in their function are related with the dynamic behavior of the respiratory system. As mentioned before, alveolar epithelium integrity is controlled by a balance in the inward forces, generated from contractile stresses and viscolastic recoil, and the outward forces supported by cell-cell and cell-ECM contacts. It has been shown that an increase in cellular stiffness is normally linked to an activation of the contractile apparatus of the cells. The greater the inward contractile forces, the stiffer the cells are (Fabry et al., 2001, 2003; Trepat et al., 2005). Thus, thrombin may increase the contractile machinery of the cells leading to an augment in the inwards forces. In addition, the viscoelastic recoil forces due to spontaneous breathing may also increase as

a result of the augment in epithelial cells stiffness. Our measurements showed no significant change in adhesion strength after thrombin stimulation, even if a significant increase in the loading rate resulted from the stiffness augment. Adhesion measurements, thus, suggest a maintenance of the outward forces related with adhesion with the ECM. Therefore, the found apparent augment of the inward forces together with the maintenance of the outward forces obtained may induce to think on a breakage in the balance of forces of the alveolar epithelium with its substratum, which has been proposed as an important cause of alveolar-capillary barrier disfunction.

In conclusion, cylindrical tips were used to measure the viscoelastic and adhesion properties of living alveolar epithelial cells in response to inflammatory mediators. Cylindrical tips were found to be appropriate to measure cell adhesion properties, enabling us to report the results in comparable units of measure, *i.e.* non area dependent. Our results showed that thrombin induced a significant increase in the stiffness of alveolar epithelial cells, which resulted in a parallel and significant increase in the loading rate. However, thrombin did not significantly modify cell adhesion properties. The measured increase of cell stiffness, together with the invariant cell-ECM adhesion properties might suggest a partial rupture in the balance of inward and outward forces, a possible detachment of alveolar epithelial cells from their substratum, and a consequent disruption in the alveolar-capillary barrier.

Bibliography

E. A-Hassan, W. Heinz, M. D. Antonik, N. P. D'Costa, S. Nageswaran, C. A. Schoenenberger, and J. H. Hoh. Relative microelastic mapping of living cells by atomic force microscopy. *Biophys.J.*, 74:1564–1578, 1998.

J. Alcaraz, L. Buscemi, M. Puig de Morales, J. Colchero, A. Baro, and D. Navajas. Correction of microrheological measurements of soft samples with atomic force microscopy for the hydrodynamic drag on the cantilever. *Langmuir*, 18(3):716–721, 2002.

J. Alcaraz, L. Buscemi, M. Grabulosa, X. Trepat, B. Fabry, R. Farre, and D. Navajas. Microrheology of human lung epithelial cells measured by atomic force microscopy. *Biophys.J.*, 84:2071–2079, 2003.

G. I. Bell. Models for specific adhesion of cells to cells. *Science*, 200(4342):618–627, 1978.

M. Benoit and H. E. Gaub. Measuring cell adhesion forces with the atomic force microscope at the molecular level. *Cells Tissues Organs*, 172(3):174–189, 2002.

L. Buscemi, M. Grabulosa, F. Rico, X. Trepat, R. Farre, and D. Navajas. Effect of thrombin on the mechanical properties of alveolar epithelial cells measured with atomic force microscopy. *Biophys.J.*, 84(2):440A, 2003a.

L. Buscemi, M. Grabulosa, X. Trepat, F. Rico, D. Navajas, and R. Farre. Effects of inflammatory mediators on the mechanical properties of human alveolar epithelial cells. *FASEB J.*, 17(5):A1217, 2003b.

H. J. Butt and M. Jaschke. Calculation of thermal noise in atomic force microscopy. *Nanotechnology*, 6:1–7, 1995.

M. Puig de Morales, E. Millet, B. Fabry, D. Navajas, N. Wang, J. P. Butler, and J. J. Fredberg. Cytoskeletal mechanics in adherent human airway smooth muscle cells: probe specificity and scaling of protein-protein dynamics. *Am.J.Physiol.-Cell Physiol.*, 287(3):C643–C654, 2004.

E. K. Dimitriadis, F. Horkay, J. Maresca, B. Kachar, and R. S. Chadwick. Determination of elastic moduli of thin layers of soft material using the atomic force microscope. *Biophys.J.*, 82:2798–2810, 2002.

S. M. Dudek and J. G. Garcia. Cytoskeletal regulation of pulmonary vascular permeability. *J.Appl.Physiol*, 91(4):1487–1500, 2001.

E. Evans. Probing the relation between force - lifetime - and chemistry in single molecular bonds. *Annu.Rev.Biophys.Biomol.Struct.*, 30:105–128, 2001.

B. Fabry, G. N. Maksym, J. Butler, M. Glogauer, D. Navajas, and J. J. Fredberg. Scaling the microrheology of living cells. *Phys.Rev.Lett.*, 87:148102–148105, 2001.

B. Fabry, G. N. Maksym, J. P. Butler, M. Glogauer, D. Navajas, N. A. Taback, E. J. Millet, and J. J. Fredberg. Time scale and other invariants of integrative mechanical behavior in living cells. *Phys.Rev.E*, 68(4), 2003.

M. Fritz, M. Radmacher, and H. E. Gaub. Granula motion and membrane spreading during activation of human platelets imaged by atomic force microscopy. *Biophys.J.*, 66(5):1328–1334, 1994.

N. Gavara. Personal communication. 2005.

T. Geiser. Mechanisms of alveolar epithelial repair in acute lung injury–a translational approach. *Swiss Med.Wkly.*, 133(43-44):586–590, 2003.

A. R. Hodges, K. M. Bussmann, and J. H. Hoh. Improved atomic force microscope cantilever performance by ion beam modification. *Rev.Sci.Instr.*, 72(10):3880–3883, 2001.

R. D. Hubmayr, S. A. Shore, J. J. Fredberg, E. Planus, Jr. R. A. Panettieri, W. Moller, J. Heyder, and N. Wang. Pharmacological activation changes stiffness of cultured human airway smooth muscle cells. *Am.J.Physiol*, 271(5 Pt 1):C1660–C1668, 1996.

J. L. Hutter and J. Bechhoefer. Calibration of atomic-force microscope tips. *Rev.Sci.Instr.*, 64(7):1868–1873, 1993.

K. Hyonchol, H. Arakawa, T. Osada, and A. Ikai. Quantification of fibronectin and cell surface interactions by afm. *Colloid Surf.B-Biointerfaces*, 25(1):33–43, 2002.

K. L. Johnson. *Contact Mechanics*. Cambridge University Press, Cambridge, 1985.

M. Kato and M. Mrksich. Using model substrates to study the dependence of focal adhesion formation on the affinity of integrin-ligand complexes. *Biochemistry (Mosc).*, 43 (10):2699–2707, 2004.

K. Kawkitinarong, L. Linz-McGillem, K. G. Birukov, and J. G. Garcia. Differential regulation of human lung epithelial and endothelial barrier function by thrombin. *Am.J.Respir.Cell Mol.Biol.*, 31(5):517–527, 2004.

H. Kim, H. Arakawa, T. Osada, and A. Ikai. Quantification of cell adhesion force with afm: distribution of vitronectin receptors on a living mc3t3-e1 cell. *Ultramicroscopy*, 97(1-4):359–363, 2003.

E. Kokkoli, S. E. Ochsenhirt, and M. Tirrell. Collective and single-molecule interactions of alpha(5)beta(1) integrins. *Langmuir*, 20(6):2397–2404, 2004.

I. Lee and R. E. Marchant. Force measurements on platelet surfaces with high spatial resolution under physiological conditions. *Colloid Surf.B-Biointerfaces*, 19(4):357–365, 2000.

P. P. Lehenkari and M. A. Horton. Single integrin molecule adhesion forces in intact cells measured by atomic force microscopy. *Biochem.Biophys.Res.Commun.*, 259(3): 645–650, 1999.

F. Y. Li, S. D. Redick, H. P. Erickson, and V. T. Moy. Force measurements of the alpha(5)beta(1) integrin-fibronectin interaction. *Biophys.J.*, 84(2):1252–1262, 2003.

R. E. Mahaffy, C. K. Shih, F. C. MacKintosh, and J. Kas. Scanning probe-based frequency-dependent microrheology of polymer gels and biological cells. *Phys.Rev.Lett.*, 85:880–883, 2000.

G. Maheshwari, G. Brown, D. A. Lauffenburger, A. Wells, and L. G. Griffith. Cell adhesion and motility depend on nanoscale rgd clustering. *J.Cell Sci.*, 113(10):1677–1686, 2000.

A. B. Moy, J. Van Engelenhoven, J. Bodmer, J. Kamath, C. Keese, I. Giaever, S. Shasby, and D. M. Shasby. Histamine and thrombin modulate endothelial focal adhesion through centripetal and centrifugal forces. *J.Clin.Invest*, 97(4):1020–1027, 1996.

V. T. Moy, Y. Jiao, T. Hillmann, H. Lehmann, and T. Sano. Adhesion energy of receptor-mediated interaction measured by elastic deformation. *Biophys.J.*, 76(3):1632–1638, 1999.

I. Obataya, C. Nakamura, S. Han, N. Nakamura, and J. Miyake. Nanoscale operation of a living cell using an atomic force microscope with a nanoneedle. *Nano Letters*, 5(1): 27–30, 2005.

E. Ruoslahti. Rgd and other recognition sequences for integrins. *Annu.Rev.Cell Dev.Biol.*, 12:697–715, 1996.

J. E. Sader, I. Larson, P. Mulvaney, and L. White. Method for the calibration of atomic force microscope cantilevers. *Rev.Sci.Instr.*, 66(7):3789–3798, 1995.

G. Sagvolden, I. Giaever, E. O. Pettersen, and J. Feder. Cell adhesion force microscopy. *Proc.Natl.Acad.Sci.U.S.A.*, 96(2):471–476, 1999.

D. Sheppard. Functions of pulmonary epithelial integrins: From development to disease. *Physiol.Rev.*, 83(3):673–686, 2003.

B. A. Smith, B. Tolloczko, J. G. Martin, and P. Grutter. Probing the viscoelastic behavior of cultured airway smooth muscle cells with atomic force microscopy: stiffening induced by contractile agonist. *Biophys.J.*, 88(4):2994–3007, 2005.

O. Thoumine, A. Ott, O. Cardoso, and J. J. Meister. Microplates: a new tool for manipulation and mechanical perturbation of individual cells. *J.Biochem.Biophys.Methods*, 39 (1-2):47–62, 1999.

A. Touhami, B. Nysten, and Y. F. Dufrene. Nanoscale mapping of the elasticity of microbial cells by atomic force microscopy. *Langmuir*, 19(11):4539–4543, 2003.

A. Trache, J. P. Trzeciakowski, L. A. Gardiner, Z. Sun, M. Muthuchamy, M. Guo, S. Y. Yuan, and G. A. Meininger. Histamine effects on endothelial cell fibronectin interaction studied by atomic force microscopy. *Biophys.J.*, 2005.

X. Trepat, M. Grabulosa, L. Buscemi, F. Rico, R. Farre, and D. Navajas. Thrombin and histamine induce stiffening of alveolar epithelial cells. *J.Appl.Physiol*, 98(4):1567–1574, 2005.

I. Vadasz, R. E. Morty, A. Olschewski, M. Konigshoff, M. G. Kohstall, H. A. Ghofrani, F. Grimminger, and W. Seeger. Thrombin impairs alveolar fluid clearance by promoting endocytosis of na+,k+-atpase. *Am.J.Respir.Cell Mol.Biol.*, 33(4):343–354, 2005.

Peter Wagner. Immobilization strategies for biological scanning probe microscopy. *FEBS Lett.*, 430(1-2):112–115, 1998.

L. B. Ware and M. A. Matthay. The acute respiratory distress syndrome. *N.Engl.J.Med.*, 342(18):1334–1349, 2000.

O. H. Willemsen, M. M. E. Snel, A. Cambi, J. Greve, B. G. De Grooth, and C. G. Figdor. Biomolecular interactions measured by atomic force microscopy. *Biophys.J.*, 79(6): 3267–3281, 2000.

E. P. Wojcikiewicz, X. Zhang, A. Chen, and V. T. Moy. Contributions of molecular binding events and cellular compliance to the modulation of leukocyte adhesion. *J.Cell Sci.*, 116(Pt 12):2531–2539, 2003.

X. H. Zhang, E. Wojcikiewicz, and V. T. Moy. Force spectroscopy of the leukocyte function-associated antigen-1/intercellular adhesion molecule-1 interaction. *Biophys.J.*, 83(4):2270–2279, 2002.

X. H. Zhang, A. Chen, D. De Leon, H. Li, E. Noiri, V. T. Moy, and M. S. Goligorsky. Atomic force microscopy measurement of leukocyte-endothelial interaction. *American Journal of Physiology-Heart and Circulatory Physiology*, 286(1):H359–H367, 2004a.

X. H. Zhang, S. E. Craig, H. Kirby, M. J. Humphries, and V. T. Moy. Molecular basis for the dynamic strength of the integrin alpha(4)beta(1)/vcam-1 interaction. *Biophys.J.*, 87 (5):3470–3478, 2004b.

C. Zhu. Kinetics and mechanics of cell adhesion. *J.Biomech.*, 33(1):23–33, 2000.

Chapter 7

Conclusions of the thesis

The general aim of this thesis was to improve and apply AFM methods to the measurement of mechanical properties of living cells, laying especial emphasis on the probe geometry. The first work presented here (Chapter 3) describes the design and set-up of an AFM based system which was applied to measure the mechanical properties (viscoelasticity and adhesion) of living cells under physiological conditions. The second work (Chapter 4) describes the development and validation of a blunted pyramidal elastic model used to determine the viscoelastic properties of soft gels and living cells. The third study (Chapter 5) validates the use of FIB modified flat-ended cylindrical tips to study the mechanical properties of biopolymer gels and living cells. The last work (Chapter 6) applies the modified cylindrical cantilevers and the developed AFM system to measure elastic and adhesive properties of living cells under inflammatory conditions. A brief summary of the main conclusions of this thesis is given below.

Major conclusions

AFM based system for probing mechanics of living cells

1. An AFM based force device was developed. The system enables the study of mechanical properties of living cells, such as viscoelasticity or adhesion, under physiological conditions.

2. The AFM based system is mounted on the stage of an inverted optical microscope and was designed to work together with fluorescence, bright field or phase contrast microscopy techniques, enabling the simultaneous acquisition of optical images.

Probing mechanical properties of living cells by AFM with blunted pyramidal cantilever tips

3. A contact model of a blunted pyramidal tip to compute viscoelastic properties of soft samples indented with conventional AFM pyramidal tips was developed.

4. Agarose gels and living cells probed with a blunted pyramidal tip exhibited elastic behavior with large values of Young's modulus for indentations lower than ~300 nm and a linear regime at deeper indentations. This indentation dependence paralleled that obtained with spherical tips, indicating that the larger strains applied by the pyramidal tip at the apex have minor effects on the force-indentation response. However, Young's modulus computed in the linear regime with the two tips differs by a factor of ~2.

5. Cells exhibited viscoelastic behavior with almost coincident values of the loss tangent obtained with both tips. Cells displayed a linear regime for indentations up to ~20% of cell thickness. This allows probing viscoelasticity with the pyramidal tip in a broad central region of the cell body with negligible influence of the hard substrate.

6. The obtained results suggest that pyramidal tips commonly used for AFM imaging are suitable for probing mechanical properties of soft polymer gels and living cells. The use of a single cantilever enables us to precisely correlate imaging and viscoelastic mapping of living cells.

Validation of cylindrical cantilever tips for probing mechanical properties of biopolymers by AFM

7. Flat-ended cylindrical tips were validated on an linear, elastic sample. Cylindrical tips enable us to measure the mechanical properties of soft biological samples, such as polymer gels and living cells, with AFM maintaining a constant area of contact.

Effect of thrombin on the adhesion properties of living alveolar epithelial cells measured by AFM

8. Cylindrical tips were used to measure the viscoelastic and adhesion properties of living alveolar epithelial cells in response to inflammatory mediators. Cylindrical

tips were found to be appropriate to measure cell adhesion properties using comparable units of measure.

9. Our results showed that thrombin induced a significant increase in the stiffness of alveolar epithelial cells, which resulted in a parallel and significant increase in the loading rate. However, thrombin did not significantly modify cell adhesion properties.

10. The measured increase of cell stiffness, together with the invariant cell-ECM adhesion properties might suggest a partial rupture in the balance of inward and outward forces, leading to a possible detachment of alveolar epithelial cells from their substratum, and a consequent disruption in the alveolar-capillary barrier.

Appendix A

Influence of the inclination angle of the cantilever on the $F(\delta)$ relationship of a pyramidal tip

Commercial AFM systems hold the cantilever forming a small angle with the sample surface. To assess the effect of tip inclination on mechanical measurements we estimated the contribution of each face of the pyramid. The cross-section of an ideal regular four-sided pyramid with semiincluded angle θ indenting an elastic half space with an actuation angle βg is obtained by simple geometric relations (Fig. A.1). The force exerted by a non tilted ideal pyramid is proportional to the square of the effective contact radius a^2 and, thus, proportional to its area. Assuming the same area dependence of the force for each face of the tilted pyramid, each interval I_i may contribute to the total force proportionally to its area A_i relative to the total area, A. The total area is computed by the formula for the area of a trapezoid

$$A = (a^+ + a^-)(\rho^+ + \rho^-) = h^2 \frac{\sin^2\theta}{\cos\beta}\left(\frac{1}{\cos(\theta+\beta)} + \frac{1}{\cos(\theta-\beta)}\right)^2 \tag{A.1}$$

where h is the height at which we obtain the cross-section and will not influence our calculations. The areas corresponding to each interval are

$$\begin{aligned} A_1 &= \rho_- a_- = h^2 \tfrac{\sin^2\theta}{\cos\beta\cos(\theta-\beta)} \quad \text{for } I_1 \\ A_3 &= \rho_+ a_+ = h^2 \tfrac{\sin^2\theta}{\cos\beta\cos(\theta+\beta)} \quad \text{for } I_3 \\ A_2 &= La_2/2 = h^2 \tfrac{1}{2}\tfrac{\sin\theta}{\cos\beta\sin\beta}\left(\tfrac{1}{\cos(\theta+\beta)} - \tfrac{1}{\cos(\theta-\beta)}\right) \quad \text{for } I_2 \text{ and } I_4 \end{aligned} \tag{A.2}$$

We assume that each interval may follow the $F(\delta)$ relationship of an ideal pyramid but weighted by A_i/A and with different semiincluded angles: θ-β and θ+β, for intervals 1 and

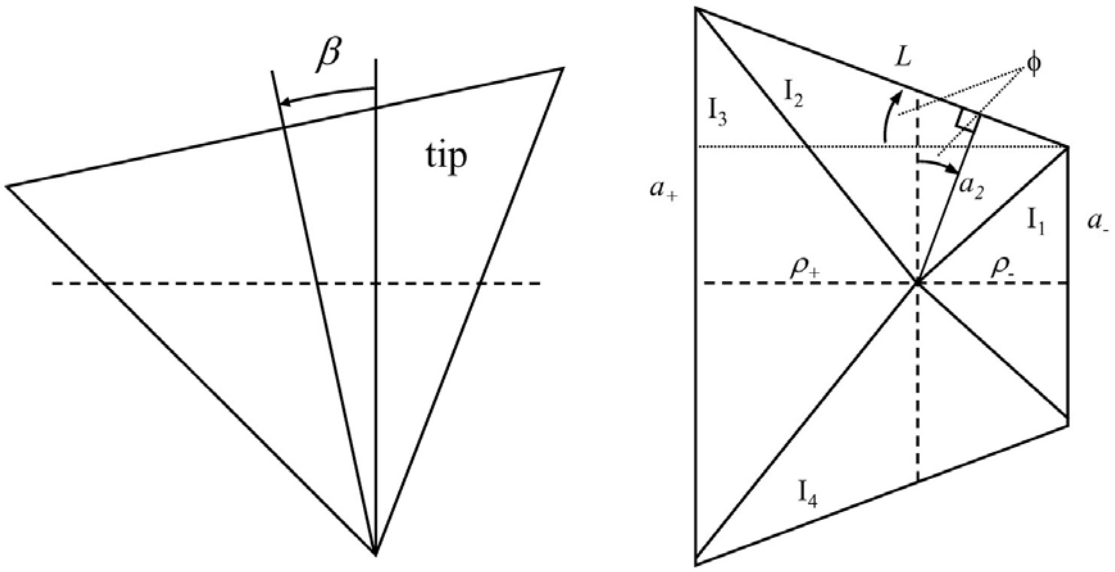

Figure A.1: Lateral view (left) and cross section (right) at a fixed indentation of an ideal four-sided pyramid tilted by an angle β.

3, respectively, and θ, for intervals 2 and 4. Thus, the force for a tilted pyramid may be the sum of the contributions of each interval

$$F_{tilted} = \frac{A_1}{A} F_{\theta-\beta} + \frac{A_3}{A} F_{\theta+\beta} + 2\frac{A_2}{A} F_{\theta} \tag{A.3}$$

where F_θ is the relationship for an ideal pyramid with semiincluded angle θ (Eq. 4.10). In the limit $\beta \to 0$, we return to the nontilted solution for a regular four-sided pyramid.

Appendix B

Calibration of the spring constant of AFM cantilevers

Abstract

Calibration of the spring constant of atomic force microscopy cantilevers is of crucial interest when accurate force measurements are required. Here we briefly review various methods related to the determination of the spring constant of V-shaped cantilevers. After comparing them, the most convenient method for our routine use was chosen.

B.1 Introduction

Since its invention in 1986 by Binnig *et al.*(Binnig et al., 1986), atomic force microscopy has been shown to be a very useful tool for probing and studying forces at the picoNewton and nanoNewton range. When precise measurements are intended it is convenient to determine the spring constant of the cantilever in use. Several methods have appeared in the literature for this purpose and here we briefly describe five of the most used and referred to in the literature.

The first method is used by several manufacturers. It consists in attaching known masses at the end of the cantilever and measuring the shift in its resonant frequency due to the added mass. The second method is an expression for the determination of the spring constant by measuring the geometry of V-shaped cantilevers and knowing its material properties (density and Young's modulus). The third and simplest method uses a precalibrated cantilever as a reference of force. The last two methods take advantage of the equipartition theorem applied to a simple harmonic oscillator (the cantilever) excited by thermal fluctuations.

B.2 Calibration methods

B.2.1 Attaching known masses[1]

A cantilever can be approximated as a spring of stiffness k and effective mass m^*. When adding a mass to such a system, its resonant frequency shifts. The measurement of this shift enables us to obtain the spring constant of the cantilever and its effective mass. The method consists in attaching known tungsten beads at the end of the cantilever, measure the changes in the resonant frequencies and computing k following the next development. The resonance frequency of a simple oscillator of spring constant k and mass m^* with an end loaded mass M is given by:

$$\nu = \frac{\omega_0}{2\pi} = \frac{1}{2\pi}\sqrt{\frac{k}{m^* + M}} \tag{B.1}$$

solving the last expression for M we obtain the relation between the mass and the resonance frequency

$$M = \frac{k}{(2\pi\nu)^2} - m^* \tag{B.2}$$

By adding several known end masses to a cantilever and measuring the new resonance frequencies, we will obtain a straight line when plotting the added mass versus $(2\pi\nu)^{-2}$ whose slope will be the spring constant and the ordinate at the origin, the effective mass. Assuming the model to be correct, the unloaded resonance frequency ν_0 and the resonance frequency ν_1 with an added mass M_1 will be enough information to determine k and m^*, from Eq. B.2,

$$k = (2\pi)^2 \frac{M_1}{\frac{1}{\nu_1^2} - \frac{1}{\nu_0^2}}, \quad m^* = M_1 \frac{\nu_1^2}{\nu_0^2 - \nu_1^2} \tag{B.3}$$

The authors report results for few added tungsten beads with known dimensions (measured by optical microcopy) and known bulk density, from which the added mass can be known (Figs. B.1a and B.1b).

Although the apparent straightforwardness of the above method there are some points to be noted. First of all, the perfect sphericity of tungsten beads and its homogeneous bulk density are assumed. In addition the determination of its diameter may be carried out by optical microscopy with probably not enough resolution. On the other hand, the practice of attaching beads is very tedious and time wasting for routine use. However, the same authors obtain another expression of the spring constant in terms of cantilever dimensions

[1] All expressions and figures appeared in this section have been extracted from ref Cleveland et al. 1993.

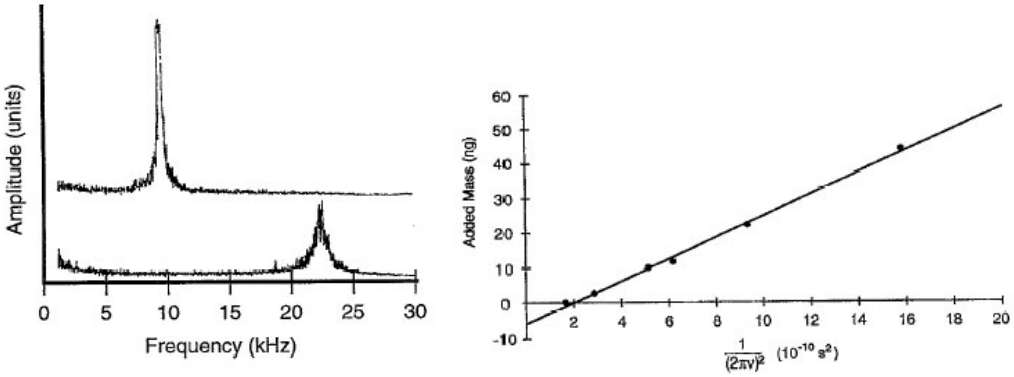

(a) (b)

Figure B.1: (a) Resonance curves of the same cantilever with and without added mass. Curves stand for the power spectrum of the deflection signals of the cantilever when driven by thermal oscillations. The lower curve is for the cantilever with no end mass and shows a peak at 22.4 kHz, the upper curve is the same cantilever with a 44 ng end mass. The resonance frequency shifted to 9.4 kHz and the quality factor Q increased. (b) Added mass vs $(2\pi\nu)^{-2}$ for a single cantilever. A simple linear regression of the data gives a spring constant (slope) of 0.031 ± 0.001 N/m and an effective mass of 6.2 ng (r=0.997).

and material properties following the next development.

The analytical expression for the spring constant of an end loaded cantilever of rectangular cross section is given by:

$$k = \frac{Et^3 d}{4L^3} \tag{B.4}$$

where E is the Young's modulus, t the thickness, d the width, and L the length of the cantilever. As mentioned, the beam can be approximated as a spring of stiffness k and an effective mass given by $m^* = 0.24 m_b$, where m_b is the mass of the beam (Butt et al., 1993). Using Eqs. B.4 and B.1, with $M = 0$, it is possible to write the unloaded resonant frequency in terms of cantilever properties ($m_b = \rho\omega tl$, with ρ the bulk density):

$$\nu_0 \simeq \frac{t}{2\pi L^2}\sqrt{\frac{E}{\rho}} \tag{B.5}$$

From Eqs. B.4 and B.5 we obtain the relation between the spring constant and the unloaded frequency:

$$k = 2\pi^3 L^3 d \sqrt{\frac{\rho^3}{E}}\nu_0^3 \tag{B.6}$$

It is important to note that in the last expression the dependence on cantilever thickness has disappeared. Manufacturers values of t have been shown to vary extremely from experimental measurements (Butt et al., 1993). This variable is difficult to determine and

requires the use of SEM or an equivalent technique. In contrast, Eq. B.6 can only be taken as a good approximation for the spring constant of V-shaped cantilevers since we start with the analytical expression for a rectangular cantilever beam. However, it may be possible to adapt the expression by invoking one of the various approximations for V-shaped cantilevers cited in the literature. One of them is the Parallel Beam Approximation which we review in the next section.

B.2.2 Parallel Beam Approximation (PBA)

The analytical result of the spring constant of a rectangular cantilever is well-known and has been shown in Eq. B.4. However, most of the cantilevers used in AFM are V-shaped, specially those utilized for biological studies. The PBA assumes that a V-shaped cantilever can be approximated by two rectangular beams joined in parallel. To our knowledge, at least three PBA formulations have appeared in the literature, namely Albrecht (Albrecht et al., 1990), Butt (Butt et al., 1993) and Sader (Sader et al., 1995) PBA, even if different approximations can be found. The work by Sader et al. reviews the first two developments and presents the third one as the most precise method [2].

As we mentioned there are at least three expressions for the PBA. This is due, in part, to the ambiguity in the selection of the width and length for the two rectangular arms of the V-shaped cantilever, since these are not parallel but skewed to one another. Using the width and length proposed by Sader (Fig. B.2) the formulas proposed by Albrecht, Butt and Sader can be written as:

$$k_{Albrecht} = \frac{Et^3 d}{2L^3}\left\{1 + \frac{b^2}{4L^2}\right\}^{-2} \tag{B.7}$$

$$k_{Butt} = \frac{Et^3 d}{2L^3} \tag{B.8}$$

$$k_{Sader} = \frac{Et^3 d}{2L^3}\cos\theta\left\{1 + \frac{4d^3}{b^3}(3\cos\theta - 2)\right\}^{-1} \tag{B.9}$$

Note that all three expressions converge to the same exact result for the PBA when supposing that the rectangular arms are parallel and infinitely narrow, *i.e.*, when $b/L \to 0$ and $d/b \to 0$.

Sader (Sader et al., 1995), using practical values of $d/b \sim 0.2$, computes errors for all the approximations in relation to a *rigorous finite element analysis* of the problem, obtaining

[2] All expressions and figures appeared in this section have been extracted from Sader et al. 1995

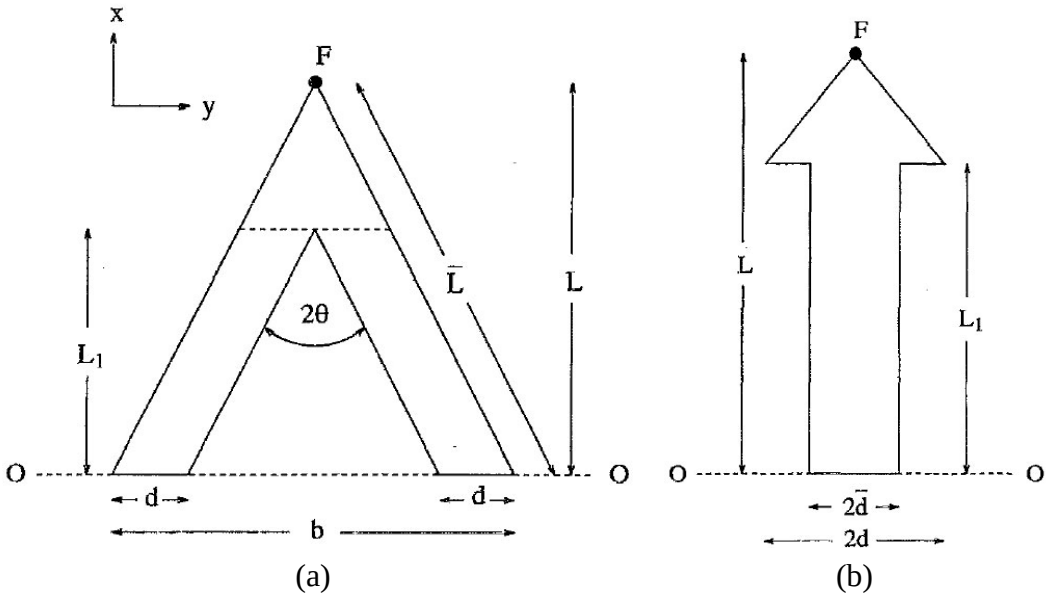

Figure B.2: (a) Cross-section of a V-shaped AFM cantilever showing the chosen dimensions (b)Cross-section of the equivalent cantilever for the V-shaped AFM showing chosen dimensions.

25, 16 and 2 % in error for Albrecht, Butt and Sader methods, respectively. The three reviewed expressions and its relative errors are summarized in table B.1.

Formulation	Spring constant formula	% error
Albrecht PBA (Eq. B.7)	$k = \frac{Et^3d}{2l^3}\{1 + \frac{b^2}{4L^2}\}^{-2}$	25 %
Butt PBA (Eq. B.8)	$k = \frac{Et^3d}{2l^3}$	16 %
Sader PBA (Eq. B.9)	$k = \frac{Et^3d}{2l^3}\cos\theta\{1 + \frac{4d^3}{b^3}(3\cos\theta - 2)\}^{-1}$	2 %

Table B.1: Summary of formulas presented for the spring constant of V-shaped AFM cantilevers.

Although Sader formulation seems to be very accurate, it presents a serious problem for its routine use. To determine the spring constant, it is necessary to know (measure) the cantilever width d, length L, semi-open angle θ and, in addition, its thickness t. The measurement of the latter is only possible by using SEM or similar technique which may do the calibration process extremely slow and complex. Moreover, neither manufacturers nor available SEM resolutions (Fig. B.3) seem to be accurate enough since the spring constant has a cubic dependence on thickness which may introduce large errors in the value of k.

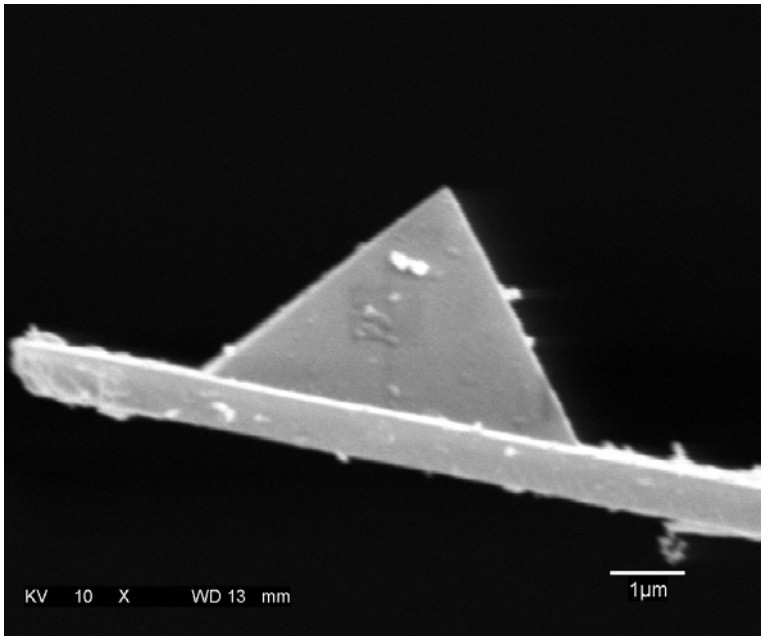

Figure B.3: Scanning Electron Microscopy image of the end of a cantilever with pyramidal tip. Note the difficulty in the determination of the cantilever thickness. Bar = 1 μm

B.2.3 Precalibrated beam method

The following method is based on static loading. The method consist in loading the cantilever with a known force. The known force is applied by a beam, a cantilever (Gibson et al., 1996) or a glass fiber (Li et al., 1993) with known spring constant, k_{beam} (see Fig. B.4). As can be deduced from the figure, when the two cantilevers are in contact we can equate the forces: $F_{beam} = F_{probe}$, where F_{probe} is the applied force of the cantilever we want to calibrate. Using Hooke's law, we obtain the following expression

$$k_{beam}(z - d) = k_{probe}d \tag{B.10}$$

where z is the height travel of the cantilever fixed end (*i.e.* the piezo travel) and d is the detected deflection of the cantilever. Solving Eq. B.10 for k_{probe} we obtain the expression for the determination of the spring constant of the cantilever

$$k_{probe} = k_{beam}\left(\frac{z}{d} - 1\right) \tag{B.11}$$

The above method has shown to introduce ~20% error. Mainly, it comes from the uncertainty in the determination of the spring constant of the reference cantilever, that was previously calibrated using one of the methods referred in the literature. Another

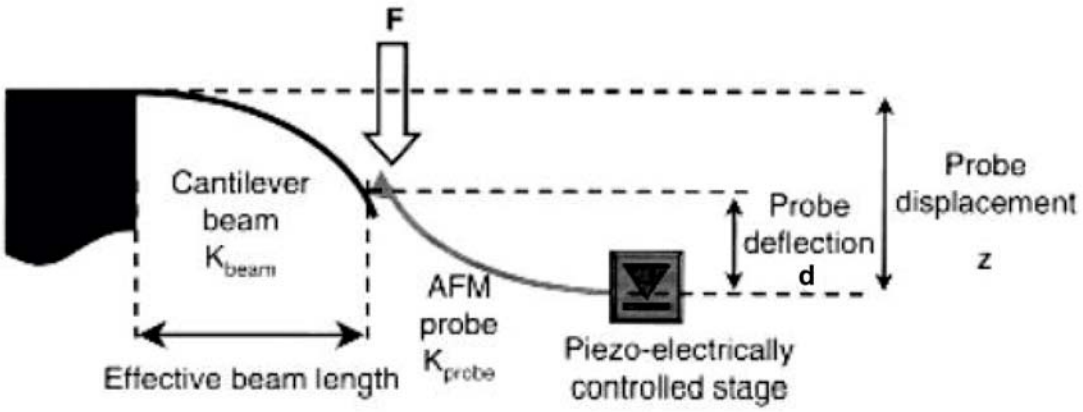

Figure B.4: Set up configuration for the precalibrated beam method.

source of error is the uncertainty of the point of loading. As shown by Sader *et al.*(Sader, 1995) practical loading is applied away from the end and central point of the cantilever. This can lead to large discrepancies in the obtained spring constant. In fact, using this method we obtained discrepancies as large as 200%.

B.2.4 Thermal fluctuations

The thermal fluctuations method (Hutter and Bechhoefer, 1993) is probably the most applied and cited method we can find in literature.

In the low deflection regime, the AFM cantilever can be approximated to a simple harmonic oscillator. Invoking the equipartition theorem: the average value of each quadratic term of the Hamiltonian of the isolated system is given by $k_B T/2$:

$$\frac{1}{2}k_B T = \frac{1}{2} < z^2 > \tag{B.12}$$

where k_B is the Boltzmann constant, T the absolute temperature and $< z^2 >$ the mean squared displacement of any mode of oscillation of the cantilever. By measuring the rms fluctuations of the freely moving cantilever we compute the spring constant solving Eq. B.12 for k:

$$k = \frac{k_B T}{< z^2 >} \tag{B.13}$$

(Eq. 3 in (Hutter and Bechhoefer, 1993)). With the measured thermal vibrations, we obtain the power spectrum. The area under the first resonant peak in the obtained spectrum gives a measure of $< z^2 >$. In order to isolate the contribution of possible sources of noise, we fit the first resonant peak to a Lorentzian with a constant background, the theoretical

curve shape obtained for a simple harmonic oscillator:

$$A(\omega) = N + \frac{A_{dc}^2 \omega_0^4}{(\omega_0^2 - \omega^2)^2 + \frac{\omega_0^2 \omega^2}{Q^2}} \tag{B.14}$$

where N is a constant offset (white noise), A_{dc} the amplitude of the peak, ω_0 the resonant frequency and Q the quality factor. The area below this curve, removing the background N, is the mean squared displacement of the cantilever due only to thermal fluctuations, P. The authors used this value to compute the spring constant using Eq. B.13. However, when the optical lever technique is applied to measure the deflection of the cantilever, a correction has to be done. We explain it briefly in the following subsection.

Correction of the power spectrum

The correction was first suggested by Butt and Jaschke (Butt and Jaschke, 1995). As authors introduce, in most of the available atomic force microscopes, the cantilever deflection is measured with the optical lever technique. Briefly, a laser beam focuses on the cantilever and changes in the reflection angle are measured in a position sensitive photodiode. Hence, what we really measure is not the deflection $z(L)$ of the cantilever itself, but its inclination $dz(L)/dx$. For this reason, when using the optical lever technique, we are interested in the thermal noise of $dz(L)/dx$ rather than that of $z(L)$. The authors find the expressions for the thermal fluctuations in the deflection $< z_i^2 >$ and in the inclination $< z_i^{*2} >$, and show that they are related to each other. They arrive to the following expressions of the thermal noise for each vibration mode, i:

$$< z_i^2 >= \frac{12 k_B T}{k \alpha_i^4} \tag{B.15}$$

$$< z_i^{*2} >= \frac{16 k_B T}{3 k \alpha_i^2} \left(\frac{\sin \alpha_i \sinh \alpha_i}{\sin \alpha_i + \sinh \alpha_i} \right)^2 \tag{B.16}$$

where α_i is a certain value that depends on the cantilever configuration (with its end free or with it fixed[3]) and on the vibration mode.

We can now isolate k form Eq. B.16 obtaining the final expression used for the calibration:

[3]When the cantilever is fixed at its two ends (*e.g.* when the free end is pressing on a hard surface) the detection system continues to measure oscillations. And different vibrations peaks can be observed in the power spectrum. This fact confirms that what we measure is the inclination of the lever and not its actual deflection.

$$k = c_i \frac{k_B T}{< z^2 >} \tag{B.17}$$

where $c_i = \frac{16}{3\alpha_i^2}\left(\frac{\sin\alpha_i \sinh\alpha_i}{\sin\alpha_i + \sinh\alpha_i}\right)^2$ is the correction factor. Note that Eq. B.17 is exactly the same as the one obtained by Hutter and Bechhoefer, (Eq. B.13), except for the correction factor.

In the case of a lever with a free end, *i.e.* the configuration used for the calibration, α_i takes different values for each vibration mode leading to the correction factors showed in table B.2.

Table B.2: Butt and Jaschke correction factors for the first six vibration modes, i

i	α_i	Correction factor, c_i
1	1.8751	0.8174
2	4.6941	0.2511
3	7.8548	0.0863
4	10.9955	0.0441
5	14.1372	0.0267
6	17.2788	0.0179

B.3 Conclusions

The thermal fluctuations method is probably the most appropriate method to use in the measuring routine for three main reasons. First, the acquisition of thermal fluctuations at high enough sampling rate is available in our laboratory for the three AFM systems used. Second, the method does not require additional measurement and data processing, apart from the computation of the power spectrum, such as SEM or optical image acquisition and processing to determine the actual dimensions. It is possible to use it in both air and liquid conditions. The method can easily be used before measurements to have the actual spring constant and apply controlled forces. And third, it is, at the moment, the most extended method used in routine laboratory protocols.

In conclusion, we opted to use the thermal fluctuations method for our routine use in AFM measurements using the following protocol.

Therefore, to calibrate the spring constant of the cantilever, thermal fluctuations of the deflection of the cantilever were acquired in air or liquid at room temperature at a scan rate of at least 50 kHz with an antialiasing filter at 22 kHz. The data willl be analysed in the frequency domain, computing the power spectrum. Contributions other than the first

oscillation mode can be rejected by isolating the first resonant peak and subtracting the offset value of the spectrum, due to white noise. Another correction to introduce is the one suggested by Butt and Jaschke (Butt and Jaschke, 1995). The obtained peak will be fitted to a Lorentzian curve. The mean square of the fluctuations is equal to the integral of the power spectrum, estimated by computing the area under the curve of the Lorentzian fit, P. The applied formula is given by $k = ck_BT/P$ (Eq.4 in Hutter and Bechhoefer 1993) with correction factor introduced). The accuracy of this method had been estimated to be within 10-20% (Burnham et al., 2003; Walters et al., 1996).

Bibliography

T. R. Albrecht, S. Akamine, T. E. Carver, and C. F. Quate. Microfabrication of cantilever styli for the atomic force microscope. *J.Vac.Sci.Technol.A*, 8(4):3386–3396, 1990.

G. Binnig, C. F. Quate, and Ch Gerber. Atomic force microscope. *Phys.Rev.Lett.*, 56(9): 930–933, 1986.

N. A. Burnham, X. Chen, C. S. Hodges, G. A. Matei, E. J. Thoreson, C. J. Roberts, M. C. Davis, and S. J. B. Tendler. Comparison of calibration methods for atomic-force microscopy cantilevers. *Nanotechnology*, 14(1):1–6, 2003.

H. J. Butt and M. Jaschke. Calculation of thermal noise in atomic force microscopy. *Nanotechnology*, 6:1–7, 1995.

H. J. Butt, P. Siedle, K. Seifert, K. Fendler, T. Seeger, E. Bamberg, A. L. Weisenhorn, K. Goldie, and A. Engel. Scan speed limit in atomic force microscopy. *J.Microsc.-Oxf.*, Vol 169(Iss JAN):75–84, 1993.

J. P. Cleveland, S. Manne, D. Bocek, and P. K. Hansma. A nondestructive method for determining the spring constant of cantilevers for scanning force microscopy. *Rev.Sci.Instr.*, 64(2):403–405, 1993.

C. T. Gibson, G. S. Watson, and S. Myhra. Determination of the spring constants of probes for force microscopy/spectroscopy. *Nanotechnology*, 7:259–262, 1996.

J. L. Hutter and J. Bechhoefer. Calibration of atomic-force microscope tips. *Rev.Sci.Instr.*, 64(7):1868–1873, 1993.

Y. Q. Li, N. J. Tao, J. Pan, A. A. Garcia, and S. M. Lindsay. Direct measurement of interaction forces between colloidal particles using the scanning force microscope. *Langmuir*, 9:637–641, 1993.

J. E. Sader. Parallel beam approximation for v-shaped atomic force microscope cantilevers. *Rev.Sci.Instr.*, 66(9):4583–4587, 1995.

J. E. Sader, I. Larson, P. Mulvaney, and L. White. Method for the calibration of atomic force microscope cantilevers. *Rev.Sci.Instr.*, 66(7):3789–3798, 1995.

D. A. Walters, J. P. Cleveland, N. H. Thomson, P. K. Hansma, M. A. Wendman, G. Gurley, and V. Elings. Short cantilevers for atomic-force microscopy. *Rev.Sci.Instr.*, Vol 67(Iss 10):3583–3590, 1996.

Appendix C

Publications and congress contributions

Publications

1. Puig, F, **F Rico**, I Almendros, JM Montserrat, D Navajas, and R Farré. Vibration Enhances Interleukin-8 Release In A Cell Model Of Snoring-Induced Airway Inflammation. *Sleep* **28** (10) 1312-1316 2005

2. **Rico, F**, P Roca-Cusachs, N Gavara, R Farré, M Rotger, and D Navajas. Probing Mechanical Properties of Living Cells by Atomic Force Microscopy with Blunted Pyramidal Cantilever Tips. *Phys Rev E* **72** (2) 021914 2005

3. Roca-Cusachs, P, **F Rico**, E Martínez, J Toset, R Farré, D Navajas. Stability of Microfabricated High Aspect Ratio Structures in Poly(dimethylsiloxane). *Langmuir* **21** (12) 5542-5548 2005

4. **Rico, F**, J Alcaraz, JJ Fredberg, and D Navajas. Nanomechanics of Lung Epithelial Cells. *Int J Nanotechnology* **2** (1/2) 180–194 2005

5. Trepat, X, M Grabulosa, L Buscemi, **F Rico**, R Farré, and D Navajas. Thrombin and histamine induce stiffening of alveolar epithelial cells. *Journal of Applied Physiology* **98** 1567-1574 2005

6. **Rico, F**, X Fernández-Busquets and G Gomila. Applications of Atomic Force Microscopy in Biology in *Phantoms Report on Scanning Probe Microscopy: Basic Concepts and Applications*. *Phantoms Report* **2** 81 2003

7. Trepat, X, M Grabulosa, L Buscemi, **F Rico**, B Fabry, JJ Fredberg and R Farre. Oscillatory Magnetic Tweezers Based On Ferromagnetic Beads and Simple Coaxial Coils. *Review of Scientific Instruments* **74** (9) 4012-20 2003

8. Grabulosa, M, L Buscemi, J Alcaraz, X Trepat, **F Rico** and D Navajas. Nanotecnologies en mecànica molecular i cel·lular. Biofísica molecular. *Treballs de la Societat Catalana de Biologia* **53** 91-99 2002

Meeting abstracts

1. Farré, R, F Puig, **F Rico**, M Rotger, JM Montserrat, and D Navajas. Inflammation induced in bronchial epithelial cells by vibration at snoring frequencies: Role of MAP kinase pathways in the production of IL-8. (Abstract) *International Conference American Thoracic Society*, San Diego, USA, May, 2005

2. **Rico, F**, P Roca-Cusachs, and D Navajas. Nanofabrication of cylindrical cantilever tips for probing mechanical properties of biopolymers by atomic force microscopy *2nd NanoSpain Workshop*, Barcelona, March 14-17, 2005

3. **Rico, F**, N Gavara, R Sunyer, M Rotger, and D Navajas. 3D NanoProbe for Measuring Mechanical Properties of Living Cells. (Oral contribution) *IV Jornades de Recerca en Enginyeria Biomèdica*, Barcelona, Spain, June 8-10, 2004

4. **Rico, F**, L Buscemi, N Gavara, M Rotger, R Farré, and D Navajas, Contact Model for Probing Cell Mechanics by Atomic Force Microscopy with Pyramidal Tips. (Abstract) *1st NanoSpain Workshop*, San Sebastián, March 10-12, 2004

5. **Rico, F**, L Buscemi, X Trepat, M Grabulosa, M Rotger, R Farré, and D Navajas. Measurement of the Elastic Modulus of Soft Samples with Atomic Force Microscopy Cantilevers. (Abstract) *4th European Biophysics Congress*. Alacant, Spain, July 5-9, 2003

6. **Rico, F**. Probing mechanical properties of soft samples with Atomic Force Microscopy. (Oral contribution) *II Workshop of the European Network PHYNECS. Nonequilibrium Physics: from complex fluids to biological systems*, Sant Feliu de Guíxols, Spain, June 16-20, 2003

7. Buscemi, L, M Grabulosa, X Trepat, **F Rico**, D Navajas, R Farre. Effects of inflammatory mediators on the mechanical properties of human alveolar epithelial cells. (Abstract) *Experimental Biology 2003* (FASEB). San Diego, USA, April 11-15, 2003

8. Buscemi, L, M Grabulosa, **F Rico**, X Trepat, R Farre, D Navajas. Effect of thrombin on the mechanical properties of alveolar epithelial cells measured with atomic force

microscopy. (Abstract) B*iophysical Society 47th Annual Meeting*. San Antonio, USA, March 1-5, 2003

9. **Rico, F**. Mechanical properties of the cell measured by Atomic Force Microscopy. (Oral contribution) *I Workshop of the European Network PHYNECS EuroWork – Physbio1*, Peyresq, France, September 12-18, 2002